High-field electron spin resonance study of electronic inhomogeneities in correlated transition metal compounds

D ISSERTATION

zur Erlangung des akademischen Grades

Doctor rerum naturalium

(Dr. rer. nat.)

vorgelegt

der Fakultät für Mathematik und Naturwissenschaften

der Technischen Universität Dresden

von

Master-Physiker

Alexey Alfonsov

Gutachter: Prof. Dr. B. Büchner

Prof. Dr. R. Klingeler

Tag der Einreichung: 26.04.2011

Tag der Disputation: 18.08.2011

Contents

Introduction

Electronic correlations are originating from the Coulomb interactions between electrons. They play a major role in the definition of the electronic structure and, as following, in the physical properties of a wide range of materials. In the case of weak correlations the description of properties can be simplified to the level of non-interacting particles, as in normal uncorrelated metals. When strong correlations are involved then the materials are exhibiting intriguing and unexpected properties due to a large number of degrees of freedom in the electronic interactions. These interactions can be of a spin, charge, lattice, or orbital origin and moreover can be simultaneously active. There are many fascinating examples of properties that systems with strong correlations possess: Colossal magnetoresistance (CMR), where enormous changes in resistance are produced by small magnetic field variations [1]; High-temperature superconductivity (HTSC) with superconducting transition temperatures up to $135\,\mathrm{K}$ at ambient pressure [2, 3]; Low-dimensional spin systems where the growth of quantum fluctuations gives rise to new exciting phenomena absent in three-dimensional systems [4, 5]; etc. Understanding these materials is very challenging and important for the establishment of our view of solids. A great example of research which pushed far ahead the understanding of the physics and stimulated the development of experimental and theoretical methods is the investigation of the high-temperature superconducting cuprates [2, 3].

Experimental results obtained in recent years have revealed that many transition-metal-based materials, especially oxides, exhibit charge, structural and/or magnetic inhomogeneities at the nanoscale (and sometimes at mesoscopic length scales). The presence of such inhomogeneities immediately calls for local probe techniques. One of them is high-field electron spin resonance spectroscopy (ESR) which is able to access a wide range of electronic properties of the materials, such as magnetic ordering and interactions, local magnetic fields, local electric field distribution

(crystal field effect), spin dynamics, etc. Employing the ESR method, we address in this work the problem of inhomogeneities in strongly correlated electronic systems by studying two systems based on transition metal elements, with very different properties. The first system is an iron based high-temperature superconductor. The present work was focused on a member of the so called 1111-family, $(La,Gd)O_{1-x}F_xFeAs$ compound. As it is established, this material exhibits coexistence of a static short range magnetic order with superconductivity up to high doping levels. The other system is a cubic perovskite, cobaltite $LaCoO_3$ where hole doping induces a strong interaction between electrons on neighboring Co ions which leads to a collective high-spin state, called a spin-state polaron. These polarons are inhomogeneously distributed in the nonmagnetic matrix.

This thesis is organized in three chapters. The first chapter gives basic ideas of magnetism in solids, focusing on the localized picture. The aim of the second chapter is to introduce the method of ESR. The third chapter is dedicated to the study of 1111-type iron arsenide superconductors. In the first part X-band ($\nu \sim 9.5\,\mathrm{GHz}$) ESR measurements on 2% and 5% Gd-doped $LaO_{1-x}F_xFeAs$ are presented. In the second part a combined investigation of the properties of $GdO_{1-x}F_xFeAs$ samples by means of thermodynamic, transport and high-field electron spin resonance methods is presented. The last, fourth chapter presents the investigation of the unexpected magnetic properties of lightly hole-doped $LaCoO_3$ cobaltite by means of the electron spin resonance technique complemented by magnetization and nuclear magnetic resonance measurements.

Chapter 1

Theoretical background

1.1 Overview

In this chapter the basic theoretical background will be given in order to help understanding the phenomenon of electron spin resonance. The discussions will mostly address quantum mechanical (QM) properties of atom or ion. Where possible, the classical examples/analogies will be given to help getting into the physics of the subject. The information presented here is based on the text-books of C. Kittel [6], S. Blundell [7], J. Weil an J. Bolton [8], S. Altshuler and B. Kozyrev [9], A. Abragam and B. Bleaney [10], C. Poole [11], L. Landau and L. Lifshitz [12].

1.2 Angular momenta and magnetic moments of electron

Orbital and spin momenta

Due to the quantum nature, an electron possess "own" ("eigen" or "intrinsic") angular moment, called *spin*. In addition, due to the orbital motion, an electron has an orbital angular momentum. In quantum mechanics the allowed values of the magnitude of the angular momentum arising from its operator $\mathbf{J}$ [1] [12–14] are given by $J(J + 1)$ where J is the primary angular-momentum quantum number

---

[1] In the case of orbital angular momentum one should write $\mathbf{L}$, in the case of spin - $\mathbf{S}$
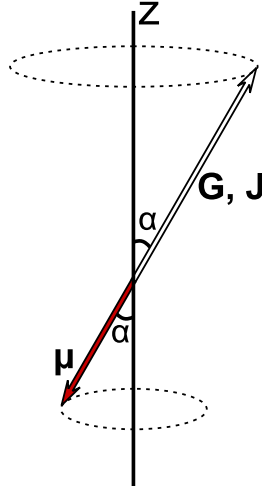
FIGURE 1.1: Angular and magnetic moments

$(J = 0, 1/2, 1, 3/2, ...)$. In the usual convention all angular momenta and their components are given in units of $\hbar$. The allowed values of the component of vector **J** along any selected direction are restricted to the quantum numbers M_J, which range in unit increments from $-J$ to $+J$, giving $2J+1$ possible components along an arbitrary direction.

Relation between angular momentum and magnetic moment

In both classical and quantum mechanics the angular momentum of an electron is proportional to a magnetic moment (Fig.1.1):

$$\boldsymbol{\mu} = \gamma \mathbf{G} \tag{1.1}$$

Here $\boldsymbol{\mu}$ is the magnetic moment, γ is the gyromagnetic ratio and **G** is either a classical angular momentum or a quantum one. In the quantum case the relation can be presented as:

$$\mathbf{G} = \hbar \mathbf{J} \tag{1.2}$$

As it follows from Eq.1.1 and Eq.1.2, values of the component of vector $\boldsymbol{\mu}$ along any selected direction are quantized as well as in the case of **J**. The gyromagnetic ratio is equal to:

$$\gamma = -g\frac{e}{2m_e c} \tag{1.3}$$

where e is electron charge, m_e is electron mass, c is the speed of light and g is a so called g-factor which depends on several properties of the system. For example, in the case of only orbital angular momentum, the g-factor with the accuracy of 10^{-4} is equal to $g_{\mathrm{L}} = 1$. In the case of only a spin angular momentum $g_{\mathrm{S}} = 2.0023$[1].

1.3 Electron Hamiltonian

In quantum mechanics the energy states of a system are given by the solution of the Schrödinger equation:

$$\boldsymbol{\mathcal{H}}\boldsymbol{\Psi} = E\boldsymbol{\Psi} \tag{1.4}$$

where $\boldsymbol{\mathcal{H}}$ is the Hamiltonian operator, E are eigenvalues of this operators (energy states of the system) and $\boldsymbol{\Psi}$ is a set of eigenfunctions of the system.

The Hamiltonian operator for one electron orbiting about the nucleus is written as:

$$\boldsymbol{\mathcal{H}_e} = \frac{\boldsymbol{p}^2}{2m_e} - \frac{Ze^2}{r} \tag{1.5}$$

Here the first term is the kinetic energy of the electron (m_e - electron mass, $\boldsymbol{p}$ - momentum operator) and the second one is the potential energy of the Coulomb attraction (Z - nuclear charge number, e - electron charge, r - distance between nucleus and electron).

In the case of an atom with N electrons ($N > 1$), beside the sum over all single electron Hamiltonians, the full Hamiltonian will contain also the Coulomb interaction between electrons:

$$\boldsymbol{\mathcal{H}} = \sum_{k=1}^{N}(\boldsymbol{\mathcal{H}_{e\,k}} + \frac{1}{2}\sum_{k\neq l}\frac{e^2}{|\boldsymbol{r}_k - \boldsymbol{r}_l|}) = \sum_{k=1}^{N}(\frac{\boldsymbol{p}_k^2}{2m_e} - \frac{Ze^2}{r_k} + \frac{1}{2}\sum_{k\neq l}\frac{e^2}{|\boldsymbol{r}_k - \boldsymbol{r}_l|}) \tag{1.6}$$

The inter-electron interaction makes the solution of the Schrödinger equation for this case rather complex, or even impossible. A common approach is the Hartree-Fock approximation [18–20] which is the assumption that each electron is situated in the central-symmetric electric field, created by other electrons[2]. In this case

---

[1] "For those readers with masochistic tendencies, we furnish some references [15–17] to the quantum electrodynamic theory of the electron magnetic moment, which has been spectacularly successful in matching the observed value of g_{S}, and continues to evolve with ever-increasing sophistication." - quotation from "Electron paramagnetic resonance elementary theory and practical applications" by John A. Weil and James R. Bolton [8].

[2] This field is usually called self-consistent field

the full Hamiltonian will be the sum of single electron Hamiltonians including the central-symmetric field term $V_k(k)$:

$$\boxed{\mathcal{H} \approx \mathcal{H}_0 = \sum_{k=1}^{N}(\frac{\boldsymbol{p}_k^2}{2m_e} - \frac{Ze^2}{r_k} + V_k(k))} \tag{1.7}$$

Since the electrostatic potential $-V_k(k)/e$ is central-symmetric, then the solution of the Schrödinger equation for this Hamiltonian can be obtained using the eigenfunction or spinor presented in polar coordinates as a product of a radial and angular parts[1]:

$$\psi_k = R_{nl}(r)Y_l^{m_l}(\theta, \phi)\chi(m_s), \; k = (n, l, m_l, m_s) \tag{1.8}$$

The radial part $R(r)$ is the function of only distance r between nucleus and the electron. The angular part, in turn, is the function of only two polar angles. This part depends on the orbital quantum number l and on the magnetic quantum number m_l which gives the z component of the angular momentum. To distinguish different m_s[2] states of the electron, this spinor ψ_k, beside radial and angular parts, consists of a spin part $\chi(m_s)$. The total eigenfunction for the many electron Hamiltonian $\mathcal{H}_0$ (Eq.1.7) can be obtained by the construction of the $N \times N$ Slater determinant $\Psi_N(\psi_k)$ of N single electron spinors ψ_k. The use of a determinant of spinors ensures the antisymmetry of many electron eigenfunction and thus satisfies the Pauli principle by the natural antisymmetry of determinants.

Spinors ψ_k, defining the electron states in atom, are characterized by 4 quantum numbers n, l, m_l, m_s. Here n is called as principal quantum number, l is the orbital quantum number and as it results from the solution (see [12–14]) it can not exceed the $n - 1$ value. m_l is a z-component of an electron orbital moment. In contrast to a single-electron atom, in the case of a many-electron atom the degeneracy in l is lifted because the potential is no longer $1/r$. Physically this means that states with lower angular momentum have a larger probability to be near the origin and hence sample more of the nuclear charge, while states of high angular momentum, which are suppressed at the origin, see the nuclear charge shielded by the electrons in the inner orbits. As a result, at each n the energy goes up with l. The "radius" of each state grows with n, with a slight dependence on l. States of a given n are thus said to form a shell (in a semiclassical sense, they may be viewed as moving

---

[1]Problem of the hydrogen atom in QM [12–14]
[2]m_s is a z-component of an electron spin

on a sphere of radius equal to the most probable value of r). States of a given l and n are said to form a subshell. So for a fixed pair of quantum numbers (n, l) the subshell is spanned by $2l + 1$ orbitals of identical energy, each of them holding at most two electrons with different spin direction m_s. This manifold of $2(2l + 1)$ electronic states defines a multiplet. The common way to describe a multiplet is to use a number for n, letter s,p,d,f... for l (see also Sec.1.4) and superscript for electron number. For example the outermost multiplet of Co^{3+} is $3d^6$.

1.4 Electronic configuration, Hund's rules

In Sec.1.3 the possible electronic energy levels were obtained for a multi-electron atom. It was shown, that to determine the ground state of the atom, or, in other words, the electronic configuration, one should minimize its energy while solving the Schrödinger equations. In the Hartree-Fock approximation case this effectively means that one should "fill" the free electronic states starting from the one with lowest energy. In the case of a free atom at a given pair of quantum numbers (n, l) there is a remanent $2(2l+1)$-fold degeneracy of the energy levels. The procedure of "filling" these degenerated levels is governed by empirical Hund's rules [21–23] and Pauli principle [24]. As they rule the occupation of the orbitals in terms of their quantum numbers, the magnetic moment of the ion is immediately determined. The three empirical Hund's rules are listed in order of decreasing importance, so that one first satisfies the first and then, having done this, attempts to satisfy the second, and so on for the third.

(1) Arrange the electronic wave function so as to maximize S. In this way the Coulomb energy is minimized because of the Pauli exclusion principle, which prevents electrons with parallel spins being in the same place, and this reduces Coulomb repulsion between electrons.

(2) The next step is, given the wave function determined by the first rule, to maximize L. This also minimizes the energy and can be understood by imagining that electrons in orbits rotating in the same direction can avoid each other more effectively and therefore reduce Coulomb repulsion.

(3) Finally the value of J (see Sec.1.5) is found using $J = |L - S|$ if the shell is less than half full and $J = |L + S|$ if it is more than half full. This third rule arises from an attempt to minimize the spin-orbit energy. One should note that the third

rule is only applicable in certain circumstances. In many systems, e.g. transition metal ions, the spin-orbit energies are not as significant as some other energy term such as the crystal field so that Hund's third rule is disobeyed. However, for rare earth ions Hund's third rule works very well.

Having found values for S, L and J, this ground state can be summarized using a term symbol of the form $^{2S+1}L_J$. Here L is written not as a number, but using a letter according to the sequence:

L	0	1	2	3	4	5	...
	S	P	D	F	G	H	...

The value $2S+1$ represents a spin multiplicity. One should note here that Hund's rules lead to a prediction of the ground state but tell nothing about the excited states or how close they are to the ground state.

1.5 Spin-orbit coupling

Nature of spin-orbit coupling

The spin-orbit interaction in an atom arises as follows. In the nucleus rest frame an electron is orbiting about an atom, but in an inertial frame comoving with the electron the nucleus appears to be orbiting about the electron. The orbiting nucleus constitutes a current which gives rise to a magnetic field at the origin equal to

$$\boldsymbol{B} = \frac{\boldsymbol{\mathcal{E}} \times \boldsymbol{v}}{c^2} \tag{1.9}$$

where

$$\boldsymbol{\mathcal{E}} = -\nabla V r = -\frac{\boldsymbol{r}}{r} \frac{dV(r)}{dr} \tag{1.10}$$

is the electric field at the electron due to the nucleus and $V(r)$ is the corresponding potential energy. Equation Eq.1.9 comes from the transformation of electric and magnetic fields in special relativity. This magnetic field interacts with the spin of the electron to give a term in the Hamiltonian

$$\mathcal{H}_{SO} = -\frac{1}{2}\boldsymbol{m} \cdot \boldsymbol{B} = \frac{e\hbar^2}{2m_e c^2 r} \frac{dV(r)}{dr} \boldsymbol{s} \cdot \boldsymbol{l} = \lambda \boldsymbol{s} \cdot \boldsymbol{l} \tag{1.11}$$

where the orbital angular momentum is given by $\hbar\boldsymbol{l} = m_e \boldsymbol{r} \times \boldsymbol{v}$ and the magnetic moment $\boldsymbol{m} = (e\hbar/m_e)\boldsymbol{s}$, and where the factor of $1/2$ in Eq.1.11 is the relativistic Thomas factor [25]. The parameter λ represents the strength of the spin-orbit coupling. This result can be obtained extremely elegantly with the relativistic correction automatically included using the Dirac equation[1]. This effect is known as the intrinsic spin-orbit interaction and is an interaction between the spin and the orbital part of an electron's wave function in an atom. For the Coulomb field in a hydrogen-like atom the potential energy $V(r)$ is known so

$$\frac{1}{r}\frac{dV(r)}{dr} = \frac{Ze}{4\pi\epsilon_0 r^3}. \tag{1.12}$$

As can be seen, depending on the charge of the nucleus, Ze, the spin-orbit coupling gains in strength for heavier elements. If more than one electron is considered, the structure of the coupling will basically be the same for each electron, but the amplitude will be influenced by screening effects which lower the coupling for electrons in outer shells.

Type of spin-orbit coupling

In the definition of the ground state of the free atom (ion) there is a competition between spin-orbit coupling and electrostatic interactions of electrons. In case of atoms with small and intermediate atomic number Z the spin-orbit interaction is a weak perturbation and the main energy terms are determined by the electrostatic interactions that control the values of L and S, i.e. by combining, separately, the orbital and spin angular momenta for the electrons:

$$L = \sum_{k=1}^{N} l_k \quad \text{and} \quad S = \sum_{k=1}^{N} s_k. \tag{1.13}$$

Only then, when the total orbital and spin angular momenta of the atom as a whole are known, we consider applying the spin-orbit interaction as a weak perturbation. This type of spin-orbit interaction is called as LS- or Russel-Saunders coupling [26].

---

[1]There are an infinite set of Lorentz transformations corresponding to the various instantaneous rest frames of the electron around its orbit. The Lorentz transformations do not commute when the direction of velocity changes and this is something our derivation has ignored. The net Lorentz transformation contains a rotation and it turns out that this Thomas precession yields a factor of precisely one-half.

The Hamiltonian in this case is:

$$\boxed{\mathcal{H}_{LS} = \lambda \boldsymbol{L} \cdot \boldsymbol{S}} \tag{1.14}$$

For atoms with high atomic number Z the spin-orbit interaction energy cannot be treated as a small perturbation. A better scheme is known as $j - j$ coupling: here the spin-orbit interaction is the dominant energy and we couple the spin and orbital angular momentum of each electron separately, and consequently the weaker electrostatic effect may then couple the total angular momentum from each electron.

Transition metals $(3d)$ and rare earth elements $(4f)$, which are studied in this thesis, both exhibit first type of coupling, namely LS or Russel-Saunders. Therefore we omit the discussion about $j - j$ coupling.

Effect of spin-orbit coupling

The presence of the LS-coupling yields that $\boldsymbol{L}$ and $\boldsymbol{S}$ are not separately conserved but the total angular momentum $\boldsymbol{J} = \boldsymbol{L} + \boldsymbol{S}$ is conserved. If the relativistic effects are considered as a perturbation (which usually can be done) then one can consider $\boldsymbol{L}^2 = L(L + 1)$ and $\boldsymbol{S}^2 = S(S + 1)$ as being conserved. Thus states with L and S are split into a number of levels with differing J; this is known as fine structure. J takes the values from $|L - S|$ to $|L + S|$. From the definition of J:

$$\boldsymbol{J}^2 = \boldsymbol{L}^2 + \boldsymbol{S}^2 + 2\boldsymbol{L} \cdot \boldsymbol{S}, \tag{1.15}$$

and since the spin-orbit interaction takes the form $\lambda \boldsymbol{L} \cdot \boldsymbol{S}$, where λ is a constant, the expected value of this energy is

$$< \lambda \boldsymbol{L} \cdot \boldsymbol{S} >= \frac{\lambda}{2}[J(J + 1) - L(L + 1) - S(S + 1)]. \tag{1.16}$$

The energy of the atom is mainly determined by the values of S and L via electrostatic considerations and so the energy eigenstates can be labelled with values of S and L. The precise value that J takes in the range $|L - S|$ to $|L + S|$ is immaterial in the absence of the spin-orbit interaction. Each level is a multiplet of $(2S + 1)(2L + 1)$ states. When adding the spin-orbit interaction as a perturbation, the multiplets split up into different fine structure levels labelled by J. Each of

these levels themselves has a degeneracy of $2J + 1$. The splitting of the different fine structure levels follows a relationship known as the Landé interval rule which will now be described. The energy separation between adjacent levels $E(J)$ and $E(J-1)$ of a given multiplet is given by:

$$
\begin{aligned}
E(J) - E(J-1) &= \frac{\lambda}{2}[J(J+1) - L(L+1) - S(S+1)] - \\
&\quad -\frac{\lambda}{2}[(J-1)J - L(L+1) - S(S+1)] \\
&= \lambda J.
\end{aligned} \tag{1.17}
$$

Thus the splitting is proportional to J (considering the separation of levels $J-1$ and J).

Magnetic moment associated with $\boldsymbol{J}$, Landé g-factor

As in the case of $\boldsymbol{S}$ and $\boldsymbol{L}$ angular momenta, there is a magnetic moment associated with $\boldsymbol{J} = \boldsymbol{L} + \boldsymbol{S}$ (see Sec.1.2):

$$
\boldsymbol{\mu} = g_J \mu_B \boldsymbol{J} \tag{1.18}
$$

Here g_J is called g-factor Landé and it is determined by:

$$
\begin{aligned}
g_J &= g_L \left(\frac{J(J+1) + L(L+1) - S(S+1)}{2J(J+1)} \right) \\
&+ g_S \left(\frac{J(J+1) - L(L+1) + S(S+1)}{2J(J+1)} \right)
\end{aligned} \tag{1.19}
$$

with g_L and g_S being g-factors for orbital and spin moments respectively. As can be seen, the presence of the orbital moment and spin-orbit coupling yield the g-factor value different from pure spin value of 2.

1.6 Zeeman effect, atom in magnetic field

Magnetic moment in magnetic field

When magnetic dipole is subjected to a magnetic field $\boldsymbol{H}$, it experiences a torque. In the classical picture the equation of motion is

$$\frac{d\boldsymbol{G}}{dt} = \boldsymbol{\mu} \times \boldsymbol{H} \tag{1.20}$$

which may be combined with Eq.1.1 to give

$$\frac{d\boldsymbol{G}}{dt} = \gamma \boldsymbol{G} \times \boldsymbol{H}. \tag{1.21}$$

If the magnetic field is assumed to lie along the z-axis of a system of Cartesian coordinates, the solution of this equation can be written in the form:

$$
\begin{aligned}
G_x &= G \sin\alpha \cos(\omega_L t + \epsilon) \\
G_y &= G \sin\alpha \cos(\omega_L t + \epsilon) \\
G_z &= G \cos\alpha
\end{aligned}
\tag{1.22}
$$

with analogous equations for $\boldsymbol{\mu}$. The motion the vectors $\boldsymbol{G}$, $\boldsymbol{\mu}$ consist of a uniform precession about $\boldsymbol{H}$ with angular velocity (Fig.1.1, $\boldsymbol{H}||z$)

$$\boldsymbol{\omega}_L = -\gamma \boldsymbol{H}. \tag{1.23}$$

where the negative sign means that the precession is in the direction of a left-handed screw advancing along $\boldsymbol{H}$ if γ is positive, and vice versa. The component of $\boldsymbol{G}$, $\boldsymbol{\mu}$ along $\boldsymbol{H}$ remains fixed in magnitude, so that the energy of dipole in the field $\boldsymbol{H}$

$$E = -\boldsymbol{\mu} \cdot \boldsymbol{H} \tag{1.24}$$

is a constant of the motion. Let us assume that only the electron spin produces the magnetic moment, which is true in the case of a free electron. Since in quantum mechanics magnetic moment $\boldsymbol{\mu}$ can have only quantized components along selected direction (see Sec.1.2), then there is a set of energy levels, associated with this components M_S

$$E = g\mu_B H M_S, \, M_S = -S... + S \tag{1.25}$$

where in case of electron $g \approx 2$ and $M_S = \pm 1/2$. Hence $E \approx \pm \mu_B H$. This splitting of the magnetic moment energy levels driven by the applied magnetic field is called Zeeman effect [27].

Atom in magnetic field

In addition to spin angular momentum, electrons in an atom also possess orbital angular momentum. If the position of the kth electron in the atom is $\boldsymbol{r}_k$, and it has momentum $\boldsymbol{p}_k$, then the total angular momentum is $\hbar \boldsymbol{L}$ and it is given by

$$\hbar \boldsymbol{L} = \sum_k \boldsymbol{r}_k \times \boldsymbol{p}_k \tag{1.26}$$

where the sum is taken over all electrons in an atom. Let us now consider an atom with a Hamiltonian $\mathcal{H}_0$ given by Eq.1.7.

We now add a magnetic field $\boldsymbol{H}$ given by

$$\boldsymbol{H} = \nabla \times \boldsymbol{A} \tag{1.27}$$

where $\boldsymbol{A}$ is the magnetic vector potential. We choose a gauge[1] such that

$$\boldsymbol{A}(\boldsymbol{r}) = \frac{\boldsymbol{H} \times \boldsymbol{r}}{2}. \tag{1.28}$$

Since the charge on the electron is $-e$, the kinetic energy is $[\boldsymbol{p}_k + e\boldsymbol{A}(\boldsymbol{r}_k)]^2/2m_e$ and hence the perturbed Hamiltonian must now be written

$$
\begin{aligned}
\mathcal{H} &= \sum_{k=1}^{N} \left(\frac{[\boldsymbol{p}_k + e\boldsymbol{A}(\boldsymbol{r}_k)]^2}{2m_e} - \frac{Ze^2}{r_k} + V_k(k) \right) + g\mu_B \boldsymbol{H} \cdot \boldsymbol{S} \\
&= \sum_{k=1}^{N} \left(\frac{\boldsymbol{p}_k^2}{2m_e} - \frac{Ze^2}{r_k} + V_k(k) \right) + \mu_B(\boldsymbol{L} + g\boldsymbol{S}) \cdot \boldsymbol{H} + \frac{e^2}{8m_e} \sum_{k=1}^{N} (\boldsymbol{H} \times \boldsymbol{r}_k)^2 \\
&= \mathcal{H}_0 + \mu_B(\boldsymbol{L} + g\boldsymbol{S}) \cdot \boldsymbol{H} + \frac{e^2}{8m_e} \sum_{k=1}^{N} (\boldsymbol{H} \times \boldsymbol{r}_k)^2
\end{aligned}
\tag{1.29}
$$

---

[1]Eq.1.27 relates $\boldsymbol{H}$ and $\boldsymbol{A}$. However, for a given magnetic field $\boldsymbol{H}$, the magnetic vector potential $\boldsymbol{A}$ is not uniquely determined; one can add to $\boldsymbol{A}$ the gradient of a scalar potential and still end up with the same $\boldsymbol{H}$. The choice of $\boldsymbol{A}$ that we make is known as a choice of gauge.

The dominant perturbation to the original Hamiltonian $\boldsymbol{\mathcal{H}}_0$ is usually the paramagnetic Zeeman term

$$\boxed{\boldsymbol{\mathcal{H}}_Z = \mu_B(\boldsymbol{L} + g\boldsymbol{S}) \cdot \boldsymbol{H}} \tag{1.30}$$

This is the effect of the atom's own magnetic moment. The third term, $\frac{e^2}{8m_e}\sum_{k=1}^{N}(\boldsymbol{H}\times \boldsymbol{r}_k)^2$, is due to the diamagnetic moment. This contribution is purely field-induced owing to its dependence on the square of the field. It is neglected in the following, since in moderate fields it is usually overcompensated by the permanent moment as long as it exists. Moreover, it is not responsible for an ESR signal.

1.7 Ligand environment

In the solid state we are concerned mostly with ions rather than with atoms. Many such ions have closed electron shells which have no resultant angular momentum and hence no permanent electronic magnetic dipole moment. Partly filled shells, with permanent dipole moments due to the orbital motion of the electrons, or to their intrinsic spin, or to both, occur in the 'transition groups' such as $3d$, $4d$, $5d$, $4f$ and $5f$ elements. Here we will restrict ourself with $3d$ and $4f$ elements only.

The ion in the solid is first of all influenced by the crystal field which is an electric field derived from neighbouring atoms in the crystal. In crystal field theory the neighbouring orbitals are modelled as negative point charges, this approach works rather well for $4f$ orbitals of rare earth element, but not good for $3d$ orbitals of transition metals. An improvement on this approximation is ligand field theory which is essentially an extension of molecular orbital theory that focusses on the role of the d orbitals on the central ion and their overlap with orbitals on surrounding ions (ligands). This difference is coming from different sensitivity of $3d$ and $4f$ ions to the crystal field. In the case of $3d$ element d shell is outermost which makes the effect of the crystal field to be very strong, much stronger than the spin-orbit coupling. In contrast, f shell is well shielded by the higher lying s and p shells which strongly reduces the influence of the crystal field and helps spin-orbit coupling to win in energy. Additionally, the size and nature of crystal field effects depend crucially on the symmetry of the local environment.

1.8   Transition metal elements in crystal field, 3d shell

Since the influence of the crystal field in the case of $3d$ elements is stronger than spin-orbit coupling, then the Hamiltonian will take a form

$$\mathcal{H} = \mathcal{H}_0 + \mathcal{H}_{CF} + \mathcal{H}_{LS} + \mathcal{H}_Z \qquad (1.31)$$

where $\mathcal{H}_0 >> \mathcal{H}_{CF} > \mathcal{H}_{LS} \geq \mathcal{H}_Z$. The initial Hamiltonian $\mathcal{H}_0$ is that of Hartree-Fock (see Eq.1.7), $\mathcal{H}_{CF}$ is a crystal field term, spin-orbit term $\mathcal{H}_{LS}$ is determined by Eq.1.14 and Zeeman term is defined in Eq.1.29. In the case of the initial Hamiltonian $\mathcal{H}_0$ the total L and S are conserved, so they can be used to describe states. To find the ground state we can use the perturbation method, starting with $\mathcal{H}_0$ and including CF, LS and Zeeman Hamiltonians step by step.

Splitting of orbital sates

The first one is $\mathcal{H}_{CF}$ since it has higher energy then the others. The electrostatic nature of the crystal field makes it acting on the orbital angular momentum, but does not affect spin. In the first approximation we do not consider LS-coupling (L and S are decoupled), so the crystal field splits only L states, or in other words it lifts the degeneracy of $3d$ orbitals. This splitting strongly depends on the symmetry of the crystal field. In many cases the transition metal has a cubic ligand surrounding, so it is important to consider the splitting in the crystal field of a cubic symmetry. Fig.1.2 depicts the angular part of the $3d$ orbital wavefunctions in the cubic symmetry. In the absence of the crystal field all these orbitals have the same energy, but in the octahedral ligand surrounding (red balls in Fig.1.2) this degeneracy is lifted. The orbitals $x^2 - y^2$ and $3z^2 - r^2$ are pointing towards ligands whereas xy, xz and yz orbitals are pointing in between. Since ligands are usually negatively charged electron "sitting" on xy, xz or yz orbital better avoids ligands than "sitting" on $x^2 - y^2$ or $3z^2 - r^2$ which yields that the energy of $x^2 - y^2$ and $3z^2 - r^2$ orbitals is higher then that of xy, xz and yz orbitals. So five degenerated orbital energy levels split into two groups: e_g, comprising $x^2 - y^2$ and $3z^2 - r^2$, and t_{2g}, comprising xy, xz and yz. Same splitting occurs also in the case of cubic
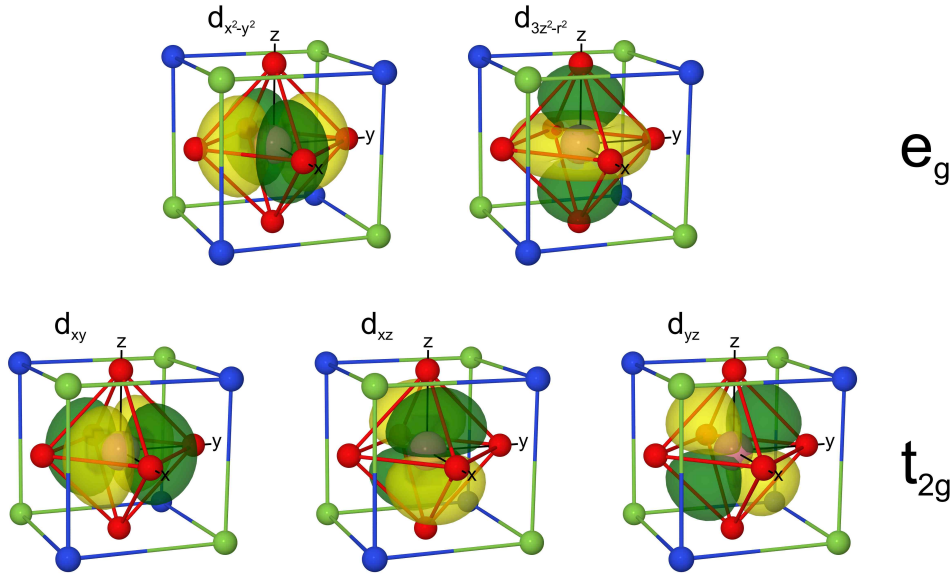
FIGURE 1.2: $3d$ orbitals in crystal field of a cubic symmetry

(blue and green balls in Fig.1.2) or tetrahedral (blue balls in Fig.1.2) surrounding but the e_g group has lower energy than t_{2g}.

Quenching of the orbital moment

The consequence of the splitting of the orbital states is the partial or total quench-ing of the orbital magnetic moment. The phenomenon of the quenching one can understand in the following. In an electric field directed towards a fixed nucleus, the plane of a classical orbit is fixed in space, so that all the orbital angular mo-mentum components L_x, L_y, L_z are constant. In quantum theory one angular momentum component, usually taken as L_z, and the square of the total orbital angular momentum L^2 are constant in a central field. In a noncentral field the plane of the orbit will move about; the angular momentum components are no longer constant and may average to zero. In a crystal L_z will no longer be a constant of the motion, although to a good approximation L^2 may continue to be constant. When L_z averages to zero, the orbital angular momentum is said to be quenched. The magnetic moment of a state is given by the average value of the magnetic moment operator $\mu_B(\boldsymbol{L} + 2\boldsymbol{S})$. In a magnetic field along the z direction the orbital contribution to the magnetic moment is proportional to the quantum
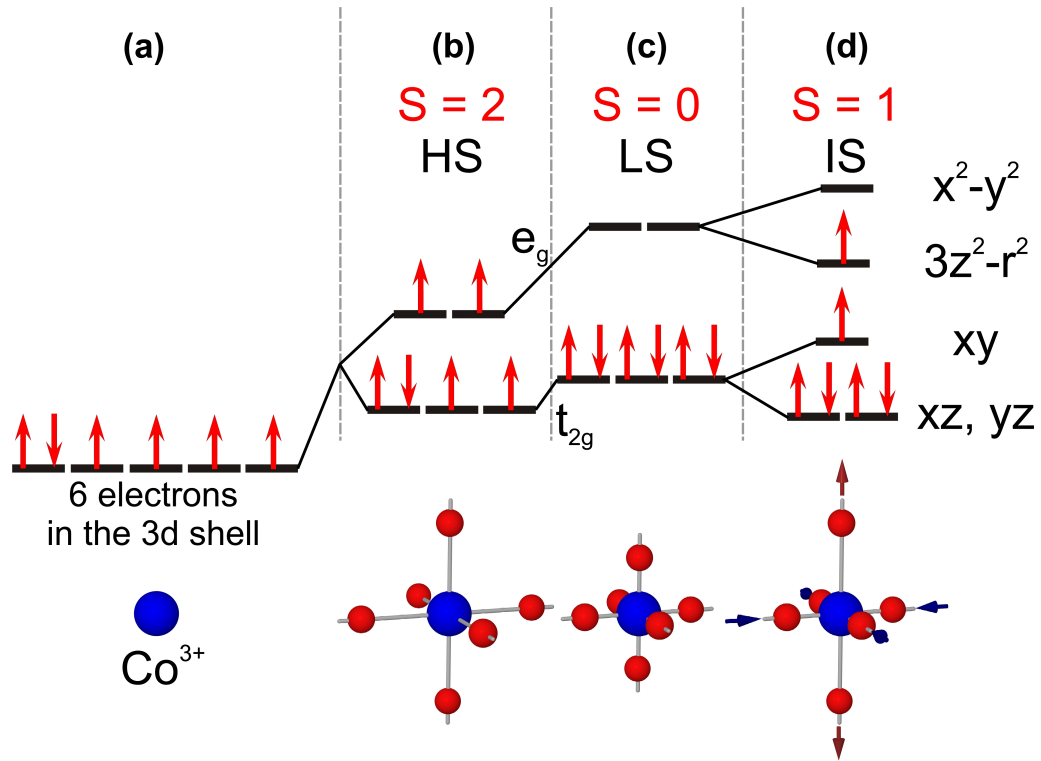
FIGURE 1.3: Splitting of $3d$ orbital states and stabilization of different spin states due to the crystal field strength and symmetry, shown on an example of Co^{3+} ion; **(a)** free ion; **(b)** weak crystal field, high spin state with $S = 2$; **(c)** strong crystal field, low spin state with $S = 0$; **(d)** tetragonal distortion, intermediate spin state with $S = 1$. See text for details.

expectation value of L_z. So if the mechanical moment L_z is quenched, then the orbital magnetic moment is quenched as well.

When the spin-orbit interaction energy is introduced, the spin may drag some orbital moment along with it. If the sign of the interaction favors parallel orientation of the spin and orbital magnetic moments, the total magnetic moment will be larger than for the spin alone, and the g value will be larger than 2. The experimental results are in agreement with the known variation of sign of the spin-orbit interaction: $g > 2$ when the $3d$ shell is more than half full, $g = 2$ when the shell is half-full, and $g < 2$ when the shell is less than half-full.

Determination of the ground state

After considering the splitting of the orbital states one can fill up these orbitals according to the Hund's rules and taking into account the quenching of the orbital

moment. Since we will need it later let us take an example of a Co^{3+} ion (Fig.1.3). In the case of a free ion there are 6 electrons on a $3d$ shell so the spin S is equal to 2 and orbital moment $L = 2$ (Fig.1.3,a). The SO-coupling leads to the magnetic ground state with $J = 4$.

In the non-distorted octahedral crystal field there are two possible configurations. When the energy of the crystal field is smaller than the Hund's energy (electric repulsion of electrons), then all electrons occupy both e_g and t_{2g} levels which gives the spin $S = 2$ (Fig.1.3,b). This spin state is called high spin state (HS). In this case crystal field splitting leads to the partial quenching of the orbital moment. To calculate the latter one can attribute the fictive orbital moment to the t_{2g} level which will be $\tilde{l} = -1$. Application of the Hund's rules only to the t_{2g} level yields the total orbital moment $L = 1$. After considering the crystal field splitting the SO-coupling can be taken into account since it is next biggest in energy perturbation (see Eq.1.31). The SO-coupling in this case yields the total moment of the ion $J = 1$.

Second configuration is represented on Fig.1.3,c. Here the energy of the crystal field is bigger than the Hund's energy (electric repulsion of electrons), so all electrons occupy only t_{2g} levels which gives the spin $S = 0$ and totally quenched orbital moment $L = 0$. This state is called low spin state (LS).

If the crystal field has symmetry lower then octahedral, then it leads to further splitting of the orbital states. For example the distortion of octahedra like uniaxial elongation (tetragonal distortion), as shown Fig.1.3,d leads to the splitting of t_{2g} level into orbital doublet and singlet and splitting of e_g level into two orbital singlets. Electric repulsion energy sets 4 electrons on the degenerated xz and yz orbitals, one on xy and one on $3z^2 - r^2$. This configuration gives a total spin $S = 1$ and the fully quenched orbital moment $L = 0$. The spin state in this case is called an intermediate spin state (IS).

1.9 Rare earth elements in crystal field, 4f shell

As was shown before, in the case of the rare earth elements in the crystal field the situation is different from transition metals. Here SO-coupling wins in energy
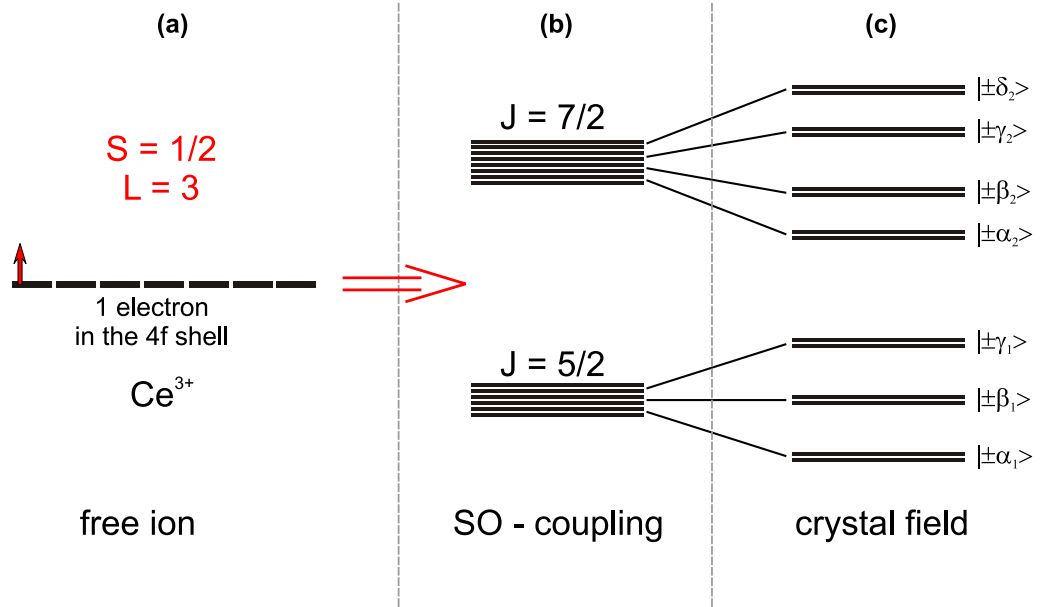
FIGURE 1.4: Energy levels of rare earth element Ce^{3+} due to the spin-orbit coupling and the crystal field; **(a)** free ion; **(b)** splitting of the states due to the spin-orbit coupling; **(c)** further splitting due to the crystal field. See text for details.

against the crystal field, so the Hamiltonian takes form of:

$$\mathcal{H} = \mathcal{H}_0 + \mathcal{H}_{LS} + \mathcal{H}_{CF} + \mathcal{H}_Z \tag{1.32}$$

where $\mathcal{H}_0 >> \mathcal{H}_{LS} > \mathcal{H}_{CF} > \mathcal{H}_Z$. The initial Hamiltonian $\mathcal{H}_0$ is that of Hartree-Fock (see Eq.1.7), spin-orbit term $\mathcal{H}_{LS}$ is determined by Eq.1.14 and the Zeeman term is defined in Eq.1.29. Since the SO-coupling energy is dominating the CF and Zeeman energy, then the good quantum number to describe states is $J = |L + S|$ or $J = |L - S|$ (see Hund's rules, Sec.1.4). As shown on Fig.1.4 in the case of Ce^{3+} ion, which has a half integer spin, firstly the SO-coupling splits states with different J, an only after that the crystal field splits states for a given J in a set of doublets. Each doublet has an effective spin $1/2$ and an effective g-factor depending on the crystal field.

1.10   Half-filled shell elements in crystal field, $3d^5$ and $4f^7$

Another case of the interaction of the crystal field with the ion is the case of ions with the half-filled shell, such as Cr^+, Mn^{2+}, Fe^{3+} ($3d$) and Gd^{3+}, Eu^{2+}, Tb^{4+}, Cm^{3+} ($4f$). Here, in the first approximation, ions do not have an orbital moment which should lead to the absence of the interaction with the crystal field. In fact such ions could have a very small splitting of the energy levels due to the crystal field. It can be explained by the fact that the presence of the crystal field leads to the slight deformation of orbitals, so there is an uncompensated small orbital moment which then couples to the spin [28].

1.11   Effective spin Hamiltonian

Whichever theoretical approach is adopted the result is a splitting of levels, leaving groups of rather small degeneracy. The degeneracy within each group (and, to some extent, the relative splittings between different groups) depends on the symmetry within the complex, and can thus be predicted by group theory. An important over-riding theorem concerning the residual degeneracy is due to Kramers [9, 10, 29]; in a system containing an odd number of electrons, at least twofold degeneracy must remain in the absence of a magnetic field.

At temperatures below room temperature only lower lying states of an ion are populated. To represent the behavior of such a group of levels when a magnetic field is applied to the system one can neglect higher lying states and use the concept of an 'effective spin' S, which is a fictitious angular momentum such that the degeneracy of the group of levels involved is set equal to (2S+1). For example, an isolated Kramers doublet with just two levels is assigned an effective spin S =1/2. This concept of an 'effective spin' is useful because it is possible to set up an 'effective spin Hamiltonian' that gives a correct description of the behavior of the group of levels in terms as concise as those for a free atom or ion. In some cases a theoretical justification of the effective spin Hamiltonian can be given; if the local symmetry of the complex is known, the effective spin Hamiltonian is expected to reflect this symmetry, thus imposing restrictions on its form. The good approach to write down such a Hamiltonian basing on the symmetry is to

use Stevens operators O_n^m [9, 30, 31]. In this case the crystal field part of the effective Hamiltonian for the tetragonal symmetry will be [9]:

$$\boxed{\boldsymbol{\mathcal{H}_{CF}} = B_2^0 O_2^0 + B_4^0 O_4^0 + B_6^0 O_6^0 + B_4^2 O_4^2 + B_6^4 O_6^4}$$ (1.33)

Stevens operators O_n^m are the functions of S_z, S_+, S_- and their higher orders, they can be found in several text-books [9, 30, 31]. Coefficients B_n^m depend on the crystal field strength and symmetry and are usually chosen empirically in order to better fit the experimental data obtained from magnetization, ESR, INS, etc. In the simplest case of uniaxial symmetry one can neglect the high order terms in Hamiltonian in Eq.1.33 and keep only the first term. Defining $D = 3B_2^0$ and knowing that $O_2^0 = 3S_z^2 - S(S+1)$ one can write:

$$\boldsymbol{\mathcal{H}_{CF}^{uniaxial}} = D(S_z^2 - \frac{S(S+1)}{3})$$ (1.34)

It is important to note that S is not necessarily the true angular momentum of the system, in which case the quantity g does not give the true magnetogyric ratio. For this reason g is better called the "spectroscopic splitting factor".

1.12   Interactions

Here we consider the different types of magnetic interaction which can be important in allowing the magnetic moments in a solid to communicate with each other and potentially to produce long range order.

Magnetic dipolar interaction

The first interaction which might be expected to play a role is the magnetic dipolar interaction. Two magnetic dipoles $\boldsymbol{\mu_1}$ and $\boldsymbol{\mu_2}$ separated by $\boldsymbol{r}$ have an energy equal to

$$E = \frac{\mu_0}{4\pi r^3}[\boldsymbol{\mu_1} \cdot \boldsymbol{\mu_2} - \frac{3}{r^2}(\boldsymbol{\mu_1} \cdot \boldsymbol{r})(\boldsymbol{\mu_2} \cdot \boldsymbol{r})]$$ (1.35)

which therefore depends on their separation and their degree of mutual alignment. We can easily estimate the order of magnitude of this effect for two moments each of $\mu = 1\,\mu_B$ separated by $r = 1\,\text{Å}$ to be approximately $1\,\text{K}$ in temperature. Since

many materials order at much higher temperatures, the magnetic dipolar interaction must be too weak to account for the ordering of most magnetic materials.

Exchange interaction

Exchange interactions lie at the heart of the phenomenon of long range magnetic order. Exchange interactions are nothing more than electrostatic interactions, arising because charges of the same sign loose energy when they are close together and save energy when they are apart.

Consider a simple model with just two electrons with spins $\boldsymbol{S_1}$ and $\boldsymbol{S_2}$. The spin-dependent term in the effective Hamiltonian can be written

$$\mathcal{H}^{spin} = -2J\boldsymbol{S_1} \cdot \boldsymbol{S_2}. \tag{1.36}$$

If $J > 0$ then the minimum of energy is corresponding to the parallel spin alignment, triplet state. If $J < 0$ then the minimum of energy is corresponding to the antiparallel spin alignment, singlet state. This equation is relatively simple to derive for two electrons, but generalizing to a many-body system is far from trivial. Nevertheless, it was recognized in the early days of quantum mechanics that interactions such as that in Eq.1.36 probably apply between all neighboring atoms. This motivates the Hamiltonian of the Heisenberg model [32, 33]:

$$\mathcal{H} = -2\sum_{i>j} J_{ij}\boldsymbol{S_i} \cdot \boldsymbol{S_j}. \tag{1.37}$$

where J_{ij} is the exchange constant between the ith and j^{th} spins.

The calculation of the exchange integral can be complicated in general, but we here mention some general features. First, if the two electrons are on the same atom, the exchange integral is usually positive. This stabilizes the triplet state and ensures an antisymmetric spatial state which minimizes the Coulomb repulsion between the two electrons by keeping them apart. This is consistent with Hund's first rule.

When the two electrons are on neighboring atoms, the situation is very different. Let us consider a simple case of a hydrogen molecule H_2. Any joint state will be a combination of a state centered on one atom and a state centered on the other.
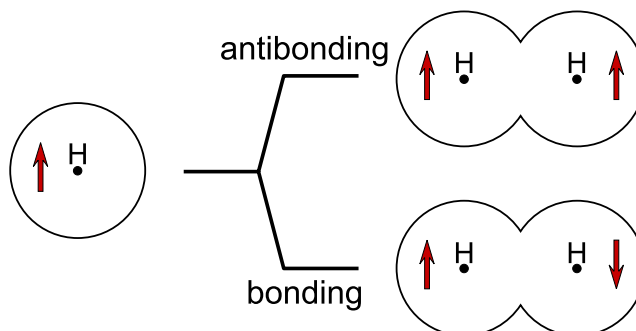
FIGURE 1.5: Exchange interaction in the H_2 molecule.

The electrons can save kinetic energy by forming bonds because this allows them to wander around both atoms rather than just one. The correct states to consider are now not atomic orbitals but molecular orbitals (see Fig.1.5). These can be bonding (spatially symmetric) or 'antibonding' (spatially antisymmetric), with the antibonding orbitals more energetically costly. This is because the antibonding orbital has a greater curvature and hence a larger kinetic energy since while moving electrons have to avoid each other due to the Pauli exclusion principle. This favors singlet (antisymmetric) states and the exchange integral is therefore likely to be negative.

The case of atoms with more than one electron is more complicated. To determine the ground state there is rule called Goodenough-Kanamori or Goodenough-kanamori-Anderson rule [34–37]. It states that the exchange interactions are anti-ferromagnetic if overlapping orbitals of neighboring atoms are half-filled, and they are ferromagnetic if one of overlapping orbitals of neighboring atoms is half-filled and another one is empty or filled.

Superexchange interaction

Besides the direct exchange interaction described above, there is also an indirect exchange. One of the mechanisms is known to be a superexchange. It can be defined as an indirect exchange interaction between non-neighboring magnetic ions which is mediated by a non-magnetic ion placed in between the magnetic ions. In the case of corner sharing metal ion-ligand configuration, it arises because there is a kinetic energy gain for antiferromagnetism. This can be understood from Fig.1.6,a which shows two transition metal ions (M) separated by an oxygen ion (O). For simplicity we will assume that the magnetic moment on the transition
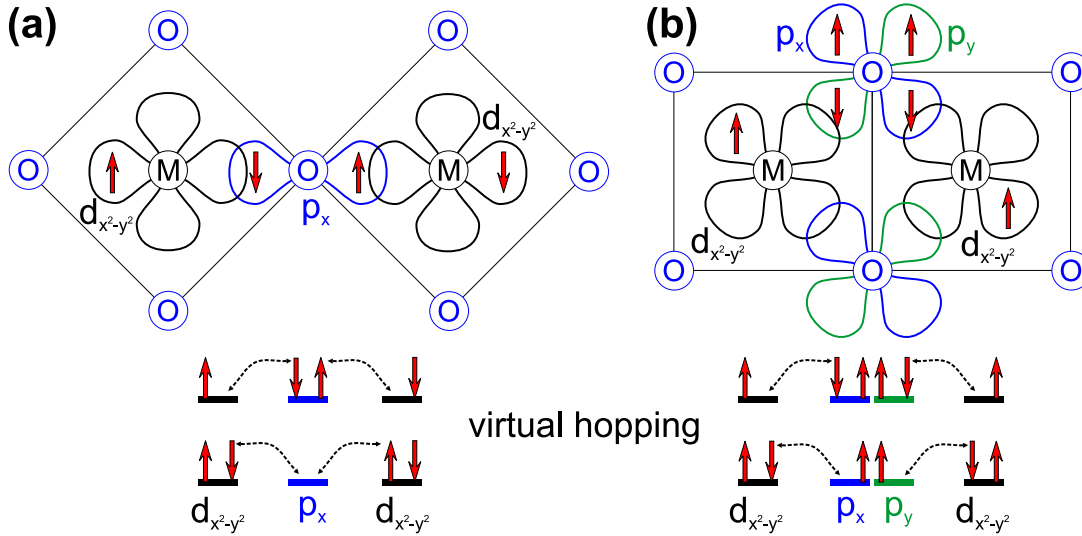
FIGURE 1.6: Super exchange between two transition metal ions through oxygen
p-orbitals; **(a)** corner sharing, antiferromagnetic coupling; **(b)** edge sharing,
ferromagnetic coupling.

metal ion is due to a single unpaired electron (more complicated cases can be dealt
with in analogous ways). Hence if this system were perfectly ionic, each metal
ion would have a single unpaired electron in a *d* orbital and the oxygen would
have two *p* electrons in its outermost occupied states. The figure demonstrates
that antiferromagnetic coupling lowers the energy of the system by allowing these
electrons to become delocalized through the virtual hopping process, thus lowering
the kinetic energy. Here the ferromagnetic coupling is not energetically favorable
due to the Pauli exclusion principle which would not allow the occupation of the
same orbital by the two electrons with parallel spin directions. In fact, the super-
exchange strength (energy) depends on the degree of the overlap of the orbitals
and its sign is strongly dependent on the angle of the M-O-M bond. Indeed, as
it is shown on Fig.1.6,b, in the case of 90° M-O-M bond angle the superexchange
should be ferromagnetic. Here during the virtual hopping process the electrons on
the p_x and p_y orbitals have parallel spins because of the Hund's rule coupling (see
Fig.1.6,b, bottom).

Double exchange interaction

In some oxides, it is possible to have a ferromagnetic exchange interaction which
occurs because the magnetic ion can show mixed valency, that is it can exist in
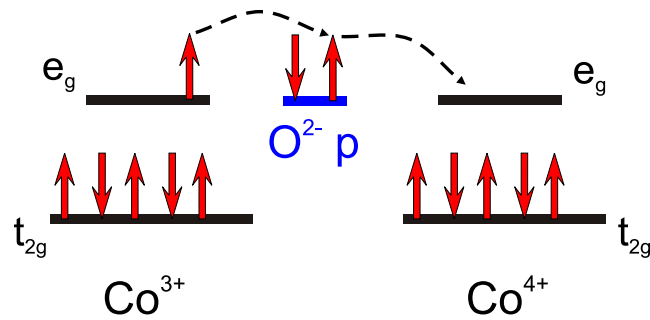more than one oxidation state. Examples of this include compounds containing the

FIGURE 1.7: Double exchange between Co^{3+} and Co^{4+} ions through oxygen p-orbitals.

Co ion which can exist in oxidation state 4+ or 3+. The ferromagnetic alignment is due to the double exchange mechanism [38] which can be understood from Fig.1.7. The e_g electron on a Co^{3+} ion can hop through the oxygen orbitals to a neighboring site only if there is a vacancy of the same spin direction (since hopping proceeds without spin-flip of the hopping electron). If the neighbor is a Co^{4+} which has no electrons in its e_g shell, this should be possible. However, there is a strong on-site (Hund's rule number 1) exchange interaction between the e_g electron and the five electrons in the t_{2g} level which keeps them all aligned. Thus it is not energetically favorable for an e_g electron to hop to a neighboring ion in which the t_{2g} spins will be antiparallel to the e_g electron. Ferromagnetic alignment of neighboring ions is therefore required to maintain the high-spin arrangement on both the donator and acceptor ion. Because the ability to hop gives a kinetic energy saving, the hopping process shown in Fig.1.7 reduces the overall energy. Thus the system ferromagnetically aligns to save energy.

Chapter 2

Electron Spin Resonance

2.1   Introduction

As an introduction to the ESR method here you can find a short historical overview
of the subject. The magnetic resonance age started when Stern-Gerlach in their
famous experiment showed that an electron magnetic moment in an atom can take
on only discrete orientations in a magnetic field [39, 40]. Shortly after, Einstein and
Ehrenfest gave few ideas of quantum transitions between magnetic energy levels
of atoms induced by the radiation [41]. Subsequently, Uhlenbeck and Goudsmit
[42] linked the electron magnetic moment with the concept of the electron spin
angular momentum. Breit and Rabi [43] described the resultant energy levels of
a hydrogen atom in a magnetic field. Rabi et al. [44] studied transitions between
levels induced by an oscillating magnetic field. Finally, the first observation of an
electron spin resonance peak, using the magnetic field of about $300\,\text{mT}$ and radio-
frequency of $133\,\text{MHz}$, was made in 1944 in Kazan (Russia) by Zavoisky during
his first experiments of resonance absorption in salts of transition metal ions [45].
Later on, the growing availability of the high (microwave) frequency emitters and
detectors and the development of the superconducting magnets enabled to increase
the measurement frequency and magnetic field which gave a possibility to extend
the range of physical properties and effects accessible with this method.

2.2   Phenomenon of Electron Spin Resonance

Let us consider a free spin $S = \frac{1}{2}$. If we apply the magnetic field, the spin states $|+\frac{1}{2}>$ and $|-\frac{1}{2}>$ split according to Zeeman effect (see Sec.1.6). If we expose this spin to a microwave radiation of a certain frequency ν matching the energy gap between these states then this radiation will induce the resonance transition of the spin state which will lead to the absorption of the microwave power. This resonance condition can be written as:

$$h\nu = g\mu_B H \tag{2.1}$$

Due to the quantum nature, a photon of a microwave radiation has a spin $s_{photon} = 1$, but it has no magnetic moment [46, 47]. This yields a selection rule for the change of the spin projection $\Delta S_z = \pm 1$. This selection rule is automatically fulfilled in the case of $S = \frac{1}{2}$, but it needs to be considered when dealing with higher spin values.

2.3   Spectrum parameters

The ESR experiment is mostly set up in the configuration when the MW radiation is kept constant and the magnetic field is swept. The result of such an experiment is the resonance absorption line (see Fig.2.1). Lets discuss parameters of this line.

Shape and width of the line

The shape of the line and its width might depend on different parameters. The intrinsic line shape and linewidth are determined by the lifetime of the spin in the exited state through the Heisenberg uncertainty principle [48]. In this case the line has a Lorentzian shape (Fig.2.2,a):

$$L = \frac{A}{1 + [2(H - H_0)/\Delta H_{1/2}]^2} \tag{2.2}$$

If there are mechanisms which increase the speed of the relaxation process, or in other words, decrease the lifetime, then the line homogeneously broadens. Such
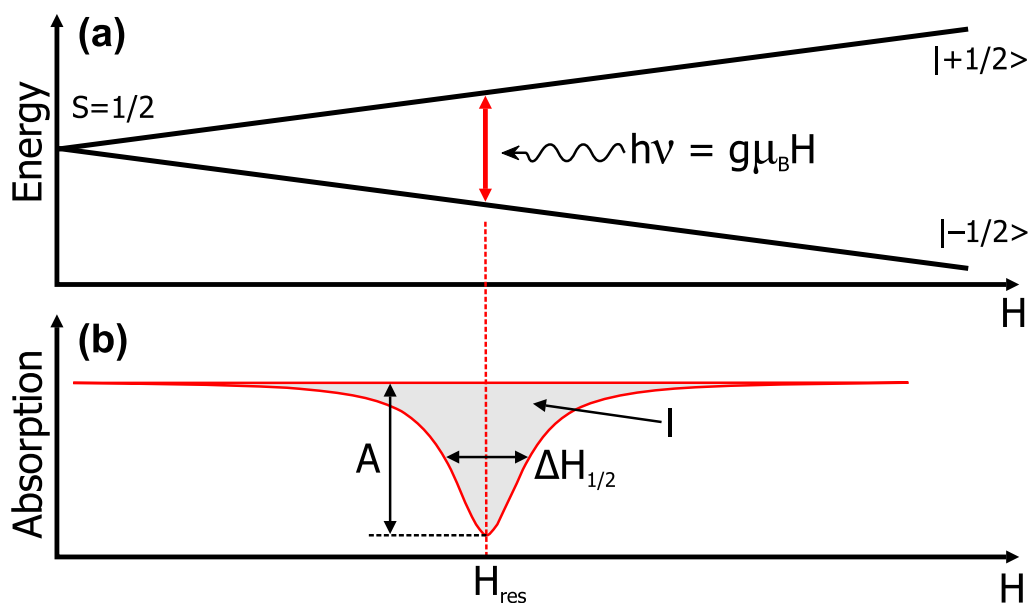
FIGURE 2.1: **(a)** Zeeman effect for a $S = 1/2$ system. At the resonance condition, microwave with energy $h\nu = g\mu_B H_{res}$ is absorbed by the spin; **(b)** resulting ESR line, A - amplitude, $\Delta H_{1/2}$ - full width at half maximum, H_{res} - resonance magnetic field, I - intensity.
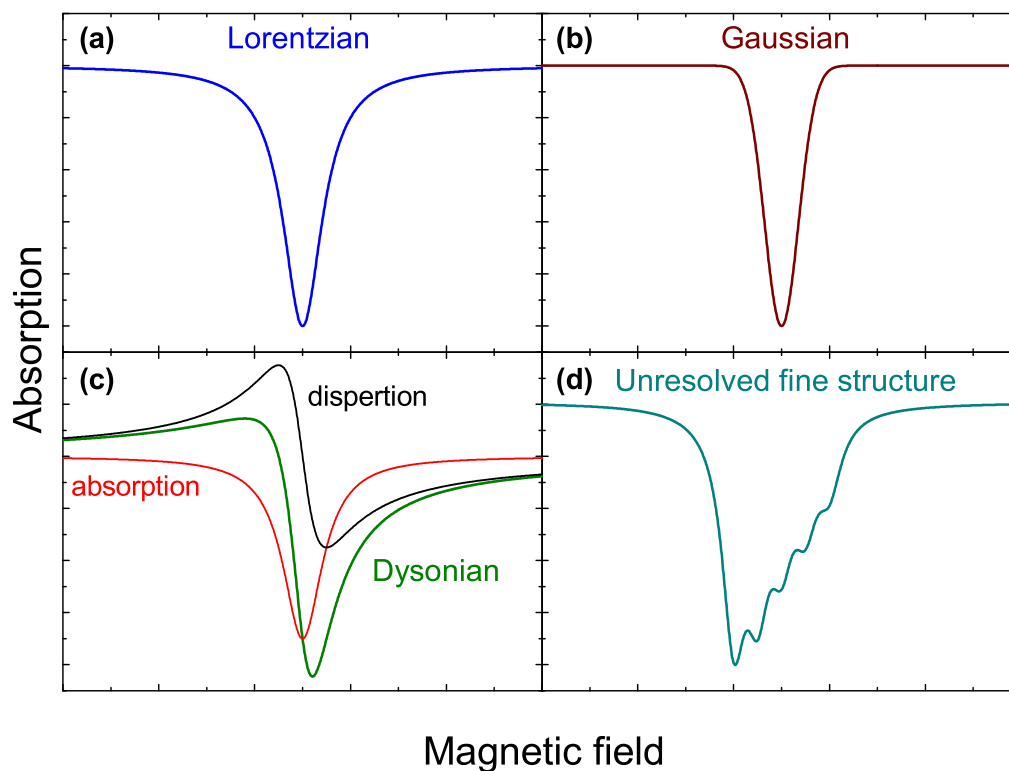

FIGURE 2.2: Examples of line shape.

mechanism is, for instance, spin-lattice relaxation. If the line broadens and changes its line shape then it is called the inhomogeneous broadening. For instance, the dipole-dipole interaction in the ensemble of spins, leads to the Gaussian line shape (Fig.2.2,b, Eq.2.3) since there is a random distribution of local magnetic fields at each spin.

$$G = 2Ae^{-\left(\frac{2(H-H_0)}{\Delta H_{1/2}}\right)^2} \tag{2.3}$$

If in this spin ensemble in addition there is an isotropic exchange interaction the ESR line will narrow. To understand this, one can consider an extreme case of an infinite exchange interaction when the whole ensemble behaves as a single spin. The result of the ESR experiment will be the Lorentzian line with intrinsic linewidth. Another important example of the inhomogeneous broadening is the broadening due to the unresolved fine structure. In this case neither Lorentzian nor Gaussian line shapes give a good fit for the line (Fig.2.2,d).

In the experiments with phase-locked detection, like in the case of Bruker x-band spectrometer with a cavity (see Sec.2.4.1), there is an effect of mixing of absorption of a microwave with dispersion if the sample has nonzero conductivity. This effect takes place due to the conduction electrons which absorb and re-emit the incident microwave. In this case the line shape is called Dysonian (Fig.2.2,c):

$$\begin{aligned} D &= A_{absorption} \frac{1}{1 + [2(H-H_0)/\Delta H_{1/2}]^2} \\ &+ A_{dispertion} \frac{[2(H-H_0)/\Delta H_{1/2}]}{1 + [2(H-H_0)/\Delta H_{1/2}]^2} \end{aligned} \tag{2.4}$$

Resonance field

Resonance field of the ESR line in the case of an isolated ion is determined by the g-factor (see Sec.1.2 and Sec.1.5).

The ion placed in the crystal field of ligands, depending of the symmetry, exhibits an additional shift of the resonance line due to the splitting of the energy levels. If to consider the simplest case of the spin $S = 1$ and uniaxial symmetry of the crystal field Eq.1.34, then the energy levels of such a spin placed in the magnetic field can be found using Hamiltonian:

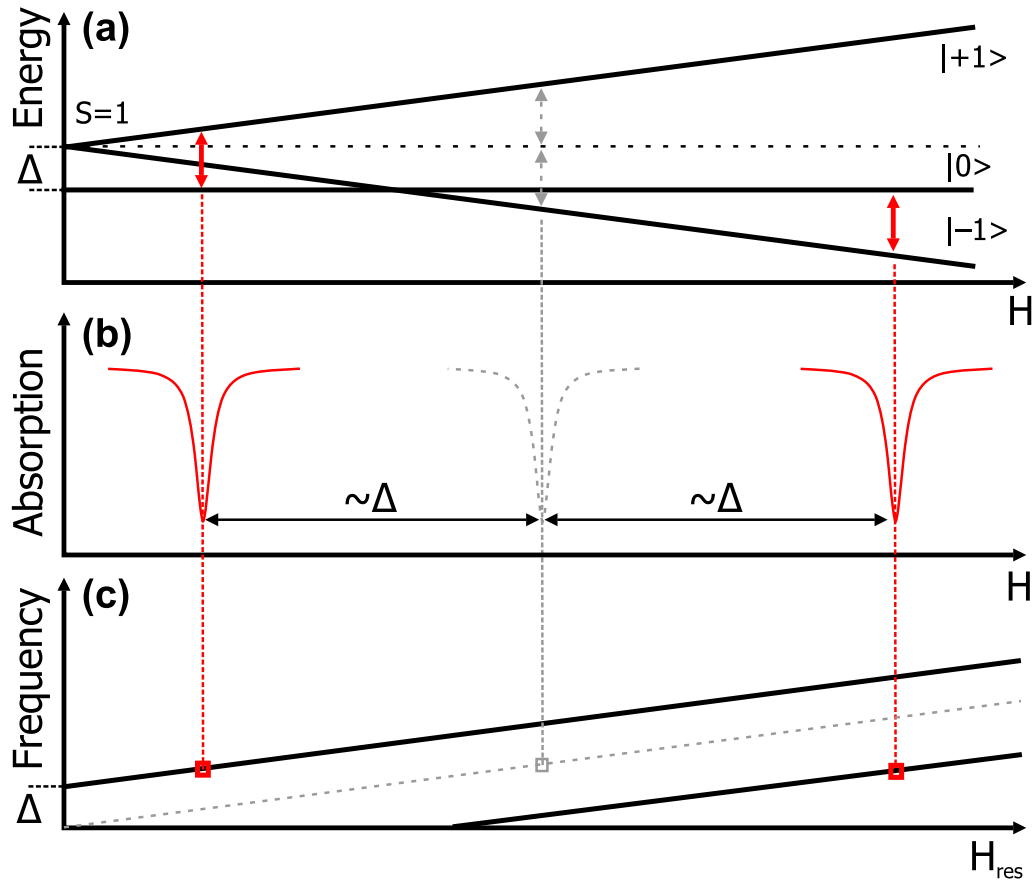$$\mathcal{H}^{uniaxial} = -g\mu_B H S_z + D(S_z^2 - \frac{S(S+1)}{3}) \tag{2.5}$$

FIGURE 2.3: Electron spin resonance of a spin $S = 1$ with splitting of the energy levels in zero magnetic field due to the crystal field. **(a)** energy levels dependence on an applied magnetic field; **(b)** resonance absorption lines, solid lines - with zero field gap, dashed - without zero field gap; **(c)** frequency as a function of resonance magnetic field for such system.

and they are depicted in Fig.2.3,a. In this case measuring the frequency dependence of the resonance field one can obtain the value of the energy gap (Fig.2.3,b,c).

In some systems, the interactions between different magnetic centers lead to the induction of the local internal magnetic field which can be added to or subtracted from the applied magnetic field. This leads as well to the shift of the ESR line since the resonance condition is changed according to:

$$h\nu = g\mu_B(H \pm H_{int}) \qquad (2.6)$$

with H_{int} being the internal magnetic field.

Integrated intensity

The integrated intensity I of the ESR line is proportional to the local spin susceptibility. In certain cases the integrated intensity can be calculated from the amplitude A of the signal and a full width at half maximum $\Delta H_{1/2}$. In the case of Lorentzian line the intensity is:

$$I_{Lorentz} = 1.57A\Delta H_{1/2} \tag{2.7}$$

In the case of Gaussian line the intensity is:

$$I_{Gauss} = 1.0643A\Delta H_{1/2} \tag{2.8}$$

2.4 ESR Instrumentation

2.4.1 X-band ESR spectrometer

The ESR measurements at 9.56 GHz (X-band) were performed by means of a commercial X-band Bruker EMX spectrometer with a Bruker rectangular resonator 4104OR-C/0801 [49]. The temperature control was carried out using a helium gas-flow cryostat and a temperature controller ITC503 (Oxford Instruments) which enables to set the temperatures between 3.4 K and 300 K.

2.4.2 High field - high frequency ESR spectrometer

Here the basics of high field - high frequency ESR spectrometer based on Millimeterwave Vector Network Analyzer (MVNA) are presented. More detailed information can be found in the PhD dissertations of C. Golze [50] and U. Schaufuss [51] and in Ref.[52].

High-field electron spin resonance (HF-ESR) experiments were performed with a spectrometer based on a Millimeterwave Vector Network Analyzer (MVNA) from AB Millimetre. This vector analyser is used for generation of millimeter- and submillimeter range microwaves and for phase-sensitive detection of a signal. MVNA enables to tune quasi-continuously the frequency of the microwave in the
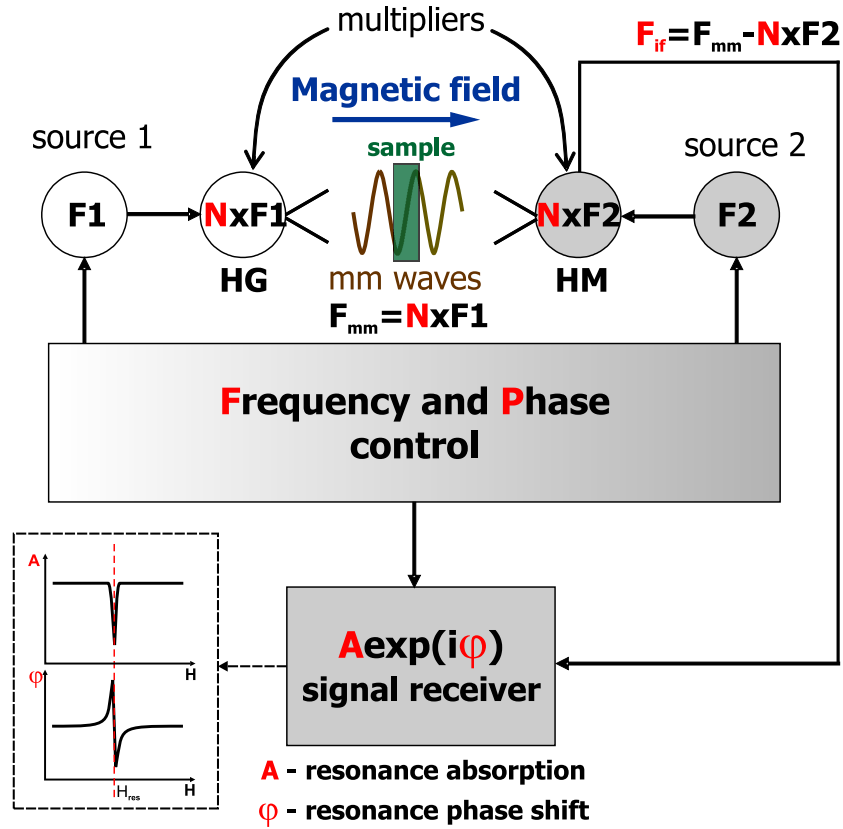
FIGURE 2.4: The principle scheme of the Millimeterwave Vector Network Analyzer

wide range from $16\,\mathrm{GHz}$ to $800\,\mathrm{GHz}$. The detection of changes in the amplitude and the phase of microwaves is realized electronically by application of non-linear solid state devices. The principle scheme of the MVNA is shown in Fig.2.4. Here, *source 1* generates a base frequency $F1$ which is further multiplied using a Schottky diode (harmonic generator HG). Then it is transferred to the sample by means of oversized wave guides (see below). After passing through the sample the microwave of a resulting frequency $F1 \times N$ is mixed on a second Schottky diode (harmonic mixer HM) with the reference microwave from *source 2* with frequency $F2 \times N$. Note here, that the reference frequency is slightly smaller by the value of $f = F1 - F2$, $f \ll F1, F2$. Mixing of the signals, or their multiplication, in practice is the generation of the harmonics with added and subtracted frequencies:

$$Acos(F1 + \phi) \times cos(F2) = \frac{1}{2}[Acos(F1 - F2 - \phi) + Acos(F1 + F2 + \phi)] \quad (2.9)$$

The last term can be filtered with a low-pass filter, and the first term contains the information about the amplitude A and the phase ϕ changes due to the resonance.

The filtering and the data acquisition is then performed by a signal receiver. Due to the phase sensitivity of the detection it is possible to obtain not only information about the absorption but also about the dispersion of the microwaves at the resonance.

To perform ESR experiments in high magnetic fields, the superconducting magneto-cryostat from Oxford Instruments was used in combination with MVNA. It is able to produce magnetic fields up to 15 T in normal mode operation and up to 17 T by pumping the helium in order to decrease the temperature of the superconducting coil. The variable temperature insert installed in the magneto-cryostat enables the precise stabilization of the temperature in the range between 2 K and 300 K.

The propagation of the microwaves to the sample placed in the cryostat in the magnetic field is realized by means of "oversized" wave guides, pipes with inner diameter much higher than a wave length of a microwave radiation. The multi-mode regime of such wave guides gives a possibility to tune quasi-continuously the frequency of a spectrometer. In Fig.2.5 two examples of probeheads based on such wave guides are shown. On the left the *transmission*-type is presented. Here the microwave emitted by the *source* is reflected from the 45° mirror and then directed towards the sample. It passes through the sample reflects twice from the 45° mirrors and thus propagates to the *detector* where the absorption and the phase shift are analyzed. This type of a probehead is suitable only for insulating samples since metallic samples are not transparent for microwaves, so they will reflect the microwaves back to the *source*. To measure ESR on metallic samples we use a *reflection*-type probehead presented on the right-hand side of Fig.2.5. Here the initial polarization of the microwave plays an important role. The vertically polarized microwave with electrical component E pointing up and down is emitted by the detector. The beam splitter, which is metallic grid, turned in the way that all the incident microwave of such a polarization is reflected down, towards the sample. At the resonance the polarization of the microwave rotates, so, after reflecting from the sample or from the bottom mirror, the part of microwave power passes through the beam splitter and induces a signal at the detector, which is then analyzed by MVNA. As can be seen such wave guide is suitable for metallic and insulating samples.
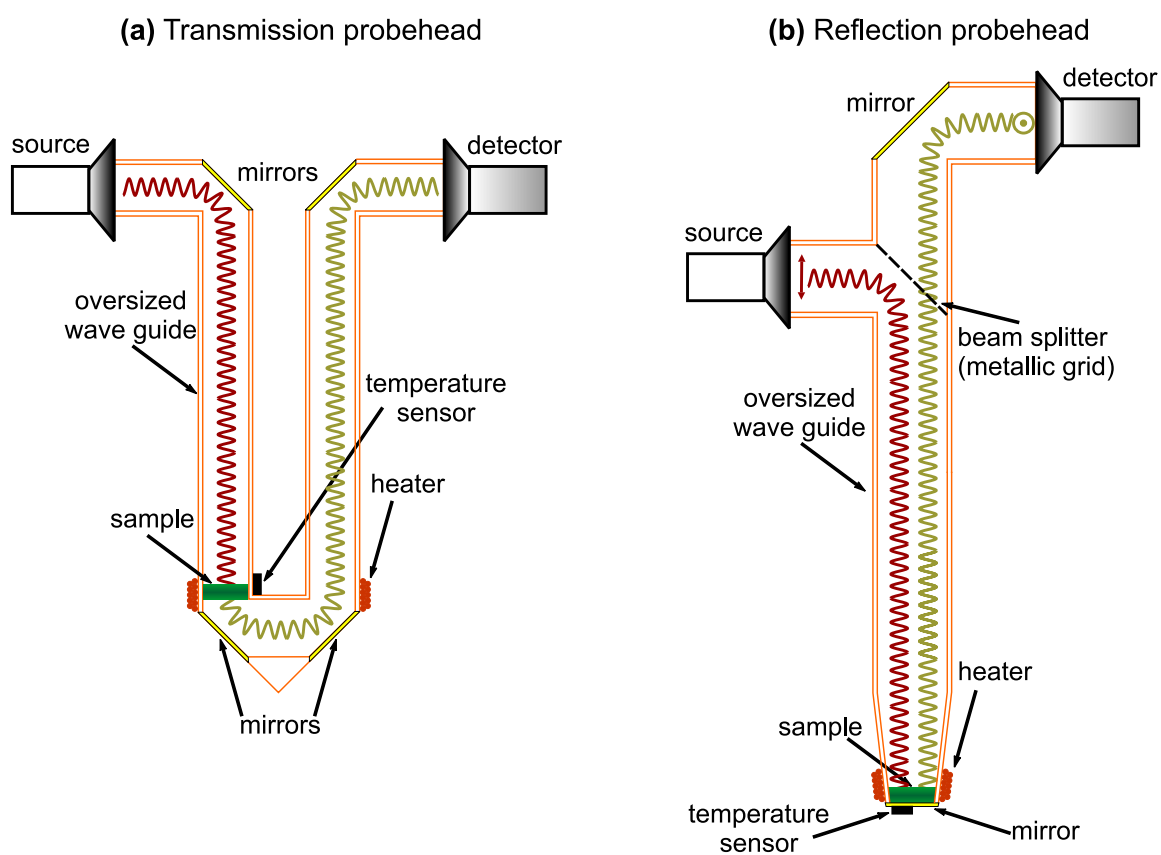
FIGURE 2.5: Probeheads based on multi-mode wave guides.

Chapter 3

$(\text{Gd,La})\text{O}_{1-x}\text{F}_x\text{FeAs}$ superconductors

3.1 Introduction

Iron-pnictide superconductors [53] with superconducting critical temperatures up to $55\,\text{K}$ [54–56] have attracted a huge interest due to striking similarities to superconducting cuprates [2, 3] as well as due to their original properties. Indeed, most families of these layered materials feature an antiferromagnetically (AFM) ordered parent compound, and the evolution of superconductivity concomitantly with suppression of AFM order upon doping (see Fig.3.2). However there are important differences which render the Fe-pnictides a separate new class of superconducting materials. Most striking of them are semi-metallicity and the spin density wave (SDW) character of the AFM order in the undoped pnictides contrasted with the Mott-insulating AFM state in the cuprates [2, 3], as well as a multi-band versus single-band electronic structure in the Fe-pnictide and cuprate high-temperature superconductors, respectively.

Beyond study of the superconducting ground state, and of the magnetic and associated structural transitions seen in the parent compound, much attention has been devoted to the issue of the ground states' coexistence. Discrepancies on this issue have been found between different families [55, 57–62], with the variation of the boundary of the two ground states and different length scales of coexistence, especially in the so-called 1111 family. This family has the composition $R\text{OFe}Pn$
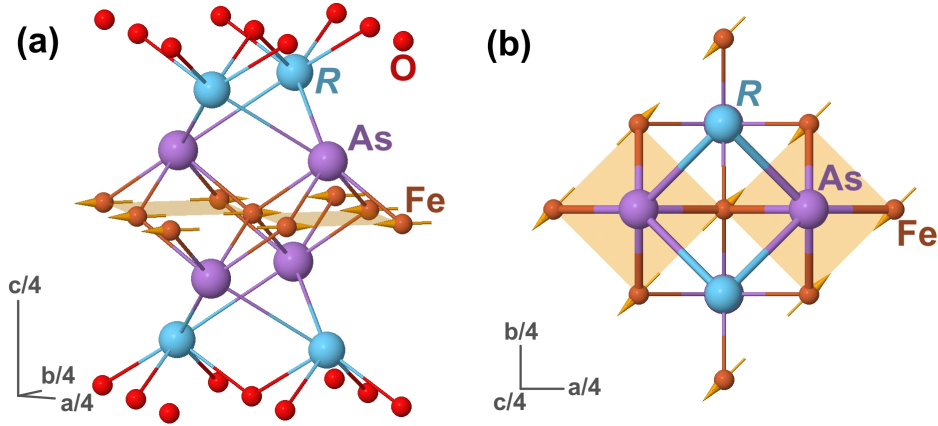
FIGURE 3.1: Crystal structure of 1111-type iron-pnictide and spin density wave antiferromagnetic ordering in Fe-layer.

(R - rare earth, Pn - pnictide) and exhibits a layered structure shown on Fig.3.1. The non-superconducting parent compound shows a structural transition from tetragonal to orthorhombic phase [56, 63] and an ordering of the Fe-layer in the antiferromagnetic spin density wave with the magnetic structure shown in Fig.3.1 [64]. The substitution of fluorine for oxygen induces the superconductivity in the Fe-layer. The replacement of one rare earth element with another can cause a significant variation of properties. Whereas in La-based *superconducting* samples there is evidence against static magnetic order in the FeAs planes (see Fig.3.2,a) [57], in the case of superconducting Sm-based samples evidence of remanent static magnetism is found (see Fig.3.2,b) [55]. The situation appears complicated due to the fact that the magnetism then tends to be of a short-range order or disordered, possibly even dynamic [65], which calls for the use of local probe techniques. These two different pictures complicate the establishment of the unified phase diagram for 1111 pnictides, necessary for the full understanding of these materials. In addition, as was shown by NMR [66, 67] and μSR [64] studies, there is a magnetic coupling between $4f$ (Ce, Pr and Sm) and $3d$ (Fe) moments. Such coupling of the rare earth to the FeAs plane might give an additional contribution to the difference in physical properties of different 1111-type superconductors.

In this part of the thesis two questions will be addressed, interaction of the Fe-layer with the rare earth element, here Gd, and the issue of coexistence of superconductivity and magnetism within Fe-layer. Firstly, this chapter starts with the investigation of lightly Gd doped $\mathrm{LaO}_{1-x}\mathrm{F}_x\mathrm{FeAs}$ where it is possible to probe local properties at the R site, such as crystal field and the internal magnetic field

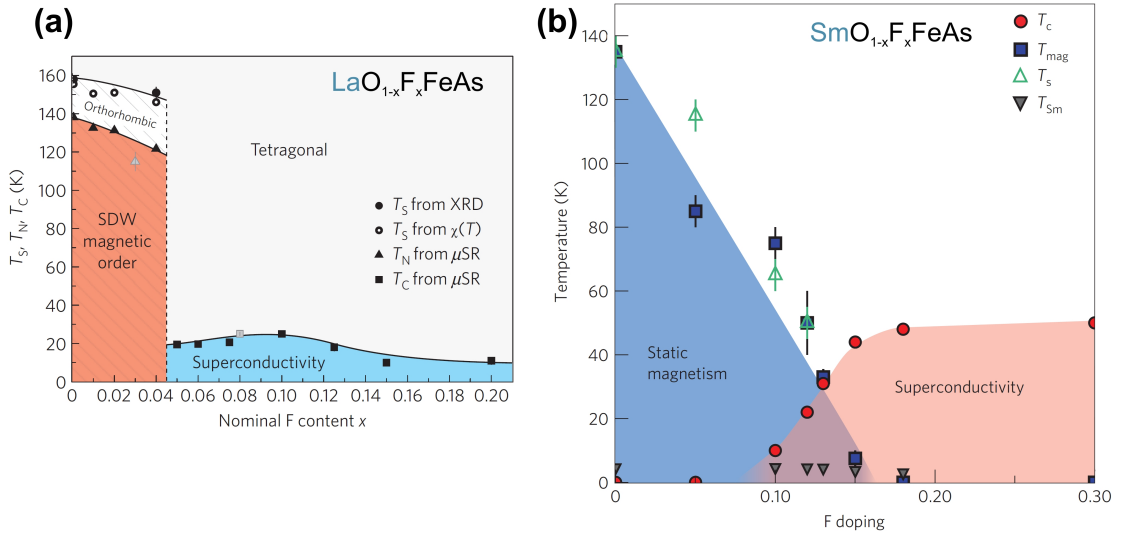FIGURE 3.2: Phase diagrams of 1111-type iron-pnictides; **(a)** $LaO_{1-x}F_xFeAs$ [57]; **(b)** $SmO_{1-x}F_xFeAs$ [55].

from the Fe-layer. The result is that Gd probes the structural changes in the compound and the appearance of the internal dipole field induced by the SDW ordered Fe-layer. Secondly, the result of the investigation of concentrated $GdO_{1-x}F_xFeAs$ compounds will be shown. In this material the ESR data reveal a significant exchange coupling of Gd- and Fe-moments in the parent GdOFeAs sample which enables the Gd^{3+} HF-ESR to probe sensitively the formation of the static SDW magnetic order in the FeAs planes. Interestingly, it is found that the signatures of such an order are still observed in the ESR spectra after doping. In particular, though long-range SDW order present at very low doping is suppressed at doping levels where superconductivity appears, our results imply static on the ESR time scale, likely short-range, magnetic correlations between Fe spins. This result suggests that $GdO_{1-x}F_xFeAs$ compounds may feature coexistence of quasi-static magnetism and superconductivity on a large doping range.

3.2   Sample preparation

Sample preparation was done by Dr. G. Behr, Dr. A. Köhler and Dr. S. Wurmehl. The polycrystalline samples of $GdO_{1-x}F_xFeAs$ ($x = 0, 0.15, 0.17$, nominal content) and $Gd_{1-y}La_yO_{1-x}F_xFeAs$ (x = 0, 0.1, and y=0.02, 0.05 nominal content) were prepared by two different routes. Route 1, which is similar to that described in
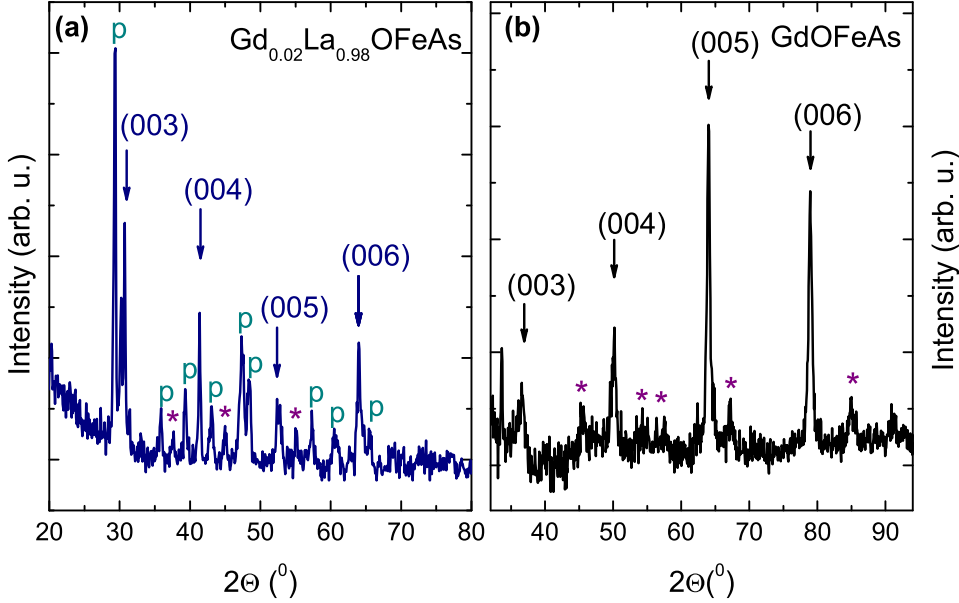
FIGURE 3.3: Powder x-ray diffraction data of the *c*-axis aligned GdOFeAs sample.

Ref.[68], starts with FeAs, Gd, Gd$_2$O$_3$, GdF$_3$ or FeAs, Gd, La, La$_2$O$_3$, LaF$_3$ in a stoichiometric ratio. All materials were homogenized by grinding in a mortar. Route 2 (only GdO$_{1-x}$F$_x$FeAs) uses GdAs, Fe, Fe$_2$O$_3$ and FeF$_3$ as starting materials in a stoichiometric ratio. Here, the starting materials were homogenized by grinding in a ball mill. In either case, the resulting powders were pressed into pellets under Ar atmosphere, and subsequently annealed in an evacuated quartz tube either in a two step synthesis at 940°C for 12 h and at 1150°C for 48 h (60 h) or in a one step synthesis at 940°C for 168 h.

In order to confirm the single phase character of the polycrystals, powder x-ray diffraction was performed on a Rigaku diffractometer (Cu K_α-radiation, graphite monochromator). The samples were either phase pure or contained insignificantly small amounts of GdAs, GdOF, and Fe$_3$O$_4$. The microstructure and the composition were examined by scanning electron microscopy (SEM, XL30 Philipps, IN400) equipped with an electron microprobe analyzer for semi-quantitative elemental analysis using the wave length dispersive x-ray (WDX) mode. The analysis showed that the GdO$_{1-x}$F$_x$FeAs sample with $x = 0.15$ (nominal content) in fact contains $\sim 0.07 \pm 0.02$ of F and $x = 0.17$ contains $\sim 0.14 \pm 0.02$ of F. Further on, we will use the doping levels obtained by WDX in order to label these samples.

For the *c*-axis alignment of the parent GdOFeAs sample, which was synthesized

under high pressure [69], and of the Gd$_{1-y}$La$_y$OFeAs ($y = 0.02, 0.05$) samples, the powder was mixed with epoxy resin and hardened while rotating in a magnetic field of 1.5 T. The x-ray diffraction data of the aligned powder samples were collected at room temperature using a PANalytical X'Pert PRO system (Philips) with Co K_α-radiation (Fig.3.3). The presence of highly intense [00l] reflections (Fig.3.3, arrows) which dominate the pattern points to a sufficiently good quality of the alignment in the case of all oriented samples. Reflections with Miller indices different from [00l] (Fig.3.3, asterisks) are visible in the background, too, but their intensity is strongly suppressed compared to the powder pattern. In Fig.3.3,a there are additional reflection, marked with symbol "p". They are attributed to the sample holder (plasticine).

3.3 Gd$_{1-y}$La$_y$O$_{1-x}$F$_x$FeAs

3.3.1 Sample characterization

Investigation of the static magnetic properties were performed by N. Leps and Prof. Dr. R. Klingeler. The temperature dependence of the susceptibility of 2% and 5% Gd doped LaOFeAs samples, shown on Fig.3.4,a,b as squares, can be fitted with high accuracy using Curie-Weiss [6] law (solid lines). This fit enables to estimate the actual content of the Gd ions doped in the sample. For the samples without fluorine doping, with nominal content of Gd of 2% the estimate from magnetization is $\approx 1.6\%$, with nominal content of 5% the actual content is $\approx 4.8\%$. For the sample with 5% of Gd and 10% of F the actual Gd content is $\approx 4.9\%$, the experimental data and the fit for this sample are not shown. In all cases the real content value does not differ significantly from the nominal one. Later to label the samples we will use nominal content values. By subtracting the Curie-Weiss fit from the measured data we extract the susceptibility of the Fe layer in these samples. The results of the subtraction are shown as dashed lines on Fig.3.4,a,b for both 2% and 5% doped LaOFeAs samples. It is clearly seen that at temperatures in the range from ~ 120 K to ~ 150 K there are changes in the susceptibility similar to that of the parent LaOFeAs sample [70]. This behavior is attributed to the structural changes in the samples and to the stabilization of the SDW order.
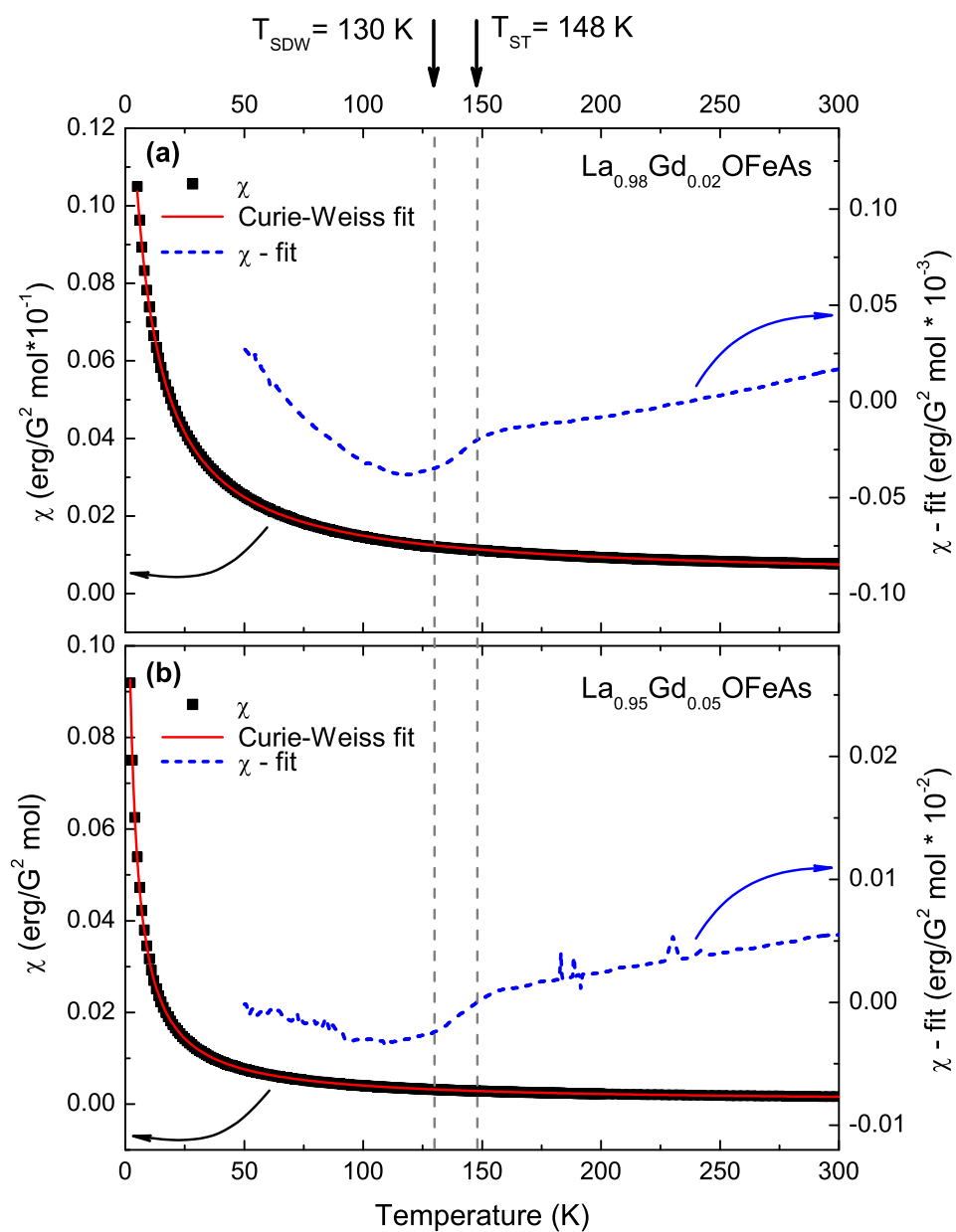
FIGURE 3.4: Magnetic susceptibility data measured on: **(a)** La$_{0.98}$Gd$_{0.02}$OFeAs; **(b)** La$_{0.95}$Gd$_{0.05}$OFeAs.
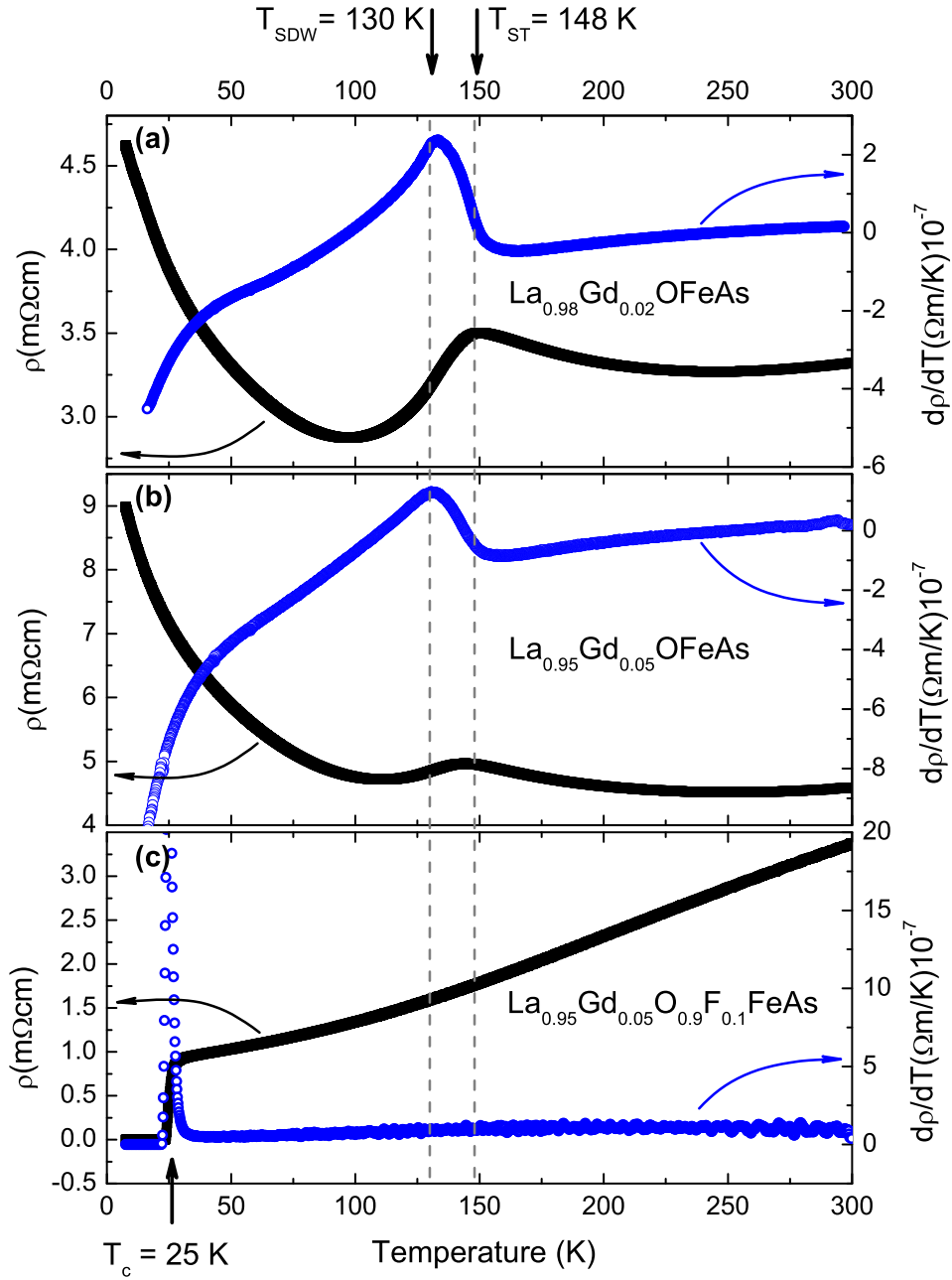
FIGURE 3.5: Electrical resistivity measurements performed on: **(a)** La$_{0.98}$Gd$_{0.02}$OFeAs; **(b)** La$_{0.95}$Gd$_{0.05}$OFeAs; **(c)** La$_{0.95}$Gd$_{0.05}$O$_{0.9}$F$_{0.1}$FeAs.

Investigation of transport properties was carried out by A. Kondrat and Dr. C. Hess. In order to precisely determine the phase transition temperatures (T_{ST}, T_{SDW} and T_c) of 2% and 5% Gd doped LaO$_{1-x}$F$_x$FeAs samples electrical resistivity measurements were performed. In the case of samples without fluorine doping (Fig.3.5,a,b) the resistivity shows qualitatively similar behavior to that of the LaOFeAs parent sample. The difference is in transition temperatures which are shifted to lower values, possibly due to increased disorder in the system. For 2% and 5% Gd doped sample transition temperatures are $T_{ST} = 148$ K and $T_{SDW} = 130$ K. The Gd$_{1-y}$La$_y$O$_{1-x}$F$_x$FeAs sample with 10% fluorine doping does not give any evidence for structural transition and SDW transition, but shows the superconductivity with $T_c = 25$ K (Fig.3.5,c).

3.3.2 X-band ESR

The typical powder ESR spectra are shown on Fig.3.6,a and Fig.3.6,b for 2% and 5% doped samples respectively. These measurements were done at X-band frequency of ~ 9.5 GHz and temperature $T = 130$ K. To fit the spectra we used two Dysonian lines, dashed lines in Fig.3.6,a,b. Later in the text they will be called broad and narrow components. The Dysonian ESR line shape is typical for metallic and semi-metallic system which the present samples are. The necessity to use two lines for the fit is explained by following. Gd^{3+} has an effective spin 7/2 and it is situated in the tetragonal/orthorombic crystal field due to the crystal lattice symmetry [56, 63]. Therefore, energy levels of the Gd^{3+} ion can be described using the effective spin hamiltonian in the generalized form [9, 10]:

$$
\begin{aligned}
\mathcal{H}_{eff} = g\mu_B \mathbf{H} \cdot \mathbf{S} &+ B_2^0 O_2^0 + B_4^0 O_4^0 + B_6^0 O_6^0 \\
&+ B_2^2 O_2^2 + B_4^2 O_4^2 + B_4^4 O_4^4 \\
&+ B_6^2 O_6^2 + B_6^4 O_6^4 + B_6^6 O_6^6
\end{aligned}
\tag{3.1}
$$

Here the first term accounts for the Zeeman energy and in the following terms O_n^m are Stevens operators describing the crystal-field (CF) interaction with parameters B_n^m. The schematic picture of energy levels and ESR spectrum corresponding to them according to Eq.(4.3) is shown in Fig.3.7,a. The ESR spectrum consists of seven absorption lines: the central transition $+\frac{1}{2} \leftrightarrow -\frac{1}{2}$ with the highest intensity and 6 satellites $\pm\frac{3}{2} \leftrightarrow \pm\frac{1}{2}$, $\pm\frac{5}{2} \leftrightarrow \pm\frac{3}{2}$ and $\pm\frac{7}{2} \leftrightarrow \pm\frac{5}{2}$. Such a structure of the line is called a fine structure splitting. In the case of an isotropic g-factor the
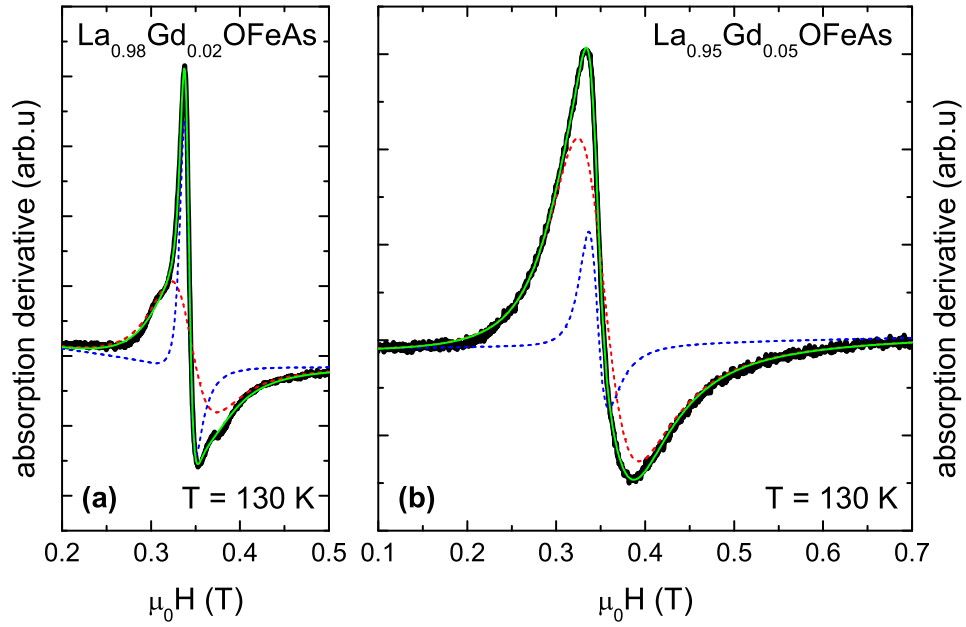
FIGURE 3.6: Two component fit of the ESR spectrum of: **(a)** La$_{0.98}$Gd$_{0.02}$OFeAs; **(b)** La$_{0.95}$Gd$_{0.05}$OFeAs
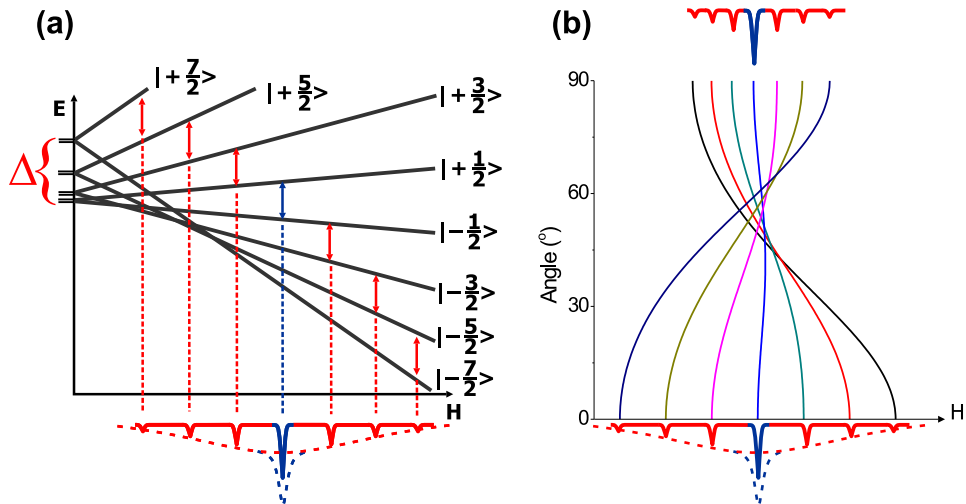
.

FIGURE 3.7: **(a)** Crystal field and Zeeman splitting of the energy levels of the Gd^{3+} ion and a corresponding ESR spectrum. **(b)** Angular dependence of this ESR spectrum.

resonance field of the main transition $(+\frac{1}{2} \leftrightarrow -\frac{1}{2})$, in contrast to the satellites, almost does not depend on the angle between the symmetry axis and the external magnetic field (see Fig.3.7,b). Hence, the powder averaging of the spectra, sum of all directions, leads to its transformation to a shape shown on Fig.3.6,a,b (see also S. E. Barnes [71], p.831). The information about the CF-splitting and the

accurate value of the magnetic field acting on the Gd ion which, in fact, defines the position of the central line can be extracted from the two component fit. The narrow component models the main transition. Its resonance field is determined by the local field at the Gd site. The broad component mimics the effect of the powder averaging of the satellites. Its width is therefore a measure of the CF splitting, and of the local magnetic field if there are magnetically nonequivalent Gd sites.

On Fig.3.8,a,b the temperature dependencies of the width δH of the broad component and the resonance field of the narrow component H_{res} are shown for the 2% and 5% Gd doped LaOFeAs samples. H_{res} is practically constant down to the temperature of the magnetic phase transition $T_{SDW} = 130\,\text{K}$ where it begins to shift to lower fields. The shift $\approx 0.007\,\text{T}$ is similar for both samples. At temperatures above T_{SDW} and T_{ST} there is gradual decrease of the width δH of the broad component and also of the narrow component with decreasing the temperature. Since both components exhibit narrowing, this behavior can be attributed to the Korringa relaxation of Gd spins on the conduction electrons, similar to the EuFe$_2$As$_2$ [72].

$$\delta H \sim (N(\epsilon_F)J)^2 T \tag{3.2}$$

The slope value, according to Eq.3.2 [71, 73], is proportional to the electronic density of states $N(\epsilon_F)$ and to the coupling J and it is equal to $\sim 0.45 \cdot 10^{-4}\,\text{T/K}$ in this case. With lowering temperature below $T_{ST} = 148\,\text{K}$ linewidth of broad component $\delta H(T)$ starts to increase and at $T_{SDW} = 130\,\text{K}$ there is a jump which is more pronounced in the case of the 5% doped sample. The initial broadening one can associate with changes in the fine structure of the Gd^{3+} ESR line and the jump at T_{SDW} can be associated with stabilization of magnetic order in Fe layer.

In contrast, the fluorine doped sample does not reveal any anomalies at temperatures above T_c (Fig.3.8,c). The Korringa slope found in this case is equal to $\sim 0.6 \cdot 10^{-4}\,\text{T/K}$. This value is significantly higher then that in the fluorine undoped case which suggests the increased density of states at the Gd ion after the charge doping.

To resolve the Gd^{3+} fine structure we have measured ESR on the 2% and 5% Gd doped LaOFeAs samples c-axis oriented in magnetic field. At temperatures above T_{SDW} and T_{ST} a single lorentzian line without a fine structure is observed. With decreasing the temperature the Gd^{3+} fine structure starts to develop and
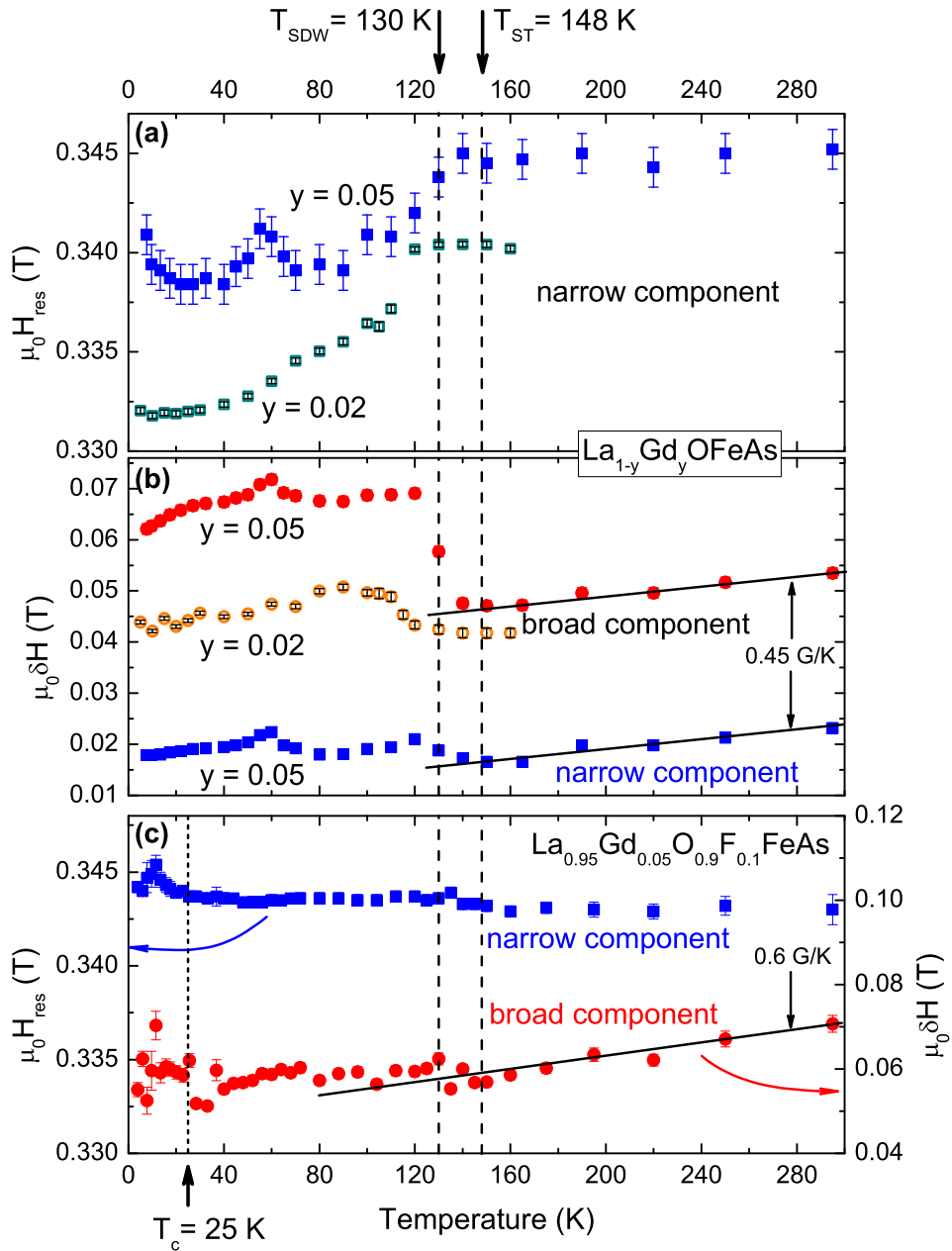
FIGURE 3.8: Temperature dependence of the resonance field of narrow component **(a)** and the linewidth of both components **(b)** of Gd doped LaOFeAs samples. **(c)** Temperature dependence of the linewidth (right) and resonance field (left) of $La_{0.95}Gd_{0.05}O_{0.9}F_{0.1}FeAs$ sample.
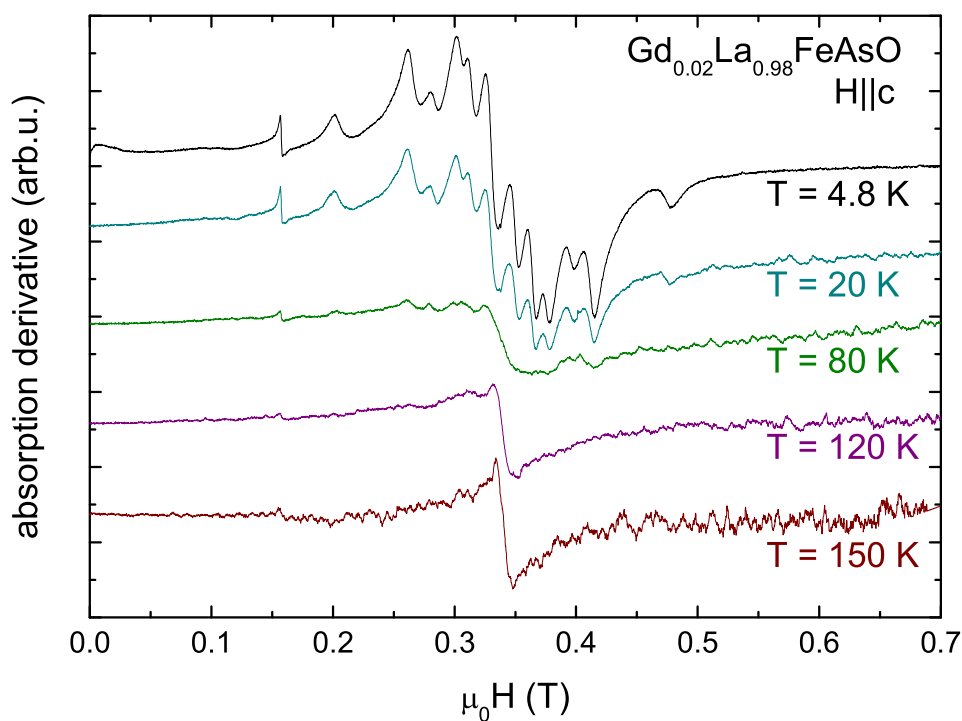
FIGURE 3.9: Temperature dependence of the ESR spectrum of 2% Gd doped
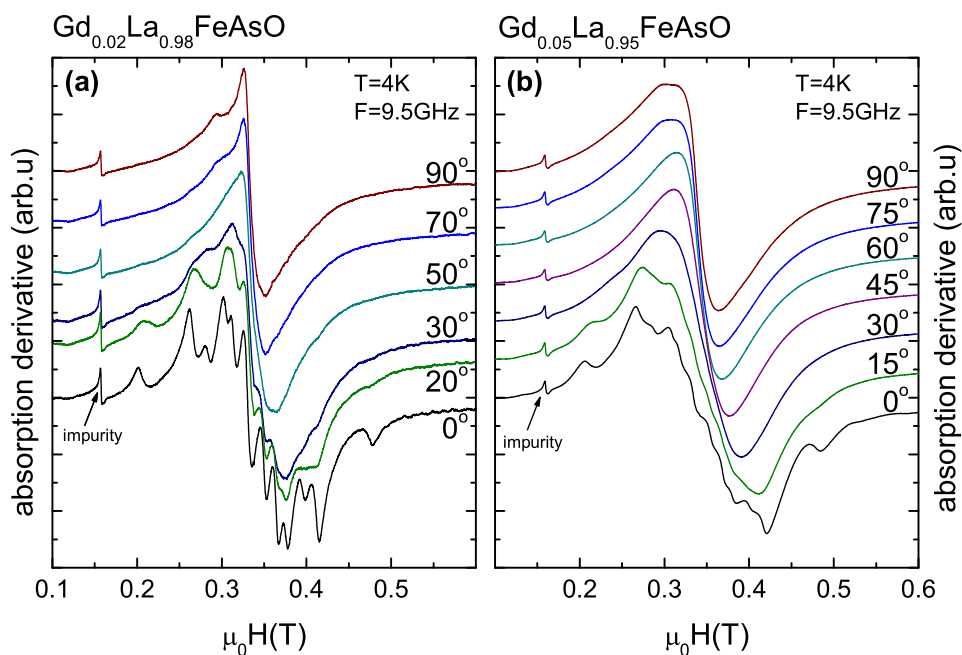*c*-axis oriented LaOFeAs sample with magnetic field parallel to *c*-axis.

FIGURE 3.10: Angular dependence the ESR spectra at low temperature of 2%
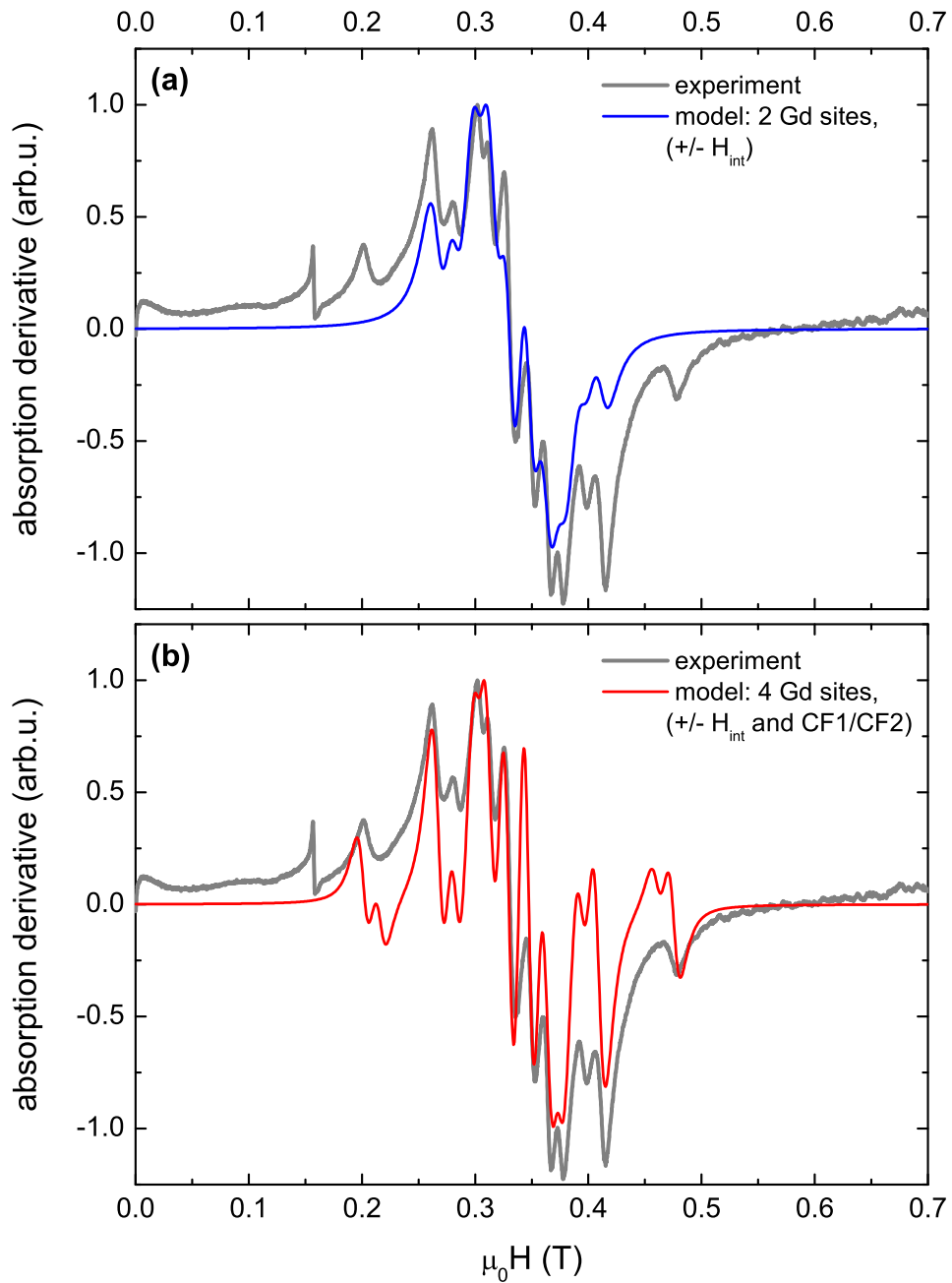**(a)** and 5% **(b)** Gd doped *c*-axis oriented LaOFeAs sample.

FIGURE 3.11: Theoretical simulation of the low-temperature ESR spectrum of c-axis oriented 2% Gd doped LaOFeAs sample assuming: **(a)** two nonequivalent Gd sites with different internal magnetic field H_{int}; **(b)** four nonequivalent Gd sites, two with different internal magnetic field H_{int} and two with different crystal field.
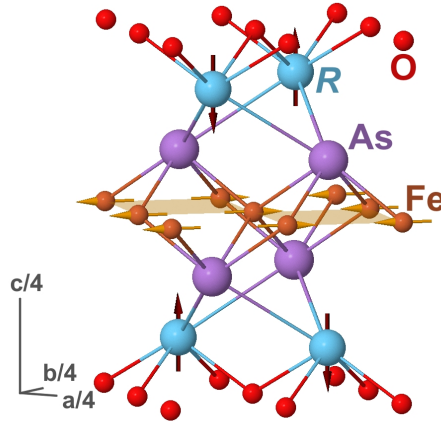
FIGURE 3.12: Two magnetically nonequivalent Gd sites, dark brown arrows depict dipolar field at the Gd/La ions produced by the SDW ordered Fe-layer.

becomes resolved at $T \sim 80\,$K (Fig.3.9). The absence of the fine structure in the ESR spectra at high temperatures can be explained by the poor signal to noise ratio due to a small susceptibility of Gd ions at high temperatures. On the angular dependence of the ESR spectra, measured at $T = 4\,$K, shown on Fig.3.10,a,b, one can see that the ESR line at lowest magnetic field, in contrast to other lines, does not exhibit any changes with varying the angle θ between magnetic field and c-axis of the sample. This leads to the conclusion that this line is not a part of the Gd signal and, most probably, is a signal from Fe impurity. As one can see on Fig.3.10,a,b, the best resolution is achieved for the smallest Gd concentration of 2% and for the direction of the external field parallel to the orientation axis of the samples (c-axis). In this case the spectrum consists of at least 12 absorption lines, but a single Gd^{3+} ion, according to its spin value $\frac{7}{2}$, may have maximum 7 lines. Straightforward explanation for that would be the SDW order in the Fe plane which creates the dipole field on the La/Gd site. According to the Fe spin alignment in the SDW, which is similar in the whole 1111-family of Fe-based superconductors (see Fig.3.1 and Fig.3.12), there are two magnetically nonequivalent positions of the La/Gd ion, where the internal field from the ordered Fe moments has the opposite sign (Fig.3.12). We performed the simulation of the Gd^{3+} spectra using the Hamiltonian (4.3) and assuming two magnetically nonequivalent positions. The best fit to the measured spectra is shown on Fig.3.11,a. The fit reproduces the middle part of the spectra rather well, but it lacks the most outer lines. To better recreate the measured spectra we had to use the model which includes not only two magnetically nonequivalent

positions (+/- H$_{int}$), but also two Gd sites with different crystal field parameters (CF1/CF2). Altogether this gives 4 different Gd sites. The best fit for this model is shown on Fig.3.11,b. The value of the internal magnetic field given by the fit is ~ 0.0078 T which is in the order of magnitude of possible dipolar field produced by Fe-layer.

3.3.3 Gd$_{1-y}$La$_y$O$_{1-x}$F$_x$FeAs summary

The ESR results on the lightly Gd doped LaO$_{1-x}$F$_x$FeAs samples establish Gd ions as a sensitive probe of magnetic and structural changes in the Fe planes. In the parent, i.e. not doped with fluorine, samples the change of the extent of the fine structure reflects the occurrence of the structural transition. In addition, the AF SDW order manifests in the shift and broadening of the powder spectra. The analysis of the spectra of the c-axis oriented sample yield 4 different Gd sites at low temperatures. Two magnetically nonequivalent positions are due to the SDW order in the Fe layer, which creates the alternating dipolar field on the Gd ions, and two positions with different charge environment. Crystal structure does not allow two different crystallographic Gd sites which yields the conclusion that different charge environments are probably due to the local disorder effects.

3.4 GdO$_{1-x}$F$_x$FeAs

3.4.1 Thermodynamic and transport measurements

Investigation of thermodynamic properties was carried out by N. Leps, L. Wang and Prof. Dr. R. Klingeler. In Fig.3.13,a, the temperature dependencies of the static susceptibility $\chi = M/H$ and the inverse susceptibility $\chi^{-1} = H/M$ of the GdOFeAs sample are presented. As $\chi(T)$ is dominated by the response of the Gd moments, the results are very similar for the F-doped samples, which are not shown. In general, the data obey the Curie-Weiss law which is expected due to the presence of paramagnetic Gd^{3+} ions. Note that the response of the FeAs-layers which is e.g. visible in LaOFeAs is about 3 orders of magnitude smaller and hence masked by the magnetism of the rare earth ions [74]. Analyzing the data in terms of the Curie-Weiss-law yields the antiferromagnetic Weiss temperature
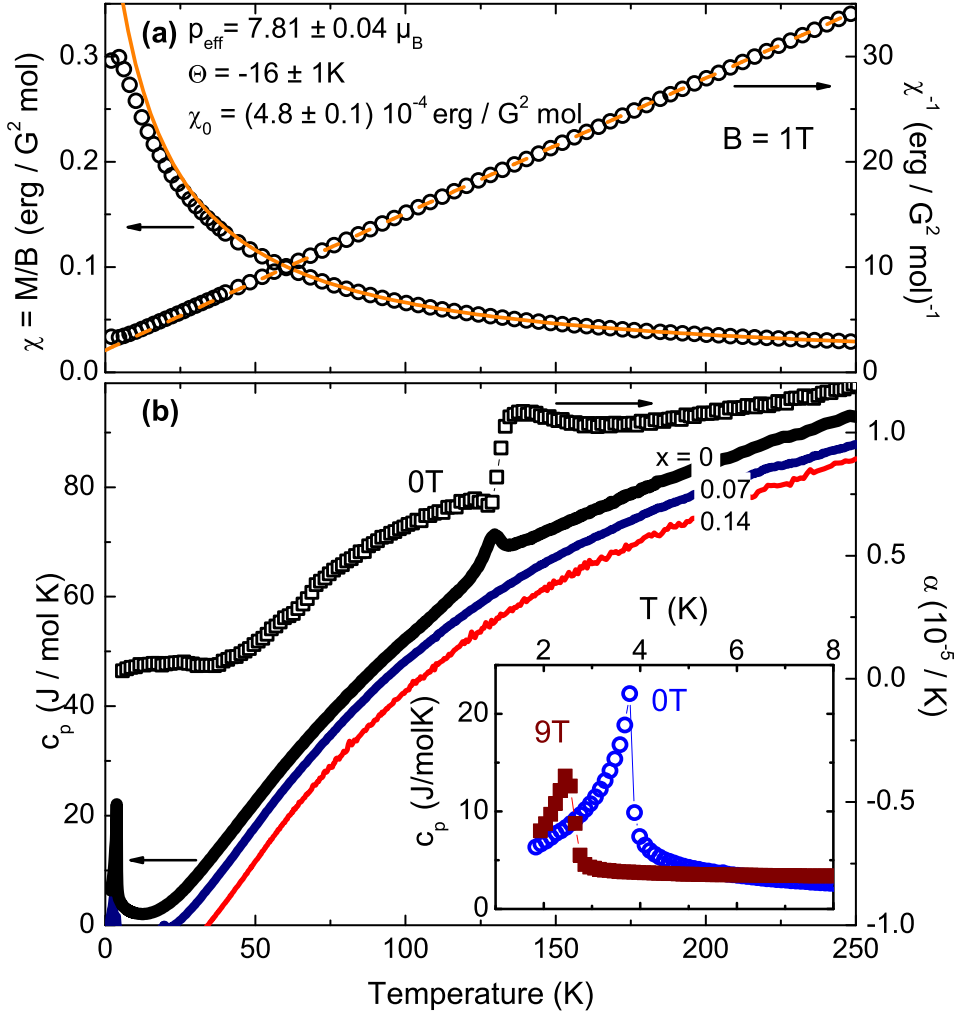
FIGURE 3.13: **(a)** Static susceptibility $\chi = M/H$ (left axis), χ^{-1} (right axis); **(b)** specific heat c_p (left axis) and thermal expansion coefficient α (right axis) of GdOFeAs vs. temperature; specific heat data for $x = 0.07$ and $x = 0.14$ samples is artificially shifted down for clarity; inset in **(b)** panel presents specific heat anomaly associated with long-range antiferromagnetic ordering of the Gd-moments at $\mu_0 H = 0$ and $\mu_0 H = 9\mathrm{T}$.

$\Theta = -16 \pm 1\,\mathrm{K}$ and the effective magnetic moments $p_\mathrm{eff} = 7.81 \pm 0.04\ \mu_\mathrm{B}$ which is close to the magnetic moment of a free Gd^{3+} ion ($p_\mathrm{eff} = 7.94\ \mu_\mathrm{B}$). At a low temperature of about $\sim 5\,\mathrm{K}$ there is a kink of the magnetization due to the AFM ordering of the Gd moments.

While the structural and magnetic phase transitions of the Fe-layer are not visible in the magnetization data, there are pronounced anomalies in the specific heat c_p and the thermal expansion coefficient α (Fig.3.13,b) in the case of the parent GdOFeAs sample. There is one broad feature visible in the specific heat data. In contrast, the thermal expansion coefficient exhibits two huge anomalies with
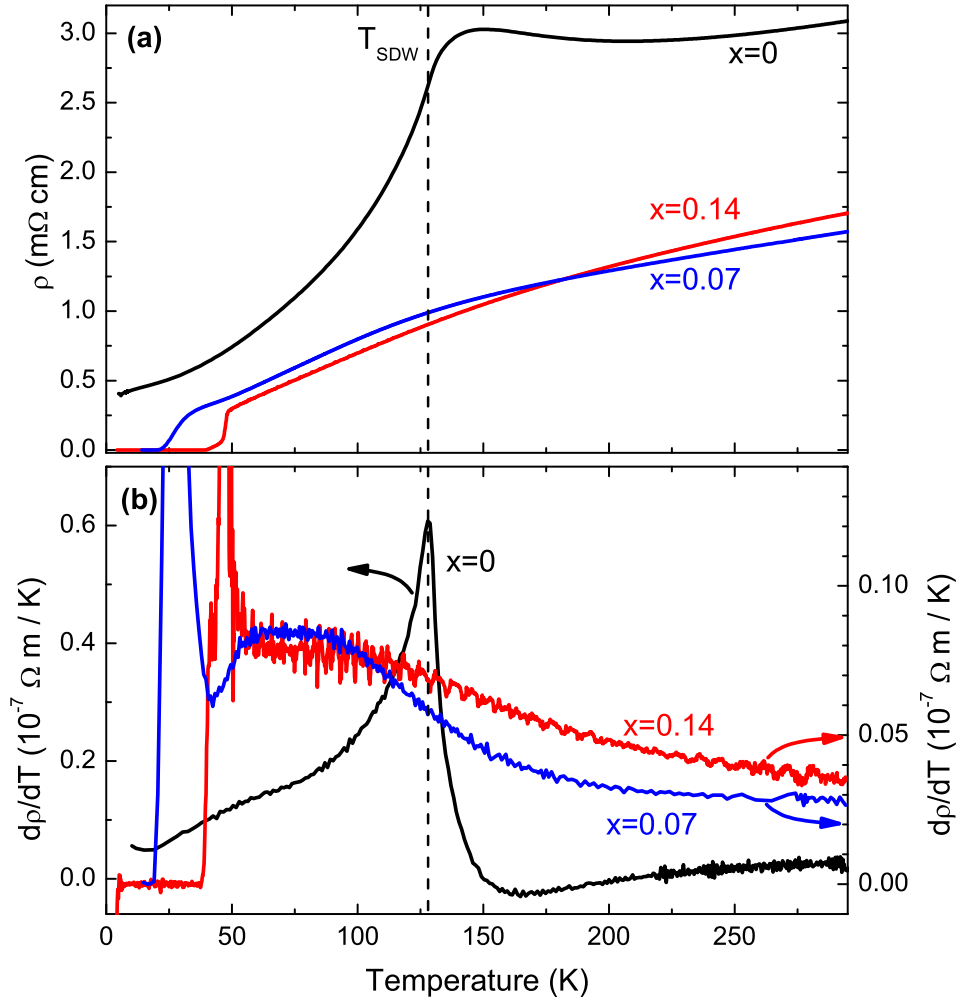
FIGURE 3.14: **(a)** Electrical resistivity ρ of GdO$_{1-x}$F$_x$FeAs samples, $x = 0$, 0.07, 0.14; **(b)** electrical resistivity derivative dρ/dT for $x = 0$ (left axis), $x = 0.07$, 0.14 (right axis).

opposite sign which can be attributed to the structural and SDW transitions of the compound at $T_{ST} = 136 \pm 5$ K and $T_{SDW} = 128 \pm 2$ K. In addition, the specific heat data reveal a sharp anomaly at $T_{\mathrm{NGd}} = 3.8$ K which is associated with the onset of long range antiferromagnetic order of the Gd moments, in accord with the magnetization data. Note that the anomaly is not present in the thermal expansion data due to the restricted temperature range $T \geq 6$ K. Upon application of external magnetic fields, Gd order is strongly suppressed as shown in Fig.3.13 (inset in the lower panel). T_{NGd} is shifted to 2.5 K in an external magnetic field of $\mu_0 H = 9$ T. While anomalies associated with Gd-ordering are still observed in the specific heat data of the F-doped samples with $x = 0.07$ and $x = 0.14$, there are no visible anomalies at higher temperatures (Fig.3.13,b). This evidences the absence of long-range SDW order in the doped, superconducting samples.

Investigation of transport properties was carried out by A. Kondrat and Dr. C. Hess. Fig.3.14,a shows the temperature dependence of the electrical resistivity ρ of the GdO$_{1-x}$F$_x$FeAs samples for all three doping levels: $x = 0$, 0.07 and 0.14. To get a better insight into the data we present the temperature derivatives $d\rho/dT$ in the bottom panel (Fig.3.14,b). The resistivity of the undoped material exhibits features closely connected to the structural and magnetic phase transitions: a maximum close to T$_{ST}$ and an inflection point at T$_{SDW}$ = 128 K, which are characteristic for all the 1111 parent compounds [56, 68, 70]. With doping, the electrical resistivity drastically changes its behavior, superconductivity emerges at low temperature and the intermediate temperature maximum disappears. The SC temperatures T_c for $x = 0.07$ and $x = 0.14$ samples amount to 20 K and 45 K, respectively. No pronounced features of the SDW phase are present in these compounds in the whole investigated temperature range. However, the normal state behavior of $\rho(T)$ for $x = 0.07$ is very unusual. At high temperatures the resistivity is linear down to approx 200 K, then it develops a curvature and drops below the linear approximation of the high temperature part. With decreasing temperature further, $\rho(T)$ becomes linear again and develops a slight opposite curvature at $T \lesssim 50$ K, prior to the onset of superconductivity. Upon increasing the F doping level in the samples, namely to $x = 0.14$, this anomaly becomes weaker. A similar drop of $\rho(T)$ at $T \lesssim 200$ K as found here has previously been observed for other 1111-type pnictide superconductors [56, 68, 75] as well as for Ba$_{1-x}$K$_x$Fe$_2$As$_2$ [76, 77]. The qualitative resemblance to the sharp drop at T_{SDW} which is observed in the respective parent compounds suggests that the resistivity drop in the superconducting samples is indicative of remnants of the SDW phase. In fact, a recent study of the Nernst effect on LaO$_{1-x}$F$_x$FeAs provides strong evidence that precursors of the SDW phase develop in the vicinity of the resistivity anomaly despite the absence of static magnetism [78].

3.4.2 GdOFeAs, 9.6 GHz X-band measurements

The ESR measurements performed at a frequency of 9.6 GHz on the c-axis aligned GdOFeAs sample in the whole temperature range of study and for both sample orientations ($H_{ext} \parallel$ or $\perp c$) reveal one broad line with the g-factor ~ 2 (Fig.3.15,a, inset). Such ESR response is typical for the systems where Gd^{3+} ions occupy regular positions in the crystal lattice with short distances between neighboring ions [71]. The Gd^{3+} is an S-state ion with a half-filled $4f$ shell which yields an

isotropic g-factor equal to 2 and a spin value of 7/2. The rather big spin value leads to strong magnetic dipole-dipole interactions which together with the unresolved fine structure broaden the ESR line. This broadening mechanism should lead to a Gaussian line shape which is however not observed in the spectra. Instead, the Lorentzian[1] function had to be used to fit the spectra (thin line in the inset in Fig.3.15,a) in order to obtain accurate values of the resonance field (H_{res}) and the linewidth. The Lorentzian shape suggests that homogeneous narrowing of the line does take place, which can be caused by isotropic exchange interaction between Gd spins [10, 71]. The temperature dependencies of H_{res} and the linewidth are shown on Fig.3.15,a,b. With lowering the temperature no drastic changes are seen in H_{res} down to $\sim 10\,\mathrm{K}$ where there is a strong shift of the line due to the ordering of Gd moments (Fig.3.15,a). The linewidth, in contrast to the resonance field, shows clear change in the behavior at $T_{SDW} = 128\,\mathrm{K}$ for both sample orientations (Fig.3.15,b). At temperatures above T_{SDW} there is a gradual decrease of the width of the ESR line upon cooling. This can be attributed to a Korringa-like behavior [71, 73], with the linewidth having a linear in T contribution due to the relaxation of the Gd spins through interaction with the conduction electrons (see Eq.3.2), similar to EuFe$_2$As$_2$ [72]. The slope value amounts to $\sim 0.9 \cdot 10^{-4}\,\mathrm{T/K}$ which is one order of magnitude smaller than that in EuFe$_2$As$_2$. A strong broadening of the line below T_{SDW} can be attributed to the SDW ordering in the FeAs layers. Similar effects in the Gd^{3+} ESR linewidth were observed before in the case of Gd$_2$BaCuO$_5$ samples where exchange coupling of Gd- and Cu-moments enabled to probe by means of Gd^{3+} ESR the magnetic ordering of the Cu layers [79] (see the discussion below).

3.4.3 GdOFeAs, high-frequency/field measurements

In the measurements performed at 9.6 GHz, the linewidth of the Gd^{3+} ESR signal is comparable to its resonance field. This leads to complications in the spectra analysis and to a lack of resolution. In order to improve the spectral resolution we performed high-frequency/field measurements on GdOFeAs samples. The high-temperature ESR spectra of the non-oriented GdOFeAs powder sample measured at a frequency of 328 GHz (Fig.3.16,a) consist of a single broad Lorentzian-shaped

---

[1]Note here that a Dysonian ESR line shape, which is typical for metallic samples in a cavity, is not observed here due to the fine grinding of the sample and further mixing with epoxy. This procedure reduces the microwave dispersion which is the origin of the Dysonian line shape.
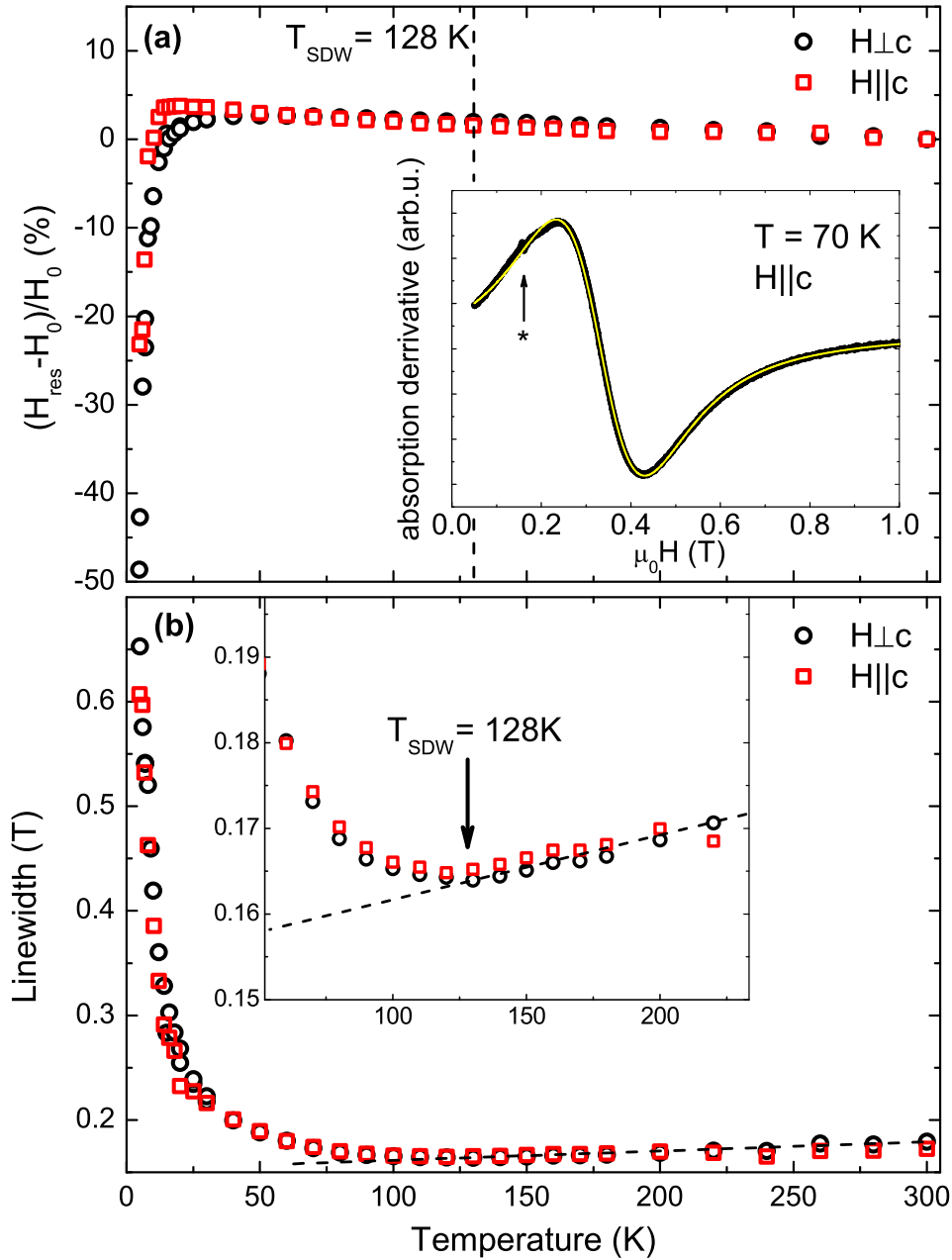
FIGURE 3.15: Results of the X-Band ESR ($\nu = 9.6$ GHz) measurements performed on c-axis aligned powder GdOFeAs sample for two sample orientations in the magnetic field, open circles - field in ab plane, open squares - field parallel to the c-axis; **(a)** temperature dependence of the resonance field on a reduced field scale $(H - H_0)/H_0$. Here $\mu_0 H_0 = 0.323/0.328$ T is resonance field at the highest temperature for $H \perp c/H \parallel c$; the inset shows the spectrum at $T = 70$ K in $H \parallel c$ configuration, the arrow points at a small Fe ESR signal which presence indicates a small amount of impurities; **(b)** temperature dependence of the linewidth; inset shows the change of the T-dependence at the SDW transition.
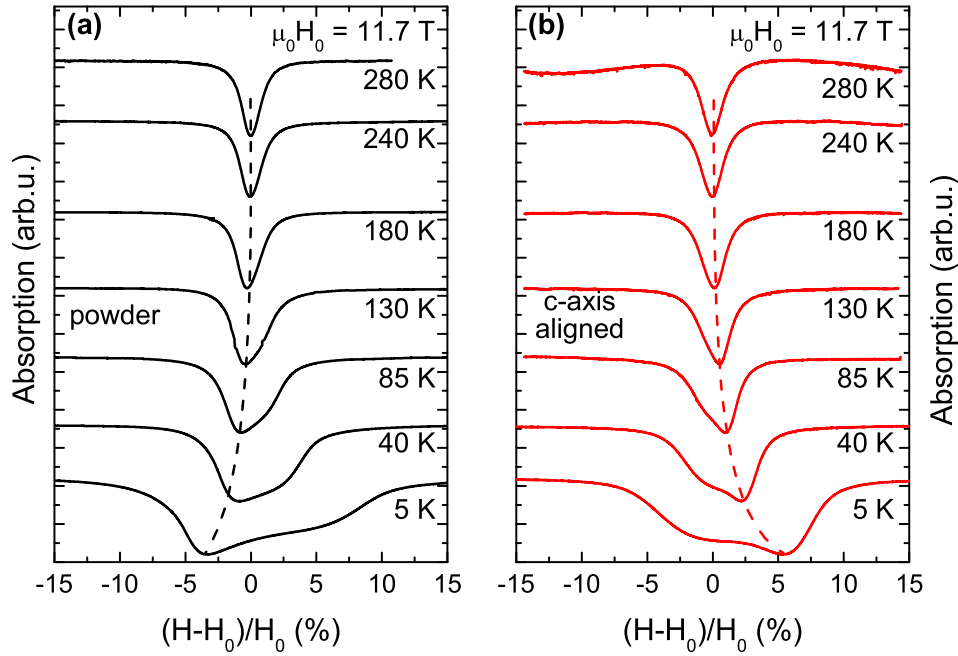
FIGURE 3.16: Temperature evolution of the high-frequency/field ESR spectra of GdOFeAs powder and c-axis aligned powder samples at a frequency of $\nu = 328\,\mathrm{GHz}$, shown on a reduced field scale $(H - H_0)/H_0$. Here $\mu_0 H_0 = 11.7\,\mathrm{T}$ is the resonance field of the signal at high temperature; **(a)** non-oriented powder; **(b)** c-axis oriented powder.

line with a g-factor of ~ 2 and a linewidth of $\sim 0.2\,\mathrm{T}$, similar to the low-frequency measurements. However, the very small Korringa contribution detected in the low frequency measurements is not visible in the HF-ESR spectra (Fig.3.21,a). The low-temperature HF-ESR spectra exhibit an inhomogeneously broadened shape which is in contrast to X-band data. As a measure of this broadening the full width at the half maximum (FWHM) of the signal ΔH has been taken (see Fig.3.21,a). As can be seen, with decreasing the temperature there is only a weak broadening of the signal down to a characteristic temperature $T_{if} \sim 150\,\mathrm{K}$ (if denotes an internal field at the Gd ion, see the discussion below) where substantial inhomogeneous broadening begins to develop continuously down to the lowest measured temperature of $4\,\mathrm{K}$. Concomitantly with the inhomogeneous broadening there is a noticeable shift of the minimum of the absorption to lower fields, as shown on Fig.3.17 (open circles) on a reduced field scale $(H - H_0)/H_0$. Here $\mu_0 H_0 = 11.7\,\mathrm{T}$ is the resonance field of the signal at high temperature. The spectral shape at low temperature (Fig.3.16,a) appears to be very similar to the shape of the ESR signal from a powder sample with an anisotropic g-factor. However, since the Gd^{3+} ion is a pure S-state ion, it should have an isotropic g-factor very close to 2. Hence
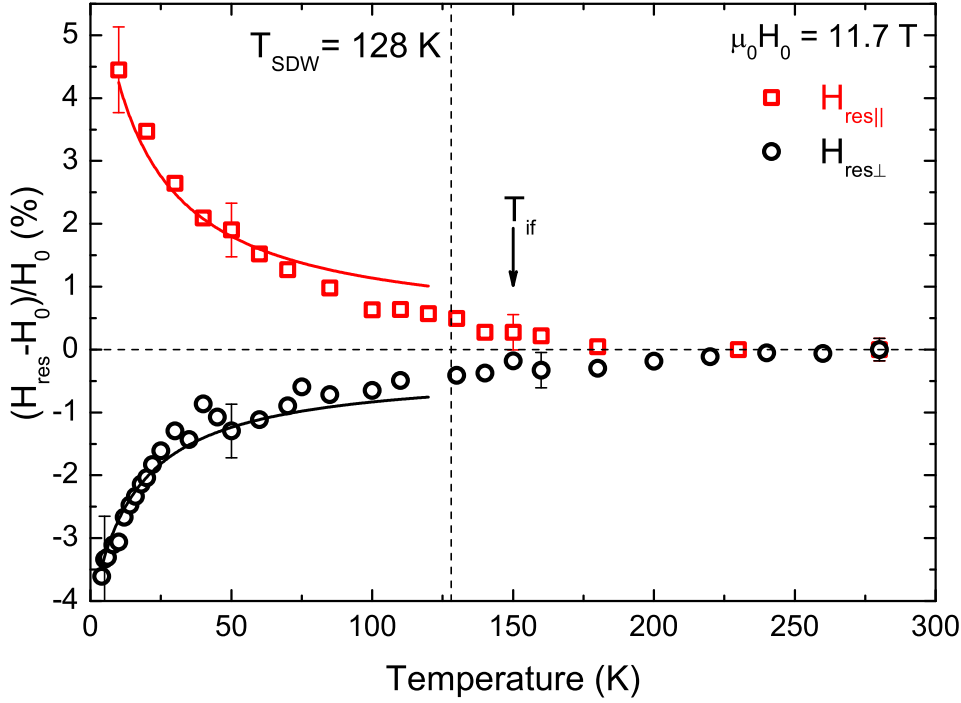
FIGURE 3.17: The shift of the minimum of absorption of the spectra with temperature, measured at a frequency of $\nu = 328$ GHz, on a reduced field scale $(H_{res} - H_0)/H_0$. Here $\mu_0 H_0 = 11.7$ T is the resonance field of the signal at high temperature; open circles - powder sample, open squares - c-axis aligned powder sample, solid lines - fits of the resonance field using Eq. 3.6.

one can conjecture that the shape of the ESR signal from the GdOFeAs sample is caused by the anisotropy of the internal field at the Gd site arising from the AFM-ordered Fe moments. In such an anisotropic powder situation most of the spectral weight is coming from the grains whose c-axes are oriented perpendicular to the direction of the external field H_{ext}. One should note here that in the case of in-plane anisotropy there will be an additional averaging effect due to the distribution of resonance fields of grains whose (ab)-planes are parallel to H_{ext}. Therefore we assume here that the low-field minimum of the absorption corresponds to the mean value of the resonance field of the Gd^{3+} ESR response ($H_{res\perp}$) in the case of the external field applied perpendicular to the c-axis. Correspondingly, the high-field shoulder of the spectra arises from grains whose c-axes make small angles with respect to H_{ext}.

In order to probe the Gd^{3+} response for the geometry $H_{\text{ext}} \parallel c$ we have performed ESR measurements on the c-axis oriented GdOFeAs powder sample. Though, according to the x-ray diffraction analysis, the alignment of the powder particles was not perfect, a substantial c-axis texturing of the sample has been achieved

(Fig.3.3). Similarly to the non-oriented powder sample, the c-axis oriented sample at temperatures above $\sim 150\,$K exhibits only a small broadening of the ESR spectrum with decreasing temperature (Fig.3.16,b). Below this temperature the signal experiences strong inhomogeneous broadening where most of the spectral weight is shifted to higher fields, which is opposite to the finding in the non-oriented powder sample. In the oriented sample most of the spectral weight and, consequently, the minimum of the absorption should correspond to the resonance field of the Gd^{3+} ESR response ($H_{res\parallel}$) in the geometry $H_{ext} \parallel c$ whereas a non-ideal powder alignment yields the low-field shoulder of the ESR signal.

From our measurements on non-oriented and c-axis oriented powder samples one can, therefore, extract the temperature dependencies of H_{res} in two configurations, i.e., for fields aligned along the c-axis ($H_{res\parallel}$) and in the (ab)-plane ($H_{res\perp}$), as summarized in Fig.3.17. As can be seen, the changes of both resonance fields $H_{res\perp}$ and $H_{res\parallel}$ start upon cooling at $T_{if} \lesssim 150\,$K and the shifts have opposite directions.

The qualitative difference in the high-field/frequency and low-field/frequency measurements leads to the conclusion that the shift of the resonance field and the inhomogeneous broadening of the spectra measured at a frequency of $328\,$GHz is a field-induced effect. To investigate it, we have measured the frequency ν versus magnetic field H_{res} dependence of the GdOFeAs powder and the c-axis aligned samples, respectively, both at $T = 280\,$K and $T = 4\,$K (Fig.3.18). At $T = 280\,$K the spectrum at all studied frequencies and fields consists of a single lorentzian line with the same linewidth value. A linear $\nu(H_{res})$ dependence has been revealed yielding a g-factor $g = h\nu/(\mu_B H_{res})$ equal to 2.005 (straight solid line on Fig.3.18). The spectra at $T = 4\,$K for the non-oriented powder (thin line) and c-axis oriented powder (thick line) samples at different frequencies together with the frequency dependence of the resonance fields $H_{res\perp}$ and $H_{res\parallel}$ are shown on Fig.3.18 as well. This measurement reveals that the difference between $H_{res\perp}$ and $H_{res\parallel}$ increases linearly with increasing the frequency and the field strength.

3.4.4   GdOFeAs, discussion

Since the inhomogeneous broadening and the shift of the Gd ESR signal set in close to the SDW ordering temperature, one can associate them with the interaction of the Fe ordered moments with the Gd spins. The shifts of $H_{res\perp}$ and $H_{res\parallel}$ from
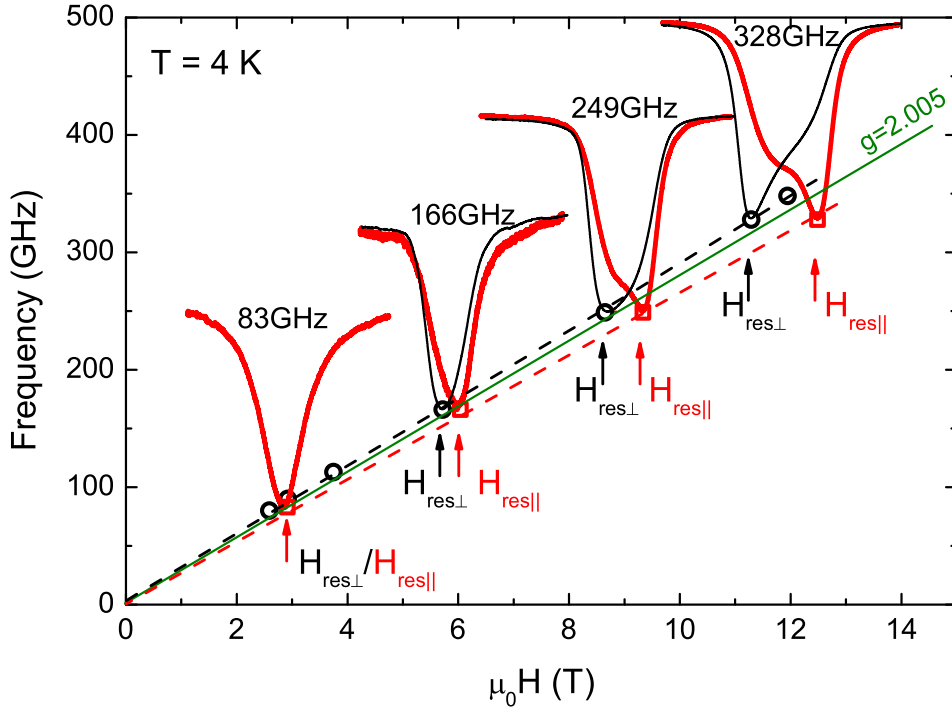
FIGURE 3.18: Frequency dependence of the ESR signal from GdOFeAs non-oriented powder and c-axis oriented powder samples measured at $T = 4$ K; data points correspond to the position of the minimum of absorption of the spectra at different frequencies, open circles - non-oriented powder sample, open squares - c-axis oriented powder sample, dashed lines - guides for the eyes, solid line - the frequency dependence of the position of the high-T Gd ESR line measured at $T = 280$ K; the lineshape of the spectra is shown as well, thin solid line - non-oriented powder, thick solid line - c-axis oriented powder.

a common high-temperature paramagnetic value H_0 can hence be related to the occurrence of an internal magnetic field ($H_{int\perp}$ and $H_{int\parallel}$) at the Gd site due to the formation of the static SDW in the FeAs layer. Based on the dependence shown on Fig.3.18 we can conclude that the strength of these internal fields depends on the strength of the applied magnetic field.

When the FeAs planes are in the paramagnetic state, at temperatures above $T_{SDW} = 128$ K, the exchange/dipolar field at the Gd position is negligible as the applied magnetic field cannot effectively polarize small paramagnetic moments at elevated temperatures. At temperatures below $T_{SDW} = 128$ K the Fe moments order *statically* in the (ab)-plane. The AFM structure of the magnetic order (see Fig.3.1), which is similar for all R-based 1111-type pnictides can be found in Ref.[64]. Due to symmetry reasons, without an applied magnetic field the internal field at the Gd site can be only of dipolar nature and in this case according to an

estimate it should not exceed $\sim 0.03\,\text{T}$. We suggest that application of an external magnetic field induces tilting of the Fe spins and hence creates an uncompensated magnetic moment (m_{Fe}) in the direction of the external field[1]. This moment can interact with the Gd^{3+} spins which would effectively lead to the occurrence of an additional internal field. If $H_{ext} \perp c$, then the Fe spins tilt in the ab plane as it is schematically shown on Fig.3.19,a,b for the configuration where H_{ext} makes an angle of 90° with the AFM ordered Fe spins. The shift of the ESR line $H_{res\perp}$, measured at $328\,\text{GHz}$, yields an estimate of the internal field ($H_{int\perp}$) of about $\approx 0.4\,\text{T}$ parallel both to H_{ext} and to the uncompensated moment m_{Fe} in the FeAs plane. If $H_{ext} \parallel c$, then the Fe moments tilt out of the plane (Fig.3.19,c,d). In this case the shift of the ESR line, measured at $328\,\text{GHz}$, yields an estimate of the internal field ($H_{int\parallel}$) of about $\approx 0.65\,\text{T}$ antiparallel both to the H_{ext} and to the uncompensated moment m_{Fe}. One should note here that an estimate of the dipolar field produced by the FeAs layers at the Gd site yields a value which does not exceed $\approx 0.05\,\text{T}$ even for full out-of-plane canting. This field is one order of magnitude smaller than the experimentally observed value which clearly implies the presence of an appreciable exchange interaction between Gd and canted Fe moments. The dependence of the sign of the internal field on the direction of the applied magnetic field suggests that the sign of the exchange interaction with Gd spins is different for different directions of the uncompensated Fe moments, i.e., ferromagnetic for the in-plane and antiferromagnetic for the out-of-plane directions. This surprisingly strong anisotropy of the exchange might be related with the multiband electronic structure of iron pnictides which might give rise to different pathways for interactions between the Gd $4f$ orbitals and the in-plane xy and out-of-plane xz and yz Fe $3d$ bands. Note that, in zero magnetic field and hence without Fe spin canting, the exchange interaction between Fe and Gd moments of an arbitrary sign is geometrically frustrated (see Fig.3.19). The application of a field which tilts the Fe moments thus removes this frustration.

Considering the exchange interaction, one might suppose that the temperature dependence of the internal field at the Gd site should follow the behavior of the SDW order parameter in 1111 compounds (see Fig.3.20) [57, 64, 70, 80], which increases fast within $\sim 30\,\text{K}$ starting at T_{SDW} and then stays almost constant with further decreasing the temperature. Here, the internal field acting on the Gd^{3+}

---

[1]For simplicity which does not affect the conclusions of the following qualitative discussion, we assume hereafter that the uncompensated magnetic moments and thereby created internal fields are collinear with the applied magnetic field.
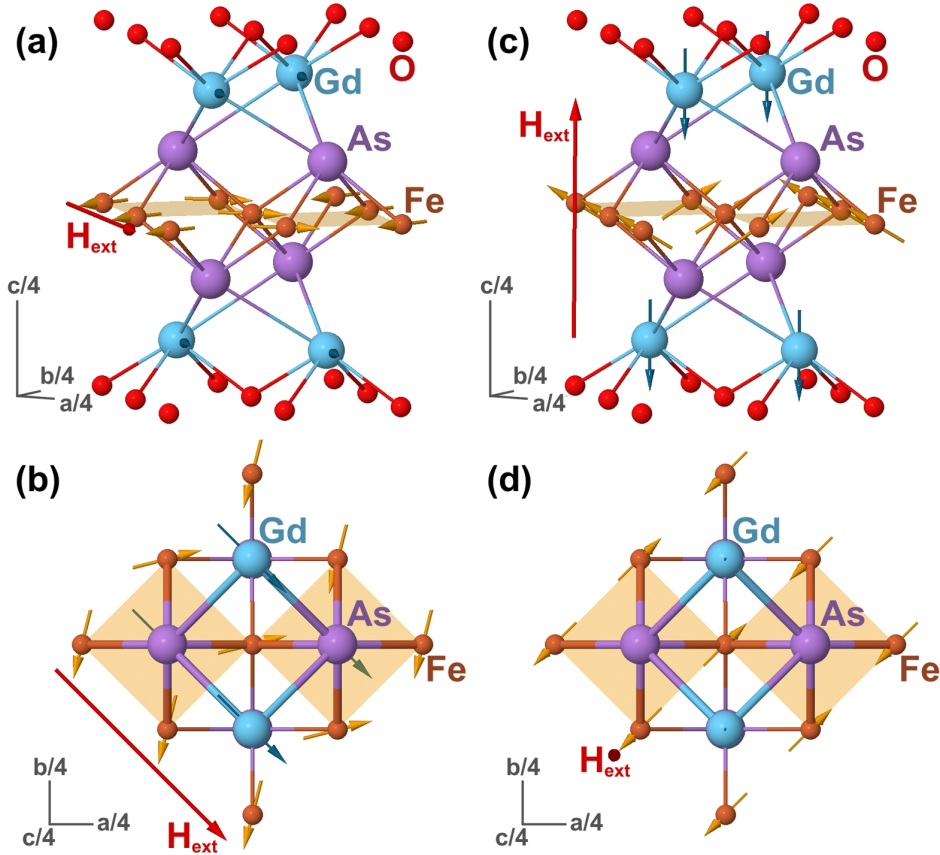
FIGURE 3.19: Canting of the Fe moments due to the applied magnetic field H_{ext}; **(a),(b)** $H_{ext} \perp c$ (the angle between H_{ext} and Fe AFM ordered moments is 90°); **(c),(d)** $H_{ext} \parallel c$; arrows on the Fe site depict magnetic moments, whereas arrows on the Gd sites represent the induced internal field.

moments arises at a temperature $T_{if} \approx 150$ K which is ~ 20 K higher than $T_{SDW} = 128$ K and keeps increasing upon cooling till the lowest measured temperature (see Fig.3.17). When approaching the temperature of the SDW transition from high temperatures, the appearance of the internal field well above T_{SDW} can be explained by growing quasi-static correlations between the Fe moments seen in the time window of the high-frequency ESR. The development of the internal field below T_{SDW} is found to be similar to that of some other systems where paramagnetic ions are coupled to magnetically-ordered moments of another type [81, 82]. To explain this evolution of the internal field we use a simple model based on a mean-field approximation [6, 71].

To simplify the calculations we assume that a magnetic field and magnetic moment vectors are collinear. In this model, the internal field at the Gd site H_{int} is proportional to the magnitude of the uncompensated Fe moment m_{Fe} with a
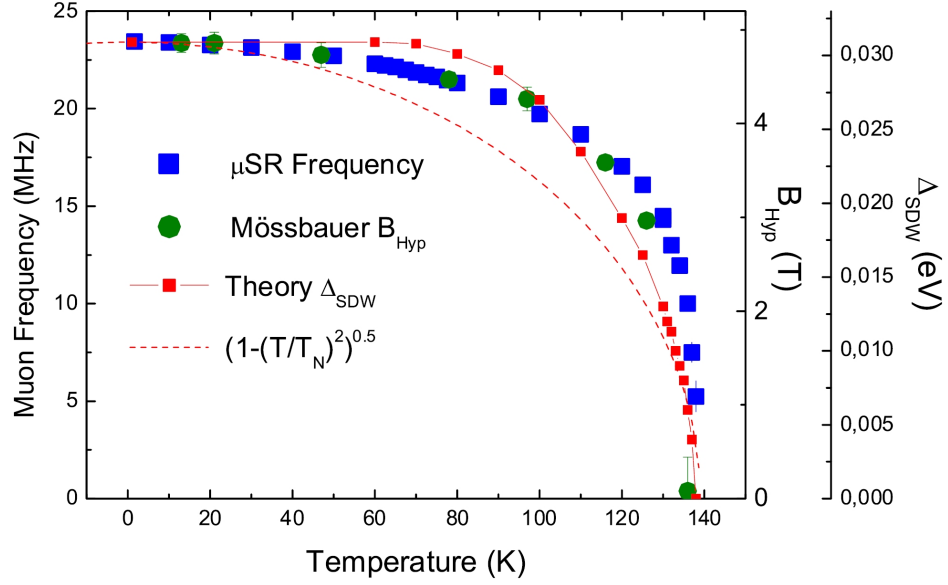
FIGURE 3.20:   Temperature dependence of the order parameter of LaO$_{1-x}$F$_x$FeAs, taken from Ref.[70]

coefficient λ:

$$H_{int} = \pm\lambda m_{Fe} \qquad (3.3)$$

Hereafter the sign depends on the type of interaction, being "+" for ferromagnetic and "−" for antiferromagnetic exchange. Neglecting the weak dipolar contribution, the magnetization normalized to the single ion m_{Gd} of the Gd subsystem is proportional to the sum of the applied magnetic field H_{ext} and internal field H_{int}:

$$m_{Gd} = \chi_{Gd}(T)\,(H_{ext} \pm H_{int}), \qquad (3.4)$$

where $\chi_{Gd}(T) = C_{Gd}/(T - \Theta)$ is the Gd magnetic susceptibility, C_{Gd} is the Gd Curie constant, Θ is the Gd Curie temperature. Due to the exchange interaction, the uncompensated magnetic moment m_{Fe} is proportional not only to the applied field but also to the internal field created by the Gd moments:

$$m_{Fe} = \alpha(H_{ext} + \lambda m_{Gd}) \qquad (3.5)$$

Here α is the susceptibility of the ordered Fe moments to the external magnetic field. Using Eq. 3.3, Eq. 3.4 and Eq. 3.5 one can obtain the equation for the

internal field H_{int} at the Gd site:

$$H_{int} = \pm \frac{\lambda^2 \alpha C_{Gd} + \lambda \alpha (T - \Theta)}{(T - \Theta) - \lambda^2 \alpha C_{Gd}} H_{ext} \qquad (3.6)$$

Eq. 3.6 enables to fit reasonably well the measured temperature dependence of the internal field (see Fig.3.17). The resonance field of the Gd is determined by the applied field and by the internal field $H_0 = H_{ext} \pm H_{int}$. At high temperatures when there is no internal field at the Gd site at any strength of the applied magnetic field ($H_{int} = 0$) one can measure the resonance field $H_0 = 11.7\,\mathrm{T}$ (for measurement frequency $\nu = 328\,\mathrm{GHz}$). Assuming that the resonance field of the Gd ions $H_0 = 11.7\,\mathrm{T}$ stays constant at all measured temperatures one obtains the expression for the applied field $H_{ext} = H_0 \mp H_{int}$ ($H_0 = 11.7\,\mathrm{T}$). The fit for two measurement configurations ($H_{res\perp}$ and $H_{res\parallel}$) is shown on Fig.3.17 by solid lines. The parameters C_{Gd}, Θ and α can be taken from different experiments. The Gd Curie constant C_{Gd} and Curie temperature Θ are known from the susceptibility data of GdOFeAs samples (see Sec. 3.4.1). As it is shown in Ref.[74] the bulk Fe susceptibility of LaOFeAs samples is determined by the spin susceptibility. Therefore the parameter α can be estimated from this measurement yielding a value of $\sim 10^{-4}\,\frac{\mathrm{erg}}{\mathrm{G^2\,mol}}$ [63, 74, 83, 84]. The λ value resulting from the fit is equal to ~ 19.7 $\frac{\mathrm{G^2\,mol}}{\mathrm{erg}}$ for $H_{res\perp}$ and $\sim 25.3\,\frac{\mathrm{G^2\,mol}}{\mathrm{erg}}$ for $H_{res\parallel}$. According to the mean field theory [6], these values yield an estimate of the exchange interaction energy J for two configurations amounting to $|J| \sim 15\,\mathrm{K}$ for $H_{res\perp}$ and $|J| \sim 19\,\mathrm{K}$ for $H_{res\parallel}$. In addition, Eq. 3.3 enables to calculate the uncompensated moment m_{Fe}. Its value grows with decreasing the temperature and increasing the Gd susceptibility until it reaches $\sim 0.03\mu_B$ at the lowest measured temperature which suggests that the Gd subsystem additionally tilts or polarizes the SDW.

To summarize this part, the ESR results on GdOFeAs samples show that the Gd subsystem is exchange-coupled to the magnetic FeAs planes. On approaching the AFM SDW transition from above, the growing correlations between the Fe moments yield a shift of the Gd ESR line. At lower temperature, depending on the angle between H_{ext} and the c-axis of the sample, the signal shifts to higher or to lower fields due to the uncompensated exchange field which is transferred to the Gd site from the Fe moments canted in an external magnetic field. Since the full width at the half maximum ΔH is proportional to the difference between resonance fields

$H_{res\perp} - H_{res\parallel}$, then the width of the ESR signal ΔH of the non-oriented powder sample can be taken as a measure of this exchange field (Fig.3.21,a).

3.4.5 GdO$_{1-x}$F$_x$FeAs ($x = 0.07$, 0.14)

The influence of the fluorine doping on the Gd ESR has been studied on two powder samples of GdO$_{1-x}$F$_x$FeAs with 7% and 14% of fluorine. On Fig.3.22,a,b the evolution of the respective Gd^{3+} ESR spectra is shown on a reduced field scale. Similarly to the undoped sample, at high temperature the ESR spectrum for both doped samples consists of a single Lorentzian-shaped line with $g = 2.005$. While lowering the temperature, the line remains almost unchanged until a characteristic temperature T_{if} is reached. This temperature corresponds to the onset of an additional inhomogeneous contribution to the width of the ESR signal ΔH. This inhomogeneous contribution is shown by the shaded area on Fig.3.21,b,c. The temperature T_{if} clearly depends on the fluorine doping level. In the case of the 7% F-doped sample a noticeable broadening of the line starts at $T_{if}(x = 0.07) \sim 125\,\text{K}$, whereas for the 14% doped sample it starts at a lower temperature $T_{if}(x = 0.14) \sim 100\,\text{K}$. For both doped samples there is a shift of the minimum of the absorption ($H_{res\perp}$) to lower magnetic fields below T_{if} (Fig.3.23). Qualitatively this shift is similar to that of the undoped sample (solid line on Fig.3.23), but it is less pronounced. In addition, the inhomogeneous broadening and the shift of $H_{res\perp}$ to lower magnetic fields exhibit a magnetic field dependence similar to that of the undoped GdOFeAs sample (Fig.3.24).

3.4.6 Superconducting GdO$_{1-x}$F$_x$FeAs, discussion

The remarkable similarities of the Gd ESR behavior between the fluorine-doped samples and the undoped one strongly suggest that, even in the superconducting samples where the phase transition to the AFM SDW state is not observed in the thermodynamics and transport properties, quasi static (on the time scale of the ESR measurement) magnetic correlations in the FeAs planes are present below the characteristic temperature T_{if}. Such correlations may explain the peculiar features in the resistivity data shown in Sec. 3.4.1.
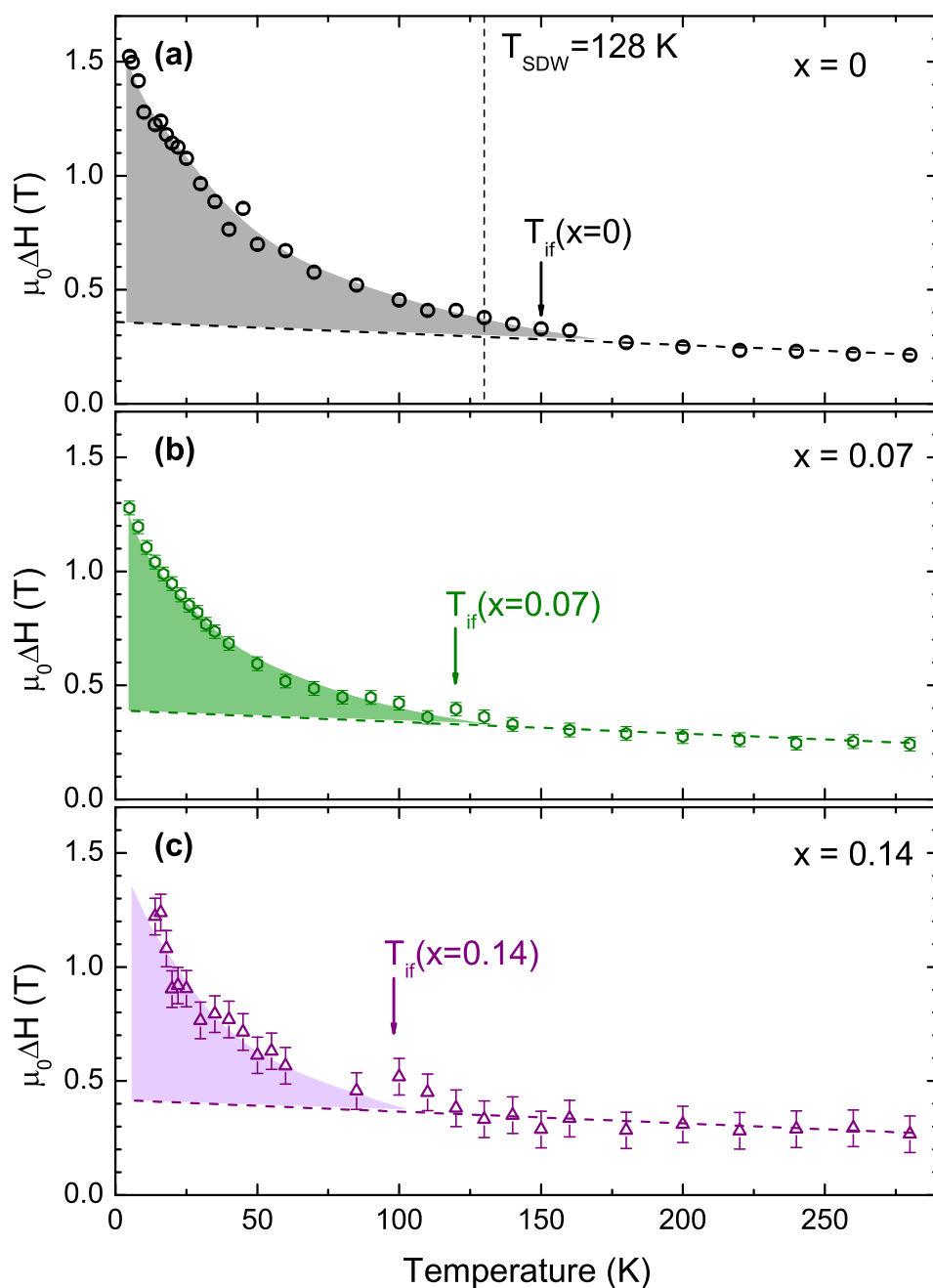
FIGURE 3.21: The full width at the half maximum (FWHM) ΔH of the ESR lines, measured at a frequency of $\nu = 348$ GHz ($x = 0.07$) and $\nu = 328$ GHz ($x = 0, 0.14$), as a function of temperature for the non-oriented GdO$_{1-x}$F$_x$FeAs samples; **(a)** $x = 0$; **(b)** $x = 0.07$; **(c)** $x = 0.14$.
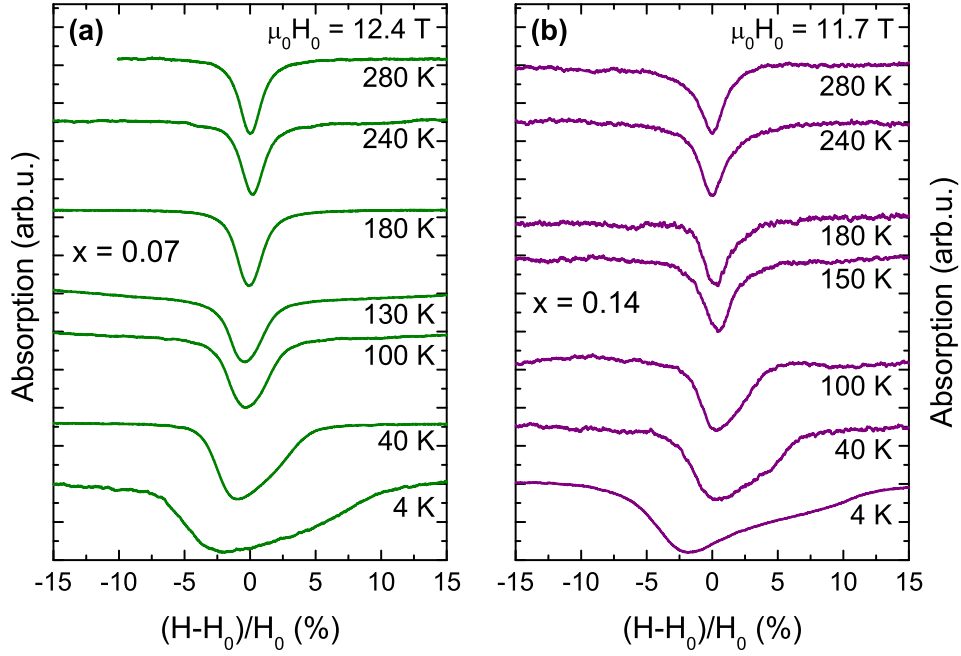
FIGURE 3.22: Temperature evolution of the high-frequency/field ESR spectra of GdO$_{1-x}$F$_x$FeAs powder samples measured at a frequency of $\nu = 348$ GHz ($x = 0.07$) and $\nu = 328$ GHz ($x = 0.14$), shown on a reduced field scale $(H - H_0)/H_0$. Here H_0 is the resonance field of the signal at high temperature; **(a)** $x = 0.07$, $\mu_0 H_0 = 12.4$ T; **(b)** $x = 0.14$, $\mu_0 H_0 = 11.7$ T.

The unified phase diagram for the iron pnictides, especially for the 1111 materials, is not fully established so far since the issue of coexistence of superconductivity and magnetism remains controversial. The nonmagnetic rare earth based LaO$_{1-x}$F$_x$FeAs material exhibits no evidence for the presence of a static magnetic order for any superconducting composition, but rather reveals SDW-like spin fluctuations seen in the transport [78] and inelastic neutron scattering experiments [85, 86]. On the other hand, the *magnetic* rare earth based systems (Ce, Sm, Nd) studied so far demonstrate coexistence of superconductivity and static magnetism at least in the underdoped region [55, 87]. Our high-field ESR results show that there is yet another 1111 system comprising a strongly magnetic rare earth (Gd) subsystem where the coexistence of quasi-static magnetism and superconductivity is still visible in large doping range. Here, the increase of the fluorine content and correspondingly the rise of T_c leads to the suppression of magnetic correlations indicating a possible interplay between these two states. All this suggests that the coexistence and possible interplay of the static or quasi-static magnetism and superconductivity may be a generic property of 1111-type compounds. In this regard, a remaining question yet to be answered is the extent to which the R-Fe
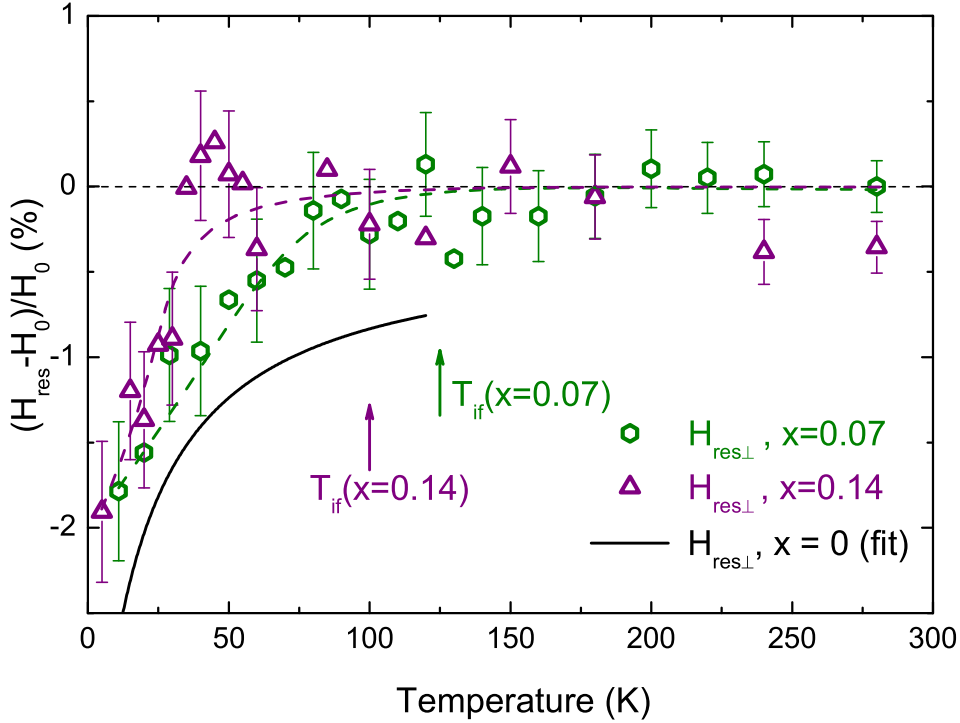
FIGURE 3.23: The shift of the minimum of absorption of the spectra with temperature, measured at a frequency $\nu = 348\,\text{GHz}(x = 0.07)/328\,\text{GHz}(x = 0.14)$, on a reduced field scale $(H_{res} - H_0)/H_0$. Here $\mu_0 H_0 = 12.4\,\text{T}/11.7\,\text{T}$ is the resonance field of the signal at high temperature, open hexagons - $x = 0.07$, open triangles - $x = 0.14$, solid line - fit of the resonance field in the parent GdOFeAs sample.

magnetic interaction influences the magnetic correlations in the FeAs planes.

3.4.7 GdO$_{1-x}$F$_x$FeAs summary

Our HF-ESR study of polycrystalline samples of the GdO$_{1-x}$F$_x$FeAs superconductor reveals a magnetic coupling between the Gd subsystem and the FeAs layers. This coupling, most probably of the anisotropic exchange type, is visible in the Gd ESR response in the undoped GdOFeAs in the SDW state, in form of a field-induced inhomogeneous broadening and shift of the ESR spectrum. This effect is caused by the interaction of the Gd spins with the uncompensated Fe moments due to the canting of the Fe moments in magnetic field. Furthermore, the data suggest that the Gd moments additionally tilt the ordered Fe moments. Surprisingly, the broadening and the shift of the spectrum are present also in the doped superconducting samples where there is no evidence of long range magnetic order. This points to the presence of short range, static on the ESR time scale, magnetic
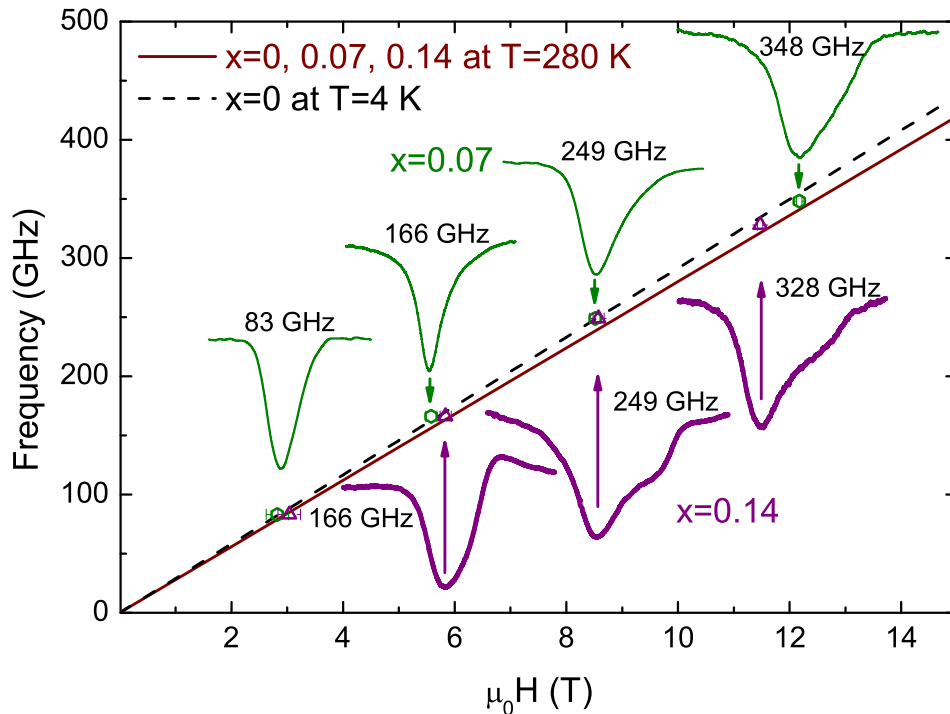
FIGURE 3.24: Frequency dependence of the ESR signal from $GdO_{1-x}F_xFeAs$ powder samples measured at a temperature of $T = 4\,K$, in SC state; data points correspond to the position of the minimum of absorption of the spectra at different frequencies, open hexagons - $x = 0.07$, open triangles - $x = 0.14$, dashed line - guide for the eyes, solid line - the frequency dependence of the position of the high-T Gd ESR line measured at $T = 280\,K$ for both F-doped samples; the lineshape of the spectra is shown as well, thin solid line - $x = 0.07$, thick solid line - $x = 0.14$.

correlations. This may be relevant to the interplay of magnetism and superconductivity in these materials, where on doping with fluorine there is a simultaneous increase of the superconducting critical temperature and suppression of the magnetic correlations. The possible relevance of the exchange interaction between the magnetic rare-earth subsystem and the FeAs planes to the properties of this novel class of superconductors remains to be elucidated.

3.5   Conclusion

The ESR investigation on the Gd- and La-based 1111-type FeAs superconductors evidences that there is an interaction between Gd- and Fe-layers. In fact one can separate different types of interactions taking place in this material. First of all there is a dipole-dipole interaction, whose effect is most pronounced in the

Gd diluted system and in small external magnetic fields. The second type of the interaction is the anisotropic exchange interaction, which appears to be most pronounced in the concentrated GdO$_{1-x}$F$_x$FeAs system. Besides its anisotropic nature, this interaction has an interesting feature, namely a frustration in the absence of an external magnetic field. To switch it on one has to tilt the SDW using magnetic field and thus to create an uncompensated Fe magnetic moment, which will interact with the Gd subsystem. At present the origin of this interaction can not be unambiguously verified. Likely it can be an exchange interaction between different Fe $3d$ bands and Gd $4f$ orbitals with some admixture of an RKKY type coupling.

The ESR measurements performed on the concentrated GdO$_{1-x}$F$_x$FeAs system suggest the coexistence of superconductivity and magnetism in the Fe-layer. The magnetism, found in the doped superconducting samples, is static on the ESR time scale and exhibit similar properties as in the undoped GdOFeAs sample. The quantitative analysis yields that the temperature, at which short range magnetic order is found, decreases with increasing the doping level, and as following with increasing T_c. This suggest that the magnetism of the Fe layers becomes more suppressed with doping, but, interestingly, it is still present up to the high doping levels. This finding enables to suggest the picture of the coexistence and the interplay between magnetism and superconductivity in Gd-based 1111 FeAs superconductors [88].

Chapter 4

Hole induced spin polarons in LaCoO$_3$

4.1 Introduction

The physical properties of nanostructured magnetic materials are extensively studied because of their fundamental interest and potential applications. A naturally-occurring analog to the artificially-fabricated heterostructures [89] and single molecular magnets [90] are doped perovskites with intrinsic inhomogeneities, i.e., with a spatial coexistence of magnetic clusters in a nonmagnetic matrix. A good example of such a material is LaCoO$_3$ doped with holes via the substitution of Sr with La. It has a pseudo-cubic structure (Fig.4.1) with a trigonal distortion along one of the cube diagonals, which makes this diagonal a symmetry axis [001] (see Fig.4.1) [91, 92]. The Sr^{2+} for La^{3+} substitution provides a charge hole to the system due to the difference in valency of these ions and creates a local crystal field distortion due to the difference in the ionic radii of Sr^{2+} and La^{3+} [91, 92].

The magnetic properties of La$_{1-x}$Sr$_x$CoO$_3$ are defined by the Co^{3+} and Co^{4+} spin states. Depending on the crystal field strength and symmetry (Fig.4.2) there are several possible spin states (see also Sec.1.8). In the case of Co^{3+} in a weak octahedral crystal field the 6 $3d$ electrons occupy both the e_g and the t_{2g} levels, yielding a high spin state with a spin value of $S = 2$ (Fig.4.2,b). The partial quenching of the orbital moment reduces it to $L = 1$ in this case. A strong crystal field can split the e_g and the t_{2g} levels so that the Hund's energy is not
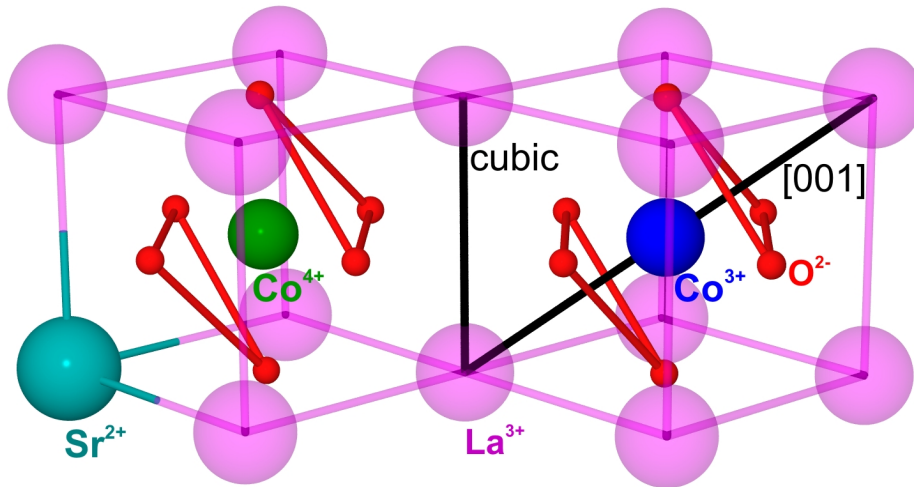
FIGURE 4.1: Pseudo-cubic structure of LaCoO$_3$. Oxygen ions form around each Co ion an octahedron with a small trigonal distortion . Cube diagonal [001] is the symmetry axis of the system.

big enough to overcome this gap (Fig.4.2,c). In this case all 6 electrons stay on the t_{2g} levels, yielding a low spin state with spin $S = 0$ and a fully quenched orbital moment $L = 0$. This state is thus nonmagnetic. The distortion of the octahedral symmetry of the crystal field leads to the splitting of the e_g and t_{2g} levels themselves (Fig.4.2,d). Here, depending on the strength of the distortion, it is possible to stabilize an intermediate spin state of the Co ion with a spin value of $S = 1$ and a fully quenched orbital moment $L = 0$. The case of Co^{4+} is very similar to Co^{3+} with the difference that there is one less electron in the $3d$ shell. This yields $S = \frac{5}{2}$ and $L = 0$ for the high spin state, $S = \frac{1}{2}$ and $L = 1$ for the low spin state and $S = \frac{3}{2}$ and $L = 1/2$ for the intermediate spin state.

Such a large number of different Co states and the possibility to transform one to another by changing dopant content and temperature yields a rich diversity of the electronic phases. Conceptional phase diagram has been predicted many years ago by J.B. Goodenough basing on electron diffraction, static magnetometery and transport measurements (see Fig.4.3) [91]. The later experimental works confirmed its validity and allowed to build slightly simplified phase diagram which is shown on Fig.4.4 [93]. First, the parent LaCoO$_3$ is nonmagnetic insulator at low temperatures. At elevated temperatures it becomes paramagnetic due to the thermal activation of the high spin state and it exhibits semiconducting properties. Second, it is widely believed that the addition of each hole into pristine LaCoO$_3$ through the substitution of a divalent, e.g., Sr^{2+}, ion for the La^{3+} ion creates a Co^{4+}
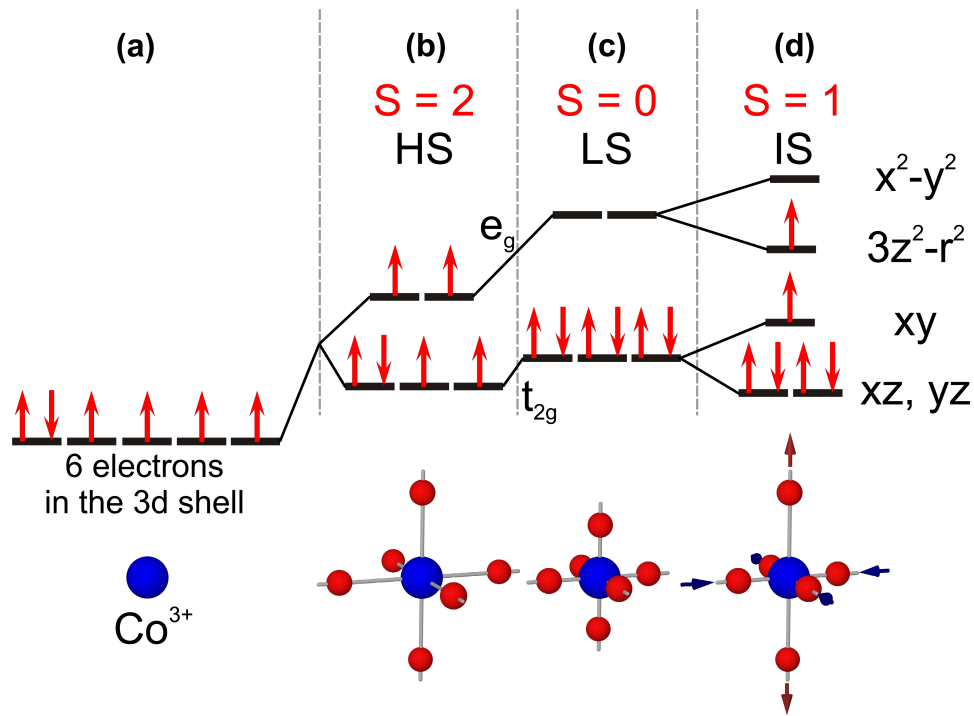
FIGURE 4.2: Spin states of the Co^{3+} ion depending on the crystal field strength and symmetry. **a)** Free Co^{3+} ion, $S = 2$, $L = 2$; **b)** weak crystal field with an octahedral symmetry, high spin state $S = 2$, partially quenched orbital moment $L = 1$; **c)** strong crystal field with an octahedral symmetry, low spin state $S = 0$, quenched orbital moment $L = 0$; **d)** crystal field with an tetragonally-distorted octahedral symmetry, intermediate spin state $S = 1$, quenched orbital moment $L = 0$.

ion in the lattice which has a nonzero S in any spin-state configuration, thereby inducing a magnetic moment in the system [91, 94]. At low temperatures Sr-doped $LaCoO_3$ shows a spin-glass and superparamagnetic behavior for $\sim 0.05 \leq x \leq \sim 0.2$ [91, 93–95] which is believed to be due to agglomeration of holes in clusters. With the addition of charge carriers, the number and possibly the size of the clusters grow, leading to a percolation-type long-range ferromagnetic (FM) order and metal-insulator (MI) transition [96] at x $\geq$ 0.18 [91, 93, 95].

Most of the investigations up to now have been focused on a relatively high Sr concentration ($x > 0.1$). An amazing fact was found by Yamaguchi et al. in 1996 [98] and apparently forgotten later. Namely, already lightly-doped material with $x = 0.002$ (i.e., with an estimated concentration of only two holes per thousand Co^{3+} ions) exhibits unusual paramagnetic properties at low temperatures: The few resulting spins, embedded in a nonmagnetic matrix, give magnetic susceptibility an order of magnitude larger than expected. It was proposed that a doped hole in
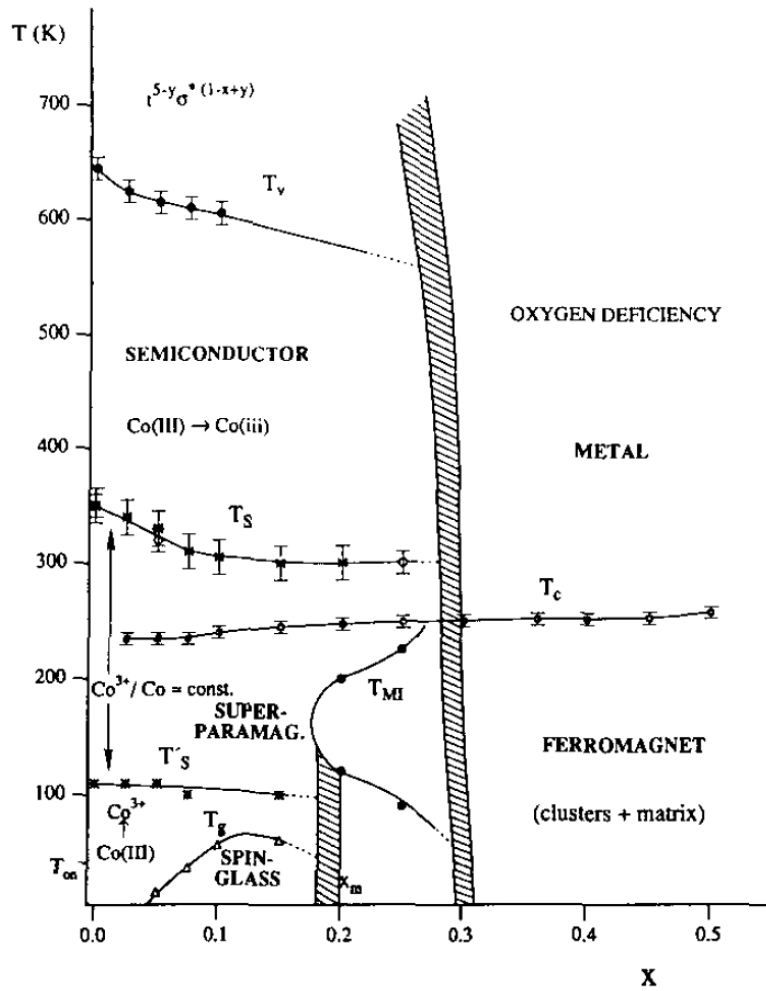
FIGURE 4.3: Phase diagram of La$_{1-x}$Sr$_x$CoO$_3$ ($0 \leq x \leq 0.50$) made by M. Señarís-Rodríguez and J. Goodenough, [91]

the spin-singlet ground state of LaCoO$_3$ behaves as a localized magnetic impurity with a unusually large spin value $S = 10 - 16$ [98] due to the formation of a magnetic polaron whose nature, however, remained unclear. Later, and for higher Sr doping $x > 0.05$, it was surmised that the addition of charge carriers causes the appearance of Zener-type polarons or even many-site magnetopolarons [94, 95]. However, experimental proof of the existence of such polarons is missing so far.

In this work we present the analysis and discussion of magnetization, ESR and NMR measurements performed on 0.2% Sr-, Y- and Ca- doped LaCoO$_3$. The goals of the research were to prove experimentally the formation of spin polarons, to understand the mechanism of this formation, and to establish the role of the hole and of the crystal field distortion introduced by the doping. Sr^{2+} has an ionic
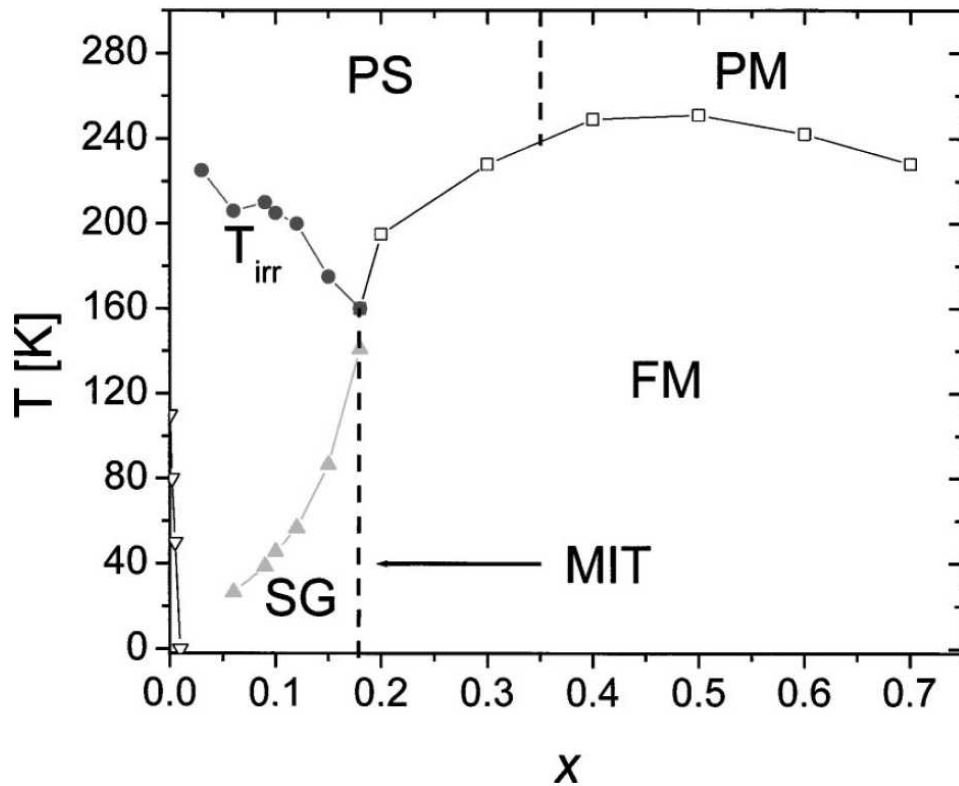
FIGURE 4.4: Magnetic phase diagram for $La_{1-x}Sr_xCoO_3$ [93]. PS - paramagnetic semiconductor, PM - paramagnetic metal, FM - ferromagnetic metal, SG - spin glass, MIT - metal-insulator transition, and T_{irr} is the irreversibility temperature which marks the bifurcation of the ZFC and FC dc magnetization curves. The open triangles at very low x indicate the estimated spin-state transition temperature from Yamaguchi et al. [97]

radius of $\sim 1.44\,\text{Å}$ which is significantly higher than the radius $\sim 1.36\,\text{Å}$ of La^{3+}. Therefore the Sr for La substitution yields a large local distortion. In order to probe the hole-doped system without the crystal field distortion we have chosen Ca^{2+} as the dopant, since its ionic radius is $\sim 1.34\,\text{Å}$. The Y^{3+} ion does not provide a hole to the system but creates a crystal field distortion due to its smaller ionic radius of $\sim 1.08\,\text{Å}$ which makes the Y-doped sample a good system to study pure crystal field distortion effects.

The experimental data evidence that the hole introduced by the substitution of only 0.2% of Sr^{2+} or Ca^{2+} for La^{3+} changes the spin state of 7 neighboring Co ions. The latter are then coupled ferromagnetically, leading to the formation at low temperature of spin polarons with a high magnetic moment and a sizeable orbital contribution. The Y^{3+}-doped $LaCoO_3$ sample exhibits weaker magnetism, not of polaronic origin. Therefore the carried out studies strongly suggest that

the introduced hole plays the main role in the formation of magnetic polarons, whereas the crystal field distortion plays a minor role.

4.2   Experimental details

Highly stoichiometric powder samples (La$_{0.998}$Ca$_{0.002}$CoO$_3$and La$_{0.998}$Y$_{0.002}$CoO$_3$) and a single crystal sample (La$_{0.998}$Sr$_{0.002}$CoO$_3$) were synthesized and characterized by *Dr. E. Pomjakushina* according to procedures described elsewhere [6]. The static magnetization measurements on these samples were done with a conventional Quantum Design VSM SQUID magnetometer. High-field/high-frequency ESR (HF-ESR) measurements were performed with a home-made spectrometer (see Chapter 2 and Ref.[52]) at frequencies $\nu = 27 - 550\,\text{GHz}$ and magnetic fields $B\mu_0 H = 0 - 15\,\text{T}$. Calculations of the spin energy levels and simulations of the frequency dependence of the ESR spectra were done with the EasySpin software package [99, 100], which is an open-access toolbox for MATLAB. The ^{59}Co and the ^{139}La NMR were measured at frequencies of 47.65 MHz and 94 MHz respectively with a Tecmag pulse NMR spectrometer.

4.3   Static magnetization measurements

The static magnetometry data (Fig.4.6) for Ca- and Sr-doped samples is very similar to the one measured by Yamaguchi et al. [98]. In contrast to the parent LaCoO$_3$ sample, the temperature dependence of the magnetic susceptibility of 0.2% Ca- and Sr-doped samples (Fig.4.5) shows anomalously strong upturn at temperatures below $\sim 30\,\text{K}$. On the contrary, the 0.2% Y-doped LaCoO$_3$ sample behaves similarly to the parent compound, with a susceptibility only slightly higher. When increasing the temperature above $\sim 30\,\text{K}$, the susceptibility increases in all four samples in a similar manner. The reason for this is the temperature activation of the high-spin state of all Co^{3+} ions leading to the change of the effective cobalt spin from S=0 to S=2 [98, 101–107]. Indeed, a temperature increase can lead to the change of the lattice parameters and of the vibration of the lattice which, in turn, leads to the change of the energy gap between e_g and t_{2g} levels of Co^{3+} ion (see Fig.4.2) so that the Hund energy wins crystal field energy and two electrons populate e_g level. At the temperature of $\sim 100\,\text{K}$ the susceptibility reaches its
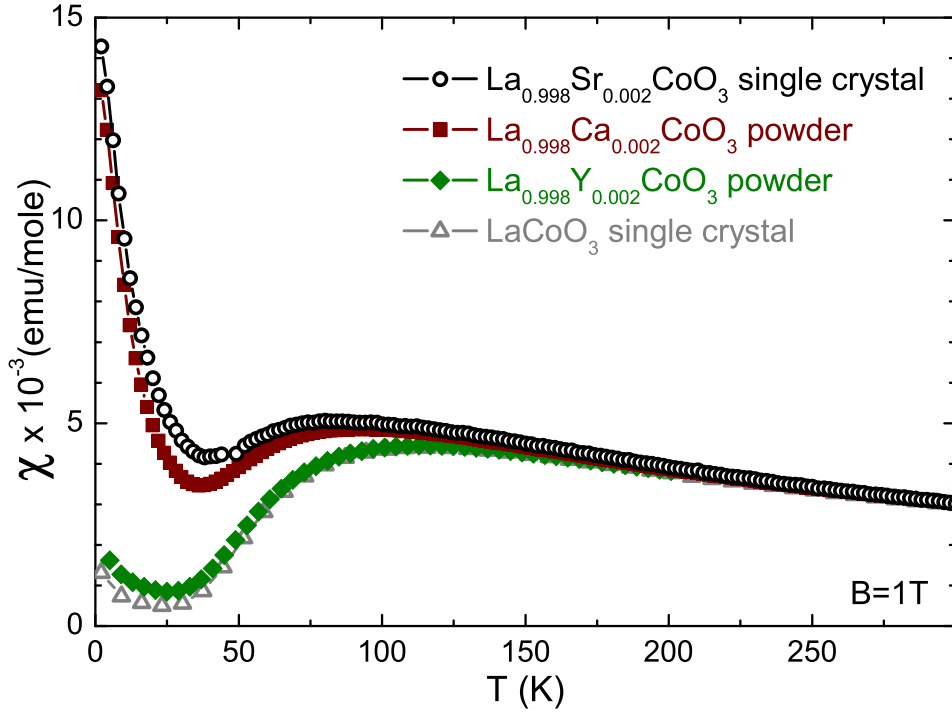
FIGURE 4.5: Temperature dependence of the static magnetic susceptibility of La$_{0.998}$Sr$_{0.002}$CoO$_3$ single crystal sample (open circles), La$_{0.998}$Ca$_{0.002}$CoO$_3$ powder sample (squares), La$_{0.998}$Y$_{0.002}$CoO$_3$ powder sample (diamonds), LaCoO$_3$ single crystal sample (open triangles).

maximum and decreases with further temperature increase. This characteristic temperature is the temperature where the spin state of the most of Co ions have transformed to a high spin state.

In order to estimate the effective magnetic moment in doped samples exhibiting the anomalous susceptibility at low temperature, we fitted the magnetization measured as a function of magnetic field (Fig.4.6) with the conventional Brillouin function $B_s(y)$ [6] and a field-linear term (4.1).

$$M(H) = N\mu_B gSB_s(y) + \chi_0 H, \quad y = \frac{g\mu_B SH}{k_B T} \qquad (4.1)$$

Assuming the doping concentration $N = 0.002$ we obtain the moment $gS \sim 15\mu_B$/hole for the Sr-doped sample. The Ca-doped sample exhibits a value which is slightly smaller, $gS \sim 13.5\mu_B$/hole, but still this value is much larger than what we can expect from Co^{3+} and Co^{4+} in any spin state. For instance, high-spin Co^{4+} which has the largest spin $S = 5/2$, will have a magnetic moment $gS = 5\mu_B$, assuming $g = 2$.
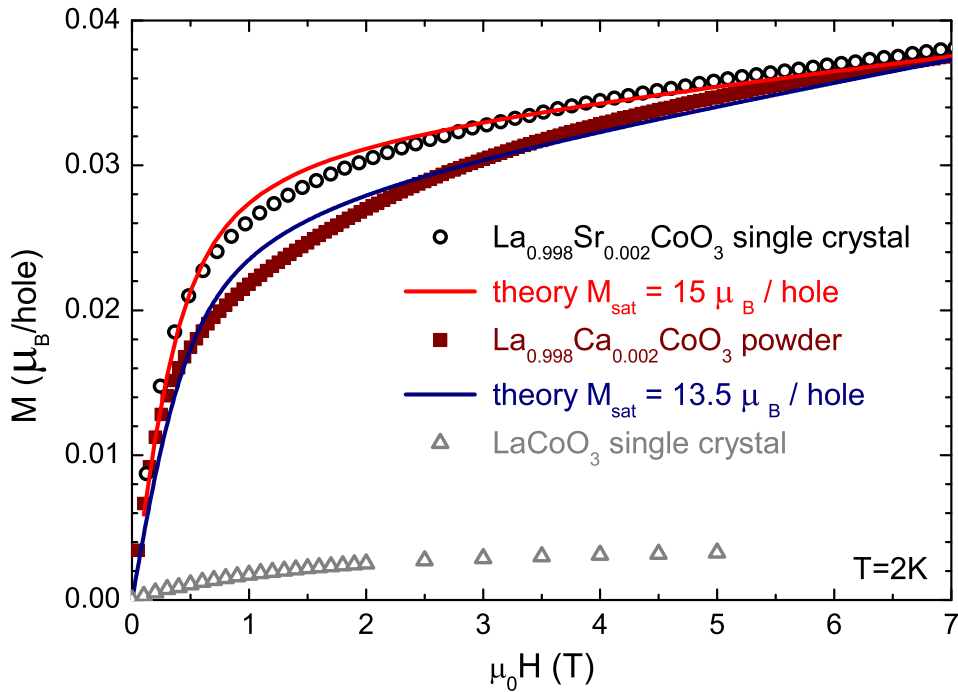
FIGURE 4.6: Magnetic field dependence of the static magnetization of La$_{0.998}$Sr$_{0.002}$CoO$_3$ single crystal sample (open circles), La$_{0.998}$Ca$_{0.002}$CoO$_3$ powder sample (squares), LaCoO$_3$ single crystal sample (open triangles). Solid lines depict Brillouin function fits yielding magnetic moment values of $gS \sim$ 15μ_B/hole for the Sr-doped sample and of $gS \sim$ 13.5μ_B/hole for the Ca-doped sample.

To summarize, static magnetometry data evidences that the Y doped sample exhibits the low-T behavior similar to the undoped LaCoO$_3$. In contrast, Sr- and Ca-doped samples exhibit similar strong magnetic response at low-T, but the magnetic moment in Ca-doped sample is slightly reduced.

4.4   Nuclear magnetic resonance

The NMR data presented in this chapter were obtained and analyzed by Dr. E. Vavilova. We started our NMR experiments on the undoped and Sr-doped LaCoO$_3$ samples, using ^{59}Co nuclei as probes of the local properties. The external magnetic field H was applied along the pseudo-cubic axis. The data are summarized in Fig.4.7. The spectral shape and the spin-lattice relaxation rate of the undoped LaCoO$_3$ agree very well with previous ^{59}Co NMR studies [108, 109]. According to a simple estimate, doping with 0.2% Sr, which yields 0.2% of Co^{4+} sites, should change the electric field gradient for at most 5% of nuclei. This would only slightly
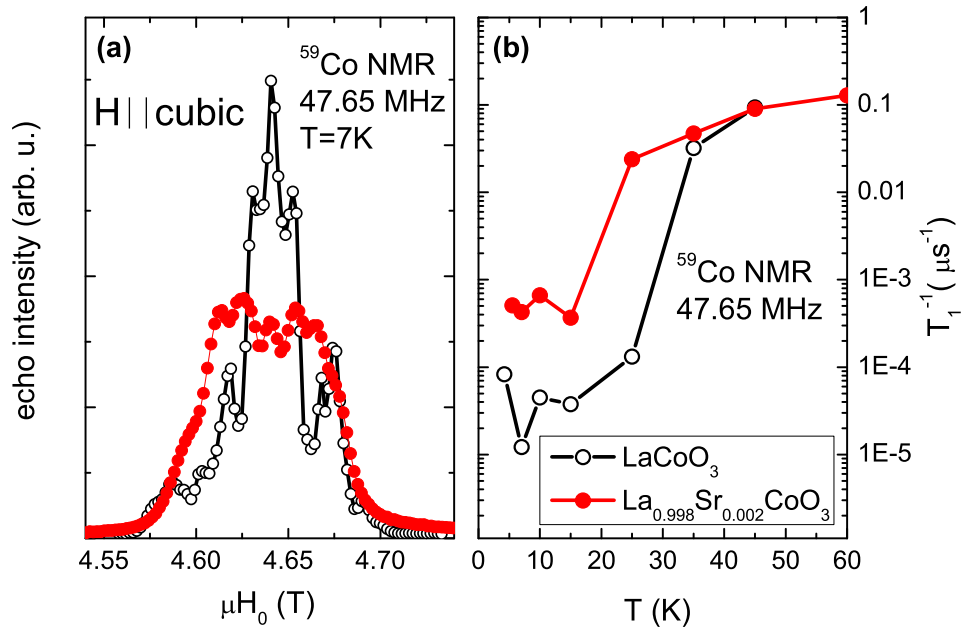
FIGURE 4.7: ^{59}Co NMR data of La$_{0.998}$Sr$_{0.002}$CoO$_3$ (closed circles) and LaCoO$_3$ (open circles) single crystals. **a)** Low-T spectra; **b)** temperature dependence of the nuclear spin-lattice relaxation rate T_1^{-1}.

affect the low-T ^{59}Co NMR spectra, the very well resolved quadrupole structure seen in the undoped sample would stay unchanged after doping. In contrast, the observed significant changes (Fig.4.7,a), namely strong broadening and poor resolution of the quadrupole structure suggest that the doping-induced change of the low-T spectrum is not due to the quadrupole interaction and has probably a magnetic origin. It becomes even more apparent in the nuclear spin dynamics yielding at low-T a more than one order of magnitude enhanced relaxation rate T_1^{-1} (Fig.4.7,b). The observed stretched-exponential shape of the nuclear magnetization recovery curve suggests a substantially nonuniform distribution of local magnetic environments at low-T as seen by the Co nuclei [110]. Thus the ^{59}Co NMR data for La$_{0.998}$Sr$_{0.002}$CoO$_3$ clearly indicate the formation of regions with large magnetization and which are non-uniformly distributed in the sample at low-T. In contrast, above ~ 35 K, where a considerable fraction of Co ions is in the thermally-activated HS state, the NMR spectra and relaxation for the doped and undoped samples are very similar, and the shape of the nuclear magnetization recovery testifies to an almost homogeneous distribution of magnetic centers.

The temperature dependence of the ^{59}Co spin-lattice relaxation rate T_1^{-1} in the Ca- and Y-doped LaCoO$_3$ samples is shown on Fig.4.8,b together with data for Sr-doped and undoped samples for a comparison purpose. The Ca-doped sample,
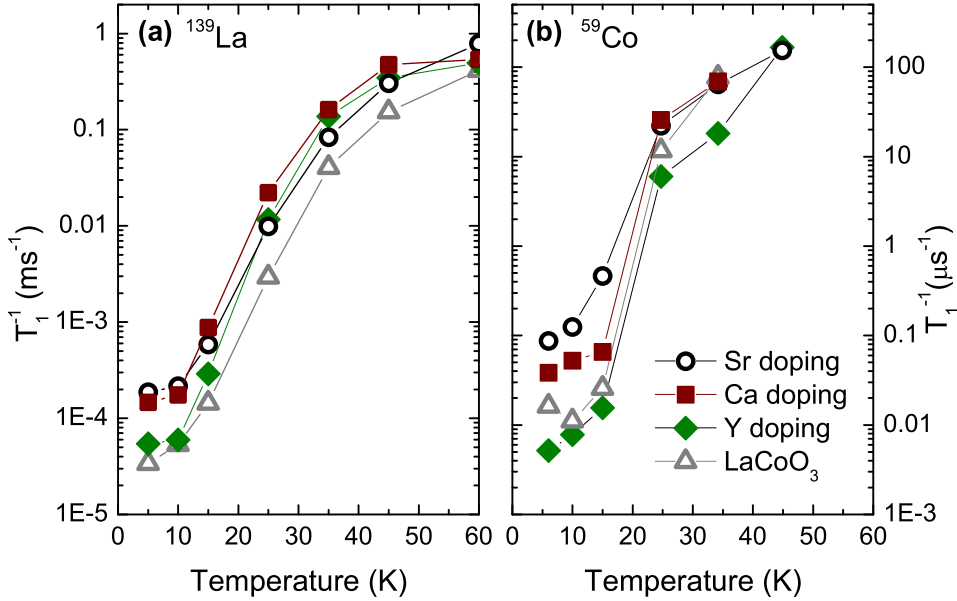
FIGURE 4.8: Temperature dependence of the nuclear relaxation rate T_1^{-1} of La$_{0.998}$Sr$_{0.002}$CoO$_3$ single crystal sample (open circles), La$_{0.998}$Ca$_{0.002}$CoO$_3$ powder sample (squares), La$_{0.998}$Y$_{0.002}$CoO$_3$ powder sample (diamonds), LaCoO$_3$ single crystal sample (open triangles). **a)** ^{139}La NMR data; **b)** ^{59}Co NMR data.

similar to Sr-, exhibit a significantly faster, about ~ 5 times, relaxation rate, whereas the Y doped sample shows almost the same relaxation rate as the undoped LaCoO$_3$. The low-T ^{139}La relaxation rate measurements exhibit even more drastic differences between Ca-doped and Y-doped samples (Fig.4.8,a). As can be seen, the Y-doped sample behaves similarly to the undoped sample, meaning that there is no magnetism at low-T in this sample. In contrast, the La$_{0.998}$Ca$_{0.002}$CoO$_3$ sample at low-T shows a behavior similar to that of the Sr-doped sample, but with slightly reduced relaxation rates. This indicates that Ca doping leads to the formation of inhomogeneous regions with large magnetization, as well as in the Sr-doping case.

4.5 Electron spin resonance

4.5.1 La$_{0.998}$Sr$_{0.002}$CoO$_3$, single crystal

Previous ESR studies on the undoped LaCoO$_3$ showed that this compound exhibits no ESR signal at $T \leq 30\,\text{K}$ due to the singlet ground state [105]. On Fig.4.9 the temperature dependence of the ESR response of La$_{0.998}$Sr$_{0.002}$CoO$_3$ measured
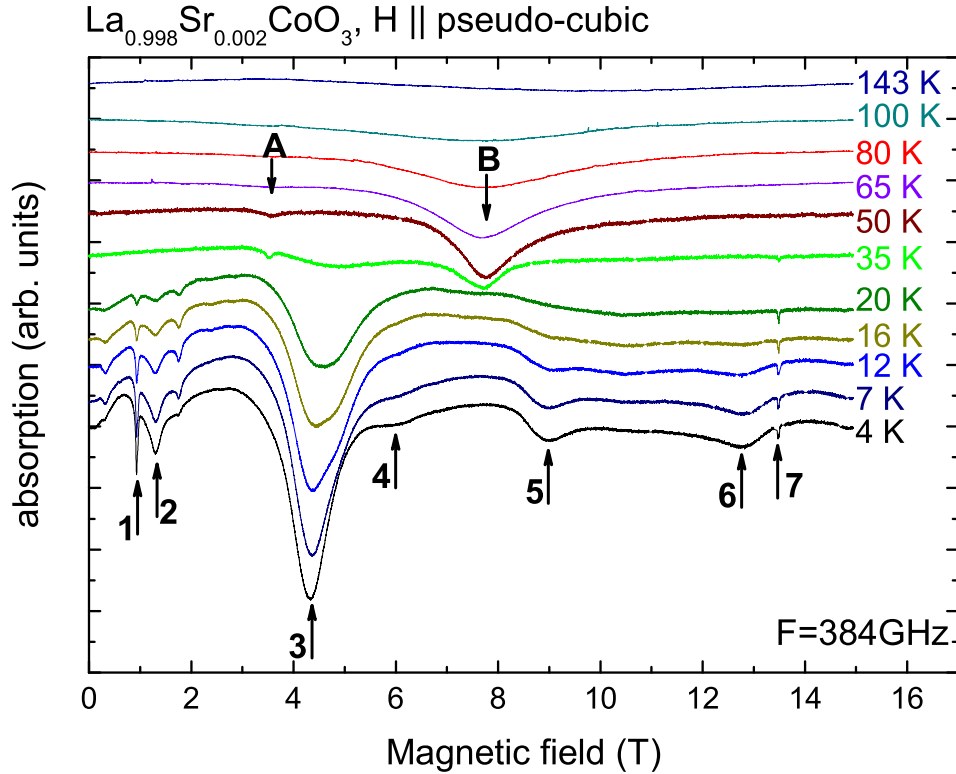
FIGURE 4.9: Temperature dependence of the high-field ESR spectra of the La$_{0.998}$Sr$_{0.002}$CoO$_3$ single crystal sample, measured in the configuration where the external magnetic field H is applied along the pseudo-cubic axis.

at $f = 384\,\mathrm{GHz}$ is shown for the measurement configuration where the external magnetic filed is parallel to the pseudo-cubic axis of the crystal (Fig.4.11, bottom). In contrast to LaCoO$_3$, La$_{0.998}$Sr$_{0.002}$CoO$_3$ shows a strong signal at the lowest temperature of $T = 4\,\mathrm{K}$, with a spectrum consisting of many well defined absorption lines (1,2,3,4,5...). When increasing the temperature, the intensity of these absorption peaks decreases until $T \sim 35\,\mathrm{K}$ where all these lines almost disappear. At the same temperature two new lines (A,B) arise.

Let us first discuss the high-T regime ($T > 35\,\mathrm{K}$). The frequency dependence of the A,B lines measured at $T = 50\,\mathrm{K}$ (Fig.4.10) was found to have one to one similarity to the frequency dependence measured by Noguchi on the parent LaCoO$_3$ compound [105] (see inset in Fig.4.10). The fit of the resonance branches A and B (solid lines on the Fig.4.10) was made in the same way as it was proposed in Ref.[105]. Due to the symmetry of the LaCoO$_3$ [101, 105] which is pseudocubic with a trigonal distortion along the cube's diagonal it is possible in the first approximation to describe the system using the simple effective spin Hamiltonian of

a uniaxial symmetry (see Sec.1.11 and [105]):

$$\mathcal{H} = g\mu_B \mathbf{H} \cdot \mathbf{S} + \frac{D}{3}\{3S_z^2 - S(S+1)\} \tag{4.2}$$

By choosing the magnetic field as a quantization axis, Eq.4.2 can be transformed to the form of:

$$\mathcal{H} = g\mu_B \mathrm{H} S_z + \frac{D}{3}\{\frac{1}{2}(3\cos^2\theta - 1)O_2^0(S) - 3\sin 2\theta O_2^1(S) + \frac{3}{2}\sin^2\theta O_2^2(S)\} \tag{4.3}$$

with Stevens operators (see Sec.1.11)

$$O_2^0(S) = 3S_z^2 - S(S+1)$$
$$O_2^1(S) = \frac{1}{2}(S_z S_+ + S_+ S_z)$$
$$O_2^2(S) = \frac{1}{2}(S_+^2 + S_-^2),$$

and θ being the angle between the magnetic field and the symmetry axis [001], pseudo-cube diagonal in this case. In the present measurement configuration the angle θ is equal to 55°. Diagonalization of the matrix of this Hamiltonian gives the magnetic field dependence of the energy levels of the system which enables to calculate ESR resonance fields at a given frequency. By changing the Hamiltonian parameters one can fit experimental points with calculated resonance branches. The best fit gives a g-factor and a single-ion anisotropy parameter D identical to those in the reference [105], $g = 3.48$ and $D = 147\,\mathrm{GHz}$ (4.9 cm^{-1}). This finding suggests that at high temperatures the magnetism of Sr-doped LaCoO$_3$ has the same nature as that in the undoped sample, namely it is due to the temperature-activated Co^{3+} high-spin state.

To understand the nature of the low-temperature ESR response we measured the frequency dependence at $T = 4\,\mathrm{K}$ in two different experimental configurations, magnetic field applied parallel to the pseudo-cubic axis (Fig.4.11) and magnetic field having an angle of 110° with the [001] crystallographic direction (cube's diagonal) (Fig.4.12). We have chosen the 3 most intensive transitions present at all measurement frequencies (1,2 and 3 on Fig.4.9) and tried to simulate their frequency dependence. Due to the same symmetry reason as in the case of the LaCoO$_3$ [101, 105] (see above), we took the effective spin Hamiltonian described by Eq.4.3 and performed the numerical diagonalization of its matrix for different spin
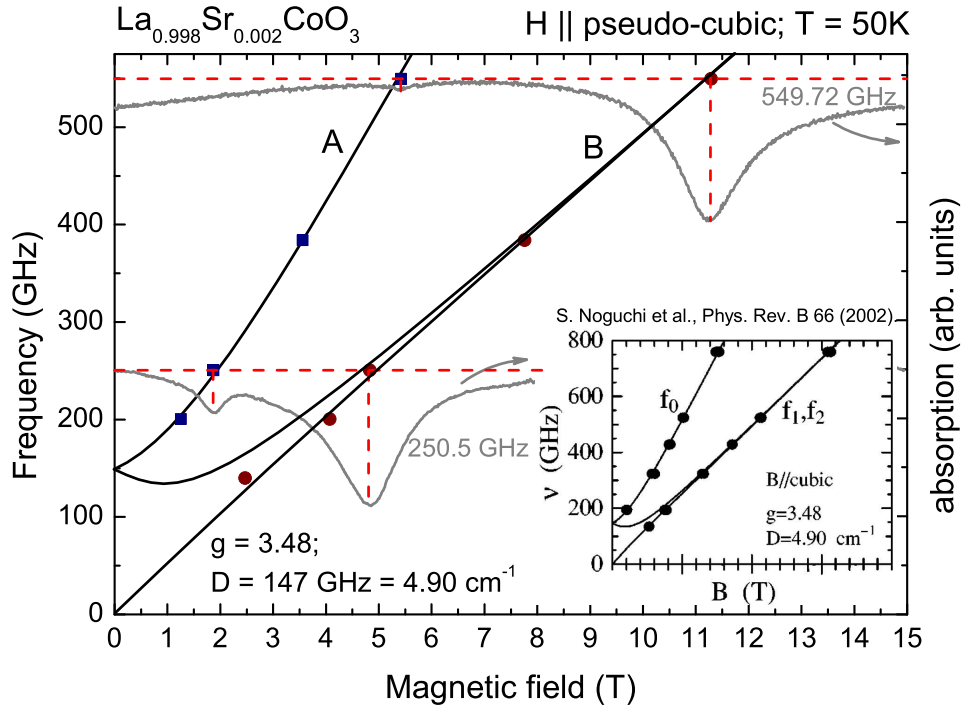
FIGURE 4.10: Frequency dependence of the ESR spectra of the La$_{0.998}$Sr$_{0.002}$CoO$_3$ single crystal sample measured at $T = 50$ K and with the magnetic field applied along the pseudo-cubic axis. Inset represents the frequency dependence of undoped LaCoO$_3$ measured in the same configuration by Noguchi et al. [105]

values S. In addition, we varied its parameters (g-factor and crystal field anisotropy D) in order to better fit the frequency dependence of the chosen transitions.

The angle θ in the Hamiltonian is the angle between the symmetry axis [001] and the magnetic field direction, its value we take from the experiment. For the experimental configuration where the magnetic field is parallel to the pseudo-cubic axis (Fig.4.11) the angle θ is equal to 55°. The magnetization measurements provide the saturation magnetic moment value of $gS = 15\mu_B$/hole which gives the limit for the spin and g-factor value. The best fit, which is shown on the Fig.4.11 as solid lines, was obtained for $S = 13/2$, $g = 2.6$ and $D = 101$ GHz. These values give a magnetic moment of $16.9\mu_B$/hole at saturation which is only slightly larger than obtained from the magnetization measurements. According to the fit the three absorption lines 1, 2 and 3 are transitions between the spin energy levels $-\frac{1}{2} \leftrightarrow +\frac{3}{2}$, $-\frac{1}{2} \leftrightarrow -\frac{3}{2}$, and $-\frac{1}{2} \leftrightarrow +\frac{1}{2}$ respectively (inset on Fig.4.11).

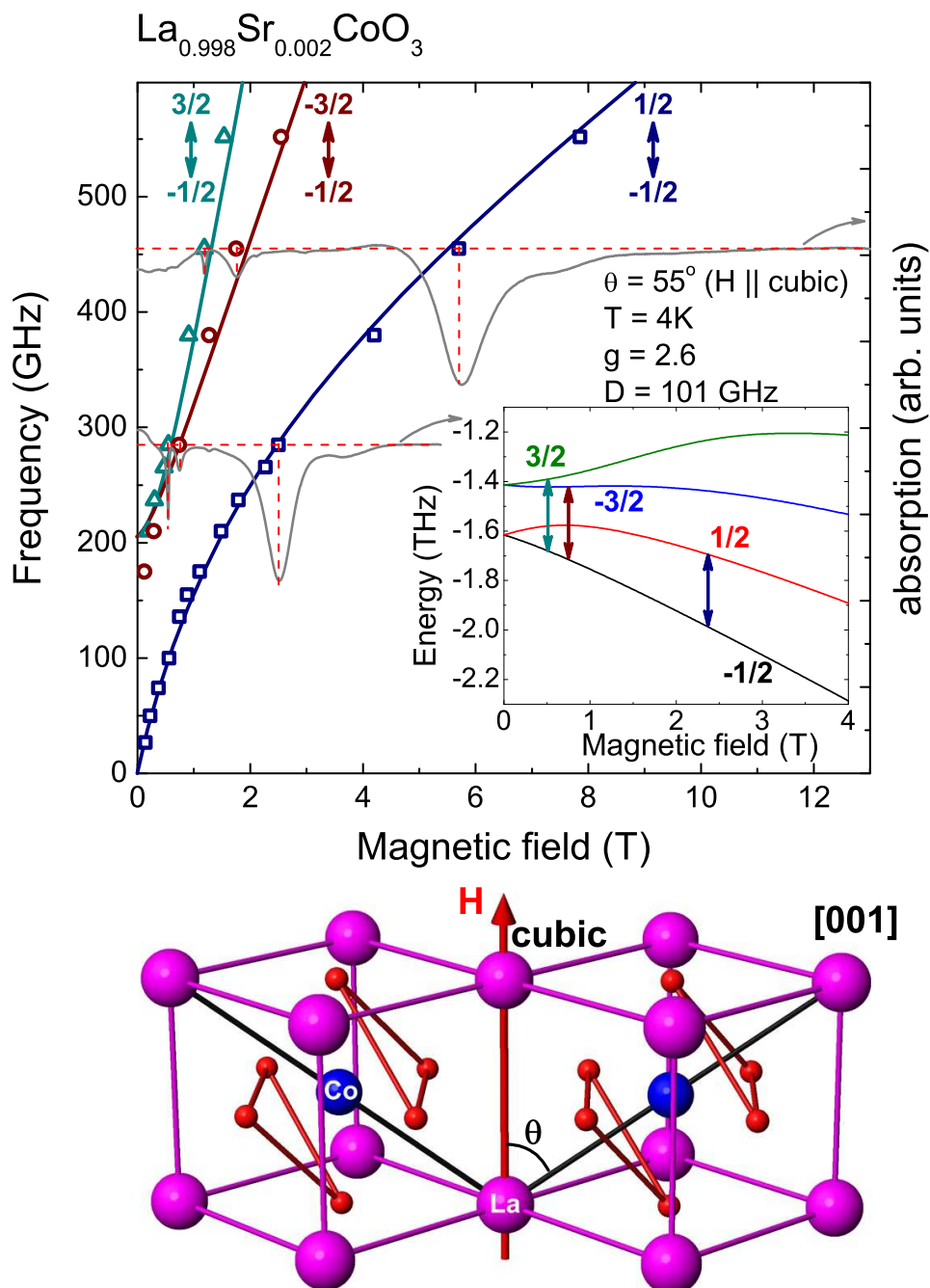For the experimental configuration with $\theta = 110^o$ we made the same simulation

FIGURE 4.11: Frequency dependence of the low-T ESR response of the La$_{0.998}$Sr$_{0.002}$CoO$_3$ single crystal sample measured at $T = 4$ K with the angle $\theta = 55^o$ between the magnetic field H and the symmetry axis [001] (H is parallel to the pseudo-cubic axis, see bottom of the figure). The solid lines represent the theoretical simulation of the frequency dependence of the resonance fields. The corresponding energy level diagram is shown in the inset.
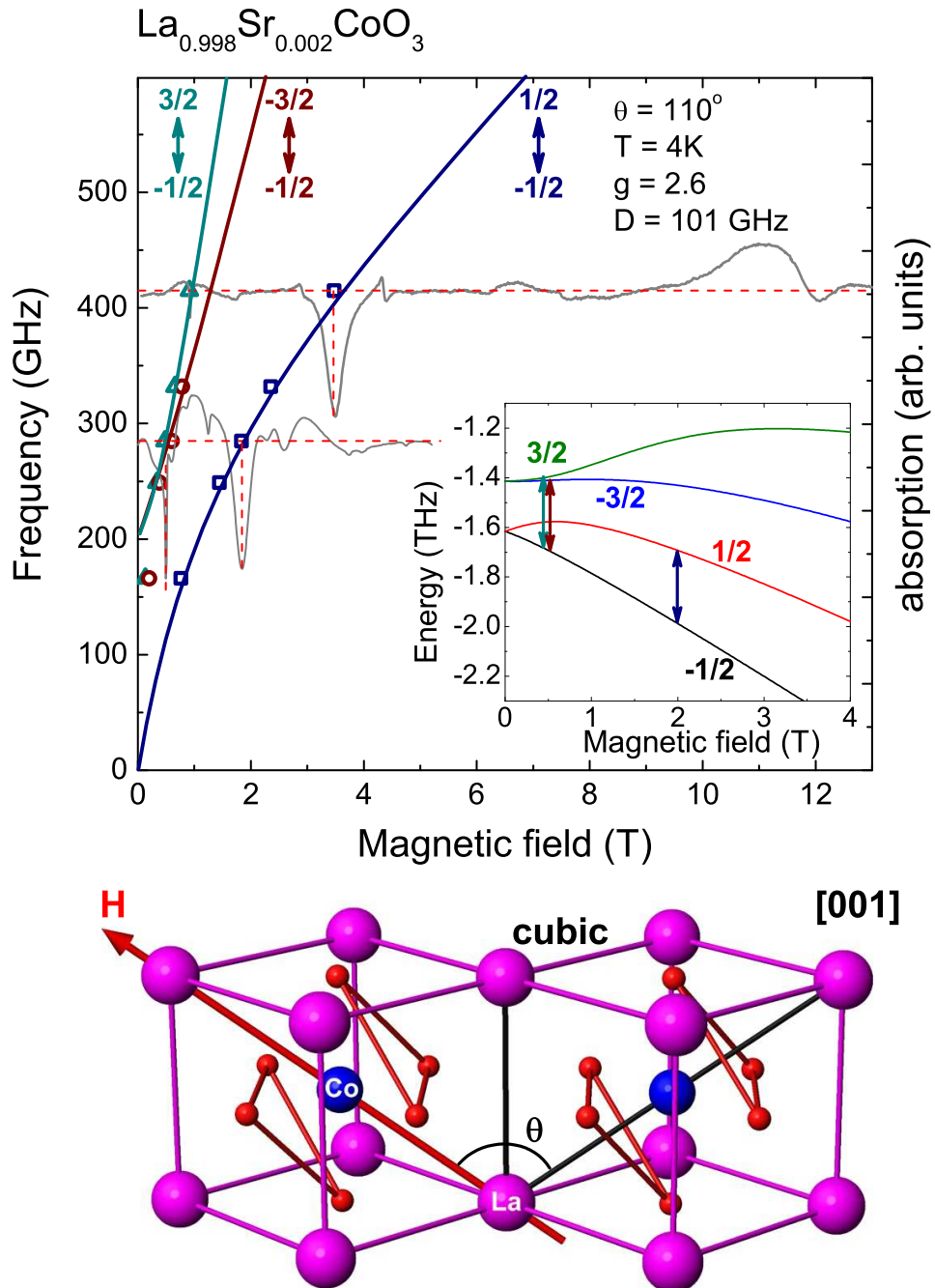
FIGURE 4.12: Frequency dependence of the low-T ESR response of the La$_{0.998}$Sr$_{0.002}$CoO$_3$ single crystal sample measured at $T = 4$ K with the angle $\theta = 110^o$ between the magnetic field H and the symmetry axis [001], see bottom of the figure. The solid lines represent the theoretical simulation of the frequency dependence of the resonance fields. The corresponding energy level diagram is shown in the inset.

procedure keeping all the parameters constant except θ itself. The resulting theoretical resonance branches of the same 1,2 and 3 transitions (solid lines on Fig.4.12) fit the experimental points as well as in the case of H‖cubic axis. The main absorption line of the spectra for both field directions, i.e., the one with the largest intensity (line 3), is the allowed transition between $\pm\frac{1}{2}$ states. This transition is gapless due to Kramers's theorem [9, 10, 29]. The two other transitions 1 and 2 are so called "forbidden" transitions having a gap of $\sim 200\,\text{GHz}$ which is $0.8\,\text{meV}$. The ESR selection rule allows only transitions with $\Delta S_z = \pm 1$, but transitions 1 and 2 seem to disobey this rule. In fact in the complex systems any kind of interaction or anisotropy would lead to a mixing of the states so that:

$$
\begin{aligned}
|-\frac{1}{2}> &= \alpha_1|-\frac{1}{2}> + \beta_1|+\frac{1}{2}> + \gamma_1|-\frac{3}{2}> + \delta_1|+\frac{3}{2}> \ldots \\
|+\frac{1}{2}> &= \alpha_2|-\frac{1}{2}> + \beta_2|+\frac{1}{2}> + \gamma_2|-\frac{3}{2}> + \delta_2|+\frac{3}{2}> \ldots \\
|-\frac{3}{2}> &= \alpha_3|-\frac{1}{2}> + \beta_3|+\frac{1}{2}> + \gamma_3|-\frac{3}{2}> + \delta_3|+\frac{3}{2}> \ldots \\
|+\frac{3}{2}> &= \alpha_4|-\frac{1}{2}> + \beta_4|+\frac{1}{2}> + \gamma_4|-\frac{3}{2}> + \delta_4|+\frac{3}{2}> \ldots
\end{aligned}
$$

$$\text{and so on...} \qquad (4.4)$$

with α_i, β_i, α_i, γ_i being weight coefficients defining the degree of mixing. When states are mixed then there is always a finite probability to have a transition between any states without breaking the selection rule. This leads the appearance of so called "forbidden" transitions.

In addition we measured the frequency dependence of the powder La$_{0.998}$Sr$_{0.002}$CoO$_3$ sample. Here, on the ESR spectra one sees mainly one pronounced ESR line (Fig.4.13) present at all measured frequencies. This line is essentially the result of the powder averaging of the most intensive absorption due to the allowed transition $-\frac{1}{2} \leftrightarrow +\frac{1}{2}$. The measurement frequency as a function of the resonance field of this line is shown on Fig.4.15 (open squares). Using the above model, keeping all the parameters unchanged, we were able to fit this powder frequency dependence as well. The fit, shown as a dotted line on the same figure, exhibits very good agreement with the measured points, which additionally proves the consistency of the model.

Thus, the ESR measurement performed on the La$_{0.998}$Sr$_{0.002}$CoO$_3$ single crystal strongly suggest an existence of a magnetic object with huge spin value of 13/2,
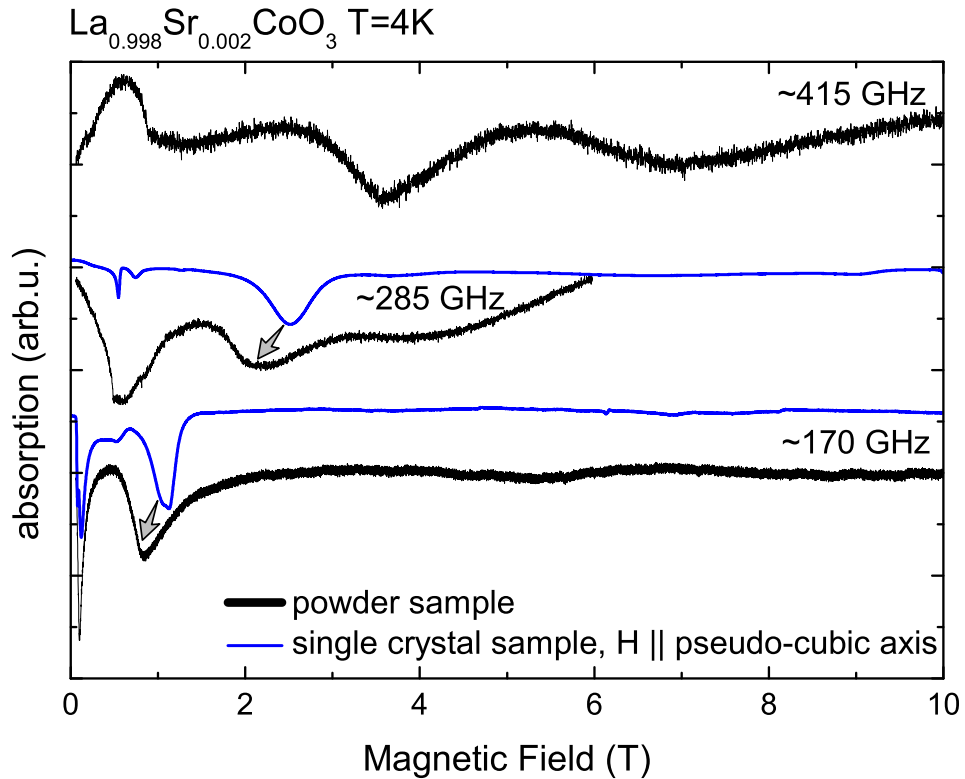
FIGURE 4.13:   Frequency dependence of the ESR signal from powder
$La_{0.998}Sr_{0.002}CoO_3$ at $T = 4\,K$.

which, in turn points to the formation of extended magnetic cluster at low temperatures. The g-factor of 2.6 indicates noticeable admixture of orbital magnetism. Besides the three absorptions taken into account for the above calculations there are less intensive resonance absorptions at higher magnetic fields which are not included in the simulation. Due to the fact that they appear at high magnetic field they might result from forbidden transitions between excited spin states of the magnetic cluster.

Connection to the inelastic neutron scattering data

The inelastic neutron scattering data (*measured by Dr. A. Podlesnyak* and published in Ref.[111]) are also perfectly explained using the calculated energy levels of a spin cluster with $S = 13/2$. On Fig.4.14 the magnetic field dependence of the INS energy transfer (a) together with the energy levels (b) are shown. The splitting of the INS peak is a consequence of the Zeeman splitting of the lowest doublet $\pm\frac{1}{2}$ and the next doublet $\pm\frac{3}{2}$. At zero magnetic field when these doublets are not split there is only one peak **I** with the energy of 0.79 meV, which represents the
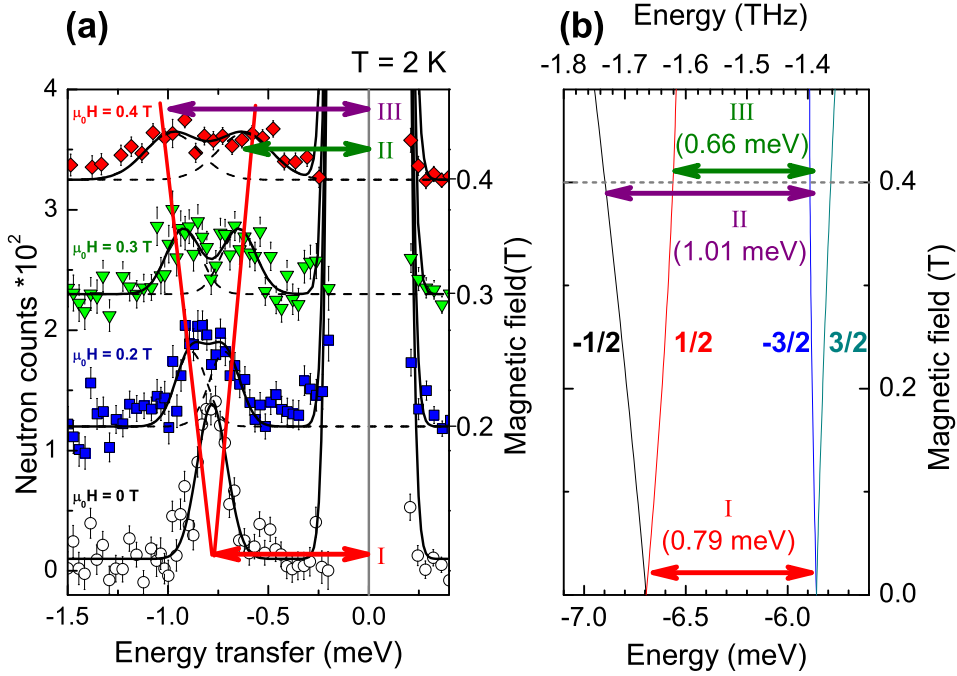
FIGURE 4.14: **a)** Magnetic field development of the inelastic neutron scattering intensity as a function of energy transfer measured on La$_{0.998}$Sr$_{0.002}$CoO$_3$ at $T = 4$ K. Data points are taken from Ref.[111]; **b)** Energy level diagram obtained from the ESR data

transition between the $\pm\frac{1}{2}$ and $\pm\frac{3}{2}$ doublets. At the applied magnetic field of 0.4 T there are two resolved transition peaks **II** and **III** with energies of 1.01 meV and 0.66 meV respectively. The transition **II** is the transition between $-\frac{1}{2}$ state and poorly resolved $\pm\frac{3}{2}$ doublet, the transition **III**, in turn, is the transition between $+\frac{1}{2}$ state and poorly resolved $\pm\frac{3}{2}$ doublet.

4.5.2   La$_{0.998}$Ca$_{0.002}$CoO$_3$, powder sample

The low temperature ESR measured on the powder La$_{0.998}$Ca$_{0.002}$CoO$_3$ showed an intense ESR response at all measured frequencies (Fig.4.15). Due to the powder averaging, the ESR spectra consist of mainly one broad line whose frequency dependence is qualitatively similar to that of the $-\frac{1}{2} \leftrightarrow +\frac{1}{2}$ transition in the case of La$_{0.998}$Sr$_{0.002}$CoO$_3$ sample (open squares). The broad line exhibits gapless frequency dependence, which is characteristic for half-integer spin systems. The effective g-factor value, estimated through linear approximation of the high frequency part of the frequency dependence, is ~ 2.5 (see Fig.4.15). The same approach for the powder La$_{0.998}$Sr$_{0.002}$CoO$_3$ provides a larger g-factor value of ~ 5.2
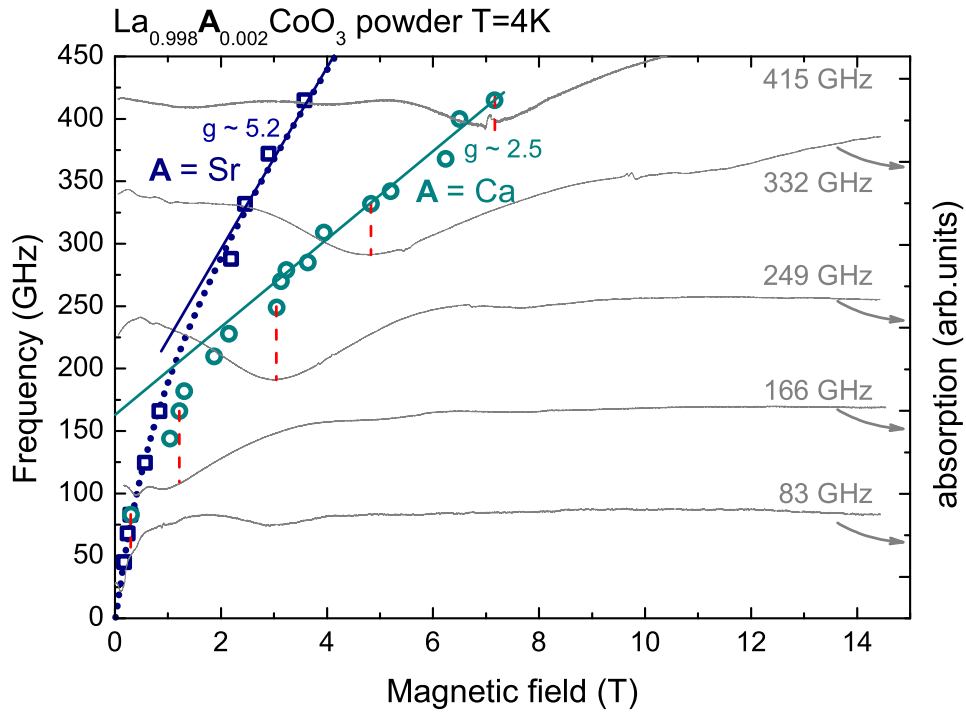
FIGURE 4.15: Frequency dependence of the resonance field of the ESR absorption line measured on powder samples of Sr (squares) and Ca (circles) doped LaCoO$_3$. Straight solid lines represent linear fits of the experimental points at high magnetic fields.

(see Fig.4.15). The qualitative similarities in the ESR of the powder Ca-, and Sr-doped LaCoO$_3$ samples yield the conclusion that magnetic clusters are present at low temperatures in both cases, but the effective g-factor of the magnetic clusters in the case of Ca doped sample is reduced, possibly due to the different local crystal field symmetry because of different ionic radii of Sr and Ca.

4.5.3   La$_{0.998}$Y$_{0.002}$CoO$_3$ powder sample

First of all the ESR response is much weaker in the intensity, more than ~ 20 times (the mass was twice bigger, the intensity 10 times smaller), than that of Ca and Sr doped samples. At all measured frequencies there is a rather narrow gapless resonance absorption C (Fig.4.16, triangles) with $g = 2.04$. This absorption most probably is due to paramagnetic impurities in the samples. One can identify two other resonances A and B (circles and squares), both of which are gapped with energy gap values of $\sim 223\,\mathrm{GHz}$ and $\sim 127\,\mathrm{GHz}$ and g-factors of ~ 4.08 and ~ 3.11 respectively. The gapped nature of the resonance absorptions, seen in the

linear fits, points to the fact that they are results of the transitions between the energy levels of an integer spin, contrary to the case of the Sr doped sample where the spin is half-integer (13/2). Together with the fact that the intensity is much smaller than in the case of Ca- and Sr- doped samples this leads the conclusion that the origin of the response is different from that of La$_{0.998}$Sr$_{0.002}$CoO$_3$ and La$_{0.998}$Ca$_{0.002}$CoO$_3$. The big difference in the ionic radii of Y and La leads to a strong distortion of the O octahedra surrounding the 8 Co ions nearest to Y^{3+}. The strength of the distortion might be enough to stabilize a non-zero spin state of these 8 Co^{3+} ions, IS with the spin $S = 1$ or even HS with $S = 2$, but in contrast to the hole doping they remain not coupled to a giant spin. This creates at low temperatures 1.6% of paramagnetic Co ions. The number is small, that is why it is almost not seen in the magnetization measurements and gives a slight or no increase of NMR spin-lattice relaxation rate. The ESR as a local probe for paramagnetic centers is able to detect it. Therefore the ESR data measured on La$_{0.998}$Y$_{0.002}$CoO$_3$ suggest that the local CF distortion creates magnetic centers due to the change of the spin state of individual Co ions, but does not lead to the formation of magnetic clusters in contrast to that in the Ca and Sr doped LaCoO$_3$ samples. Detailed information about these paramagnetic individual Co ions is still to be obtained from measurements on single crystals which are not yet available.

4.6   Discussion

The magnetization measurements made on the Sr-doped single crystal sample evidence a strong magnetic response at low temperatures with a magnetic moment at saturation of $gS \sim 15\mu_B$/hole. The NMR experiments suggest that the sample has regions with large magnetization which are non-uniformly distributed in the sample volume, i.e., that there are extended magnetic objects formed after Sr doping. ESR investigation gives an additional proof of the existence of magnetic clusters, and provides an important quantitative description: the cluster has a magnetic ground state with a large spin value of 13/2, substantial spin-orbit coupling yielding a g-factor of 2.6 and an energy gap of $\sim 200\,\text{GHz}$ ($\sim 0.8\,\text{meV}$) between the lowest doublet $\pm\frac{1}{2}$ and the first excited triplet $\pm\frac{3}{2}$ due to an axially-symmetric crystal field. The scattering wave vector dependence of the INS intensity (see work by Podlesnyak et al. Ref.[111]) provides the size and the shape of the magnetic cluster which is an octahedrally-shaped Co heptamer (Fig.4.17). The measurements on
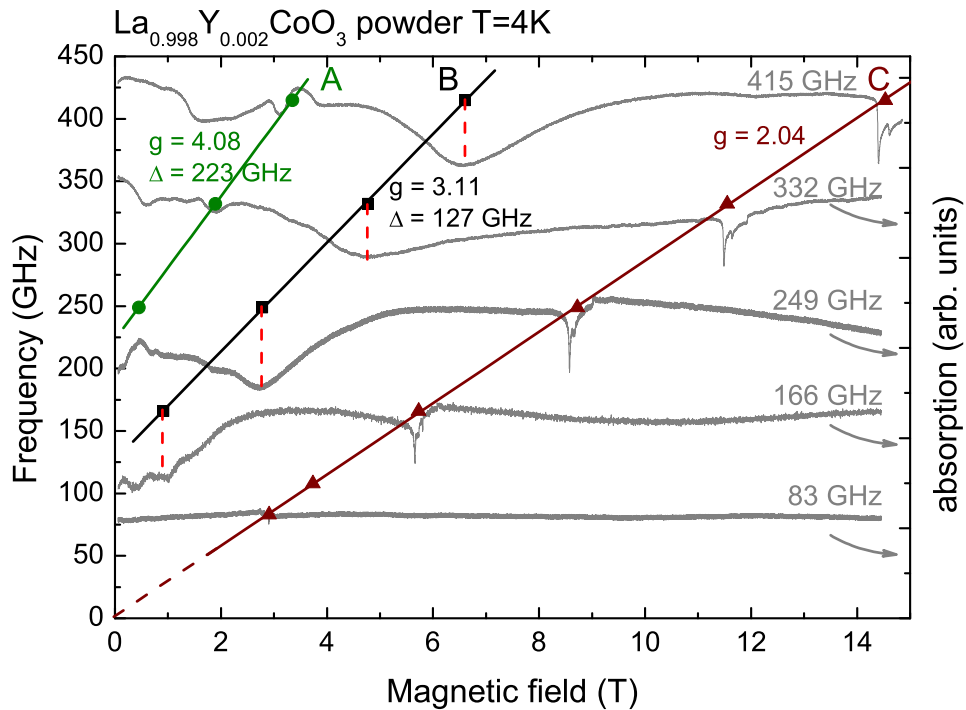
FIGURE 4.16: Frequency dependence of the resonance fields of the ESR absorption lines A, B and C measured on powder sample of Y doped $LaCoO_3$. Straight solid lines represent linear fits of the experimental points.

the Ca-doped $LaCoO_3$ powder sample, where the substitution causes hole doping without any crystal field distortion due to the very similar ionic radii of Ca and La, together with measurements on the Y-doped sample, where there is no hole doping, but only the distortion of the crystal lattice, allow to establish the role of the hole and of the CF distortion in the formation of this extended cluster. The remarkable similarities between Ca- and Sr-doped samples, and absolutely different from Sr-doped sample result of all measurements on the Y-doped sample yield the conclusion that essentially the doped hole is responsible for the cluster formation. Putting all this facts together we propose a model of a spin cluster, or spin polaron, stabilized by the doped hole.

The mechanism of the magnetic cluster (spin polaron) formation is shown on Fig.4.17. The hole introduced by Sr or Ca doping changes the oxidation state of one of the Co from 3+ to 4+. The smaller ionic radii and higher positive charge of the Co^{4+} lead to the attraction of the negatively-charged O ions to the Co^{4+} ion. The displacement of the oxygen weakens the crystal field and reduces its symmetry at the 6 neighboring Co^{3+} ions therefore stabilizing the IS state with $S = 1$, see Fig.4.2. Due to the increased crystal field at the central Co^{4+} ion it

stays in the LS state with $S = 1/2$. From the ESR measurements it is concluded that the spin value amounts to 13/2. To obtain this value all involved Co spins must be coupled ferromagnetically. A reasonable mechanism for the coupling was proposed by Louca and Sarrao [94]. The neighboring LS-Co^{4+} and IS-Co^{3+} ions can share an e_g electron via the double exchange process (Sec.1.12, Fig.4.18). The e_g electron hopes from one Co site to another through the p-orbitals of the oxygen ion and swaps the oxidation and the spin state of the involved Co ions. Due to the Hund's rules the unpared t_{2g} electron is polarized parallel to the e_g electron which yields the ferromagnetic coupling (see Fig.4.18) and stabilization of the high spin $S = 13/2$ of the polaron. Therefore, we propose that the holes introduced in the LS state of LaCoO$_3$ do not stay at a single Co site but are extended over the neighboring Co sites involved in the spin polaron.

4.7   Conclusions

The presented work gives a clear microscopic explanation why hole doping of as low as of 0.2% may dramatically affect the magnetic properties of the entire system. A combined HF-ESR and magnetization studies complemented by NMR and INS measurements enabled to establish that holes introduced in LaCoO$_3$ by substitution of Sr or Ca for La change the oxidation state of one of the Co^{3+} ions from 3+ to 4+ and transform the six nearest-neighbor Co^{3+} ions to the IS state. The double exchange interaction driven by the doped hole couples ferromagnetically the 7 neighboring ions forming octahedrally shaped spin-state polarons. As was proved by the magnetization, NMR and ESR measurements, the additional crystal field distortion introduced due to the different size of the Sr ion seems to play a minor role in the formation of the polaron, possibly changing the details of spin-orbital coupling and the of local crystal field. The local crystal field distortion without hole-doping, like in the Y-doped sample, alone is not enough to form polarons at low-T. ESR data suggests that it can only change the spin state of 1.6 % of Co ions which do not interact.

It is difficult to draw a definite conclusion with regard to the spin polarons stabilizing in the high temperature regime. Plausibly, owing to the activation of magnetic states of Co in the bulk [91, 95, 107], the existence of spin polarons is not anymore energetically favorable, and therefore they continuously dissolve upon raising the temperature in the regular magnetic lattice of IS or HS Co ions.
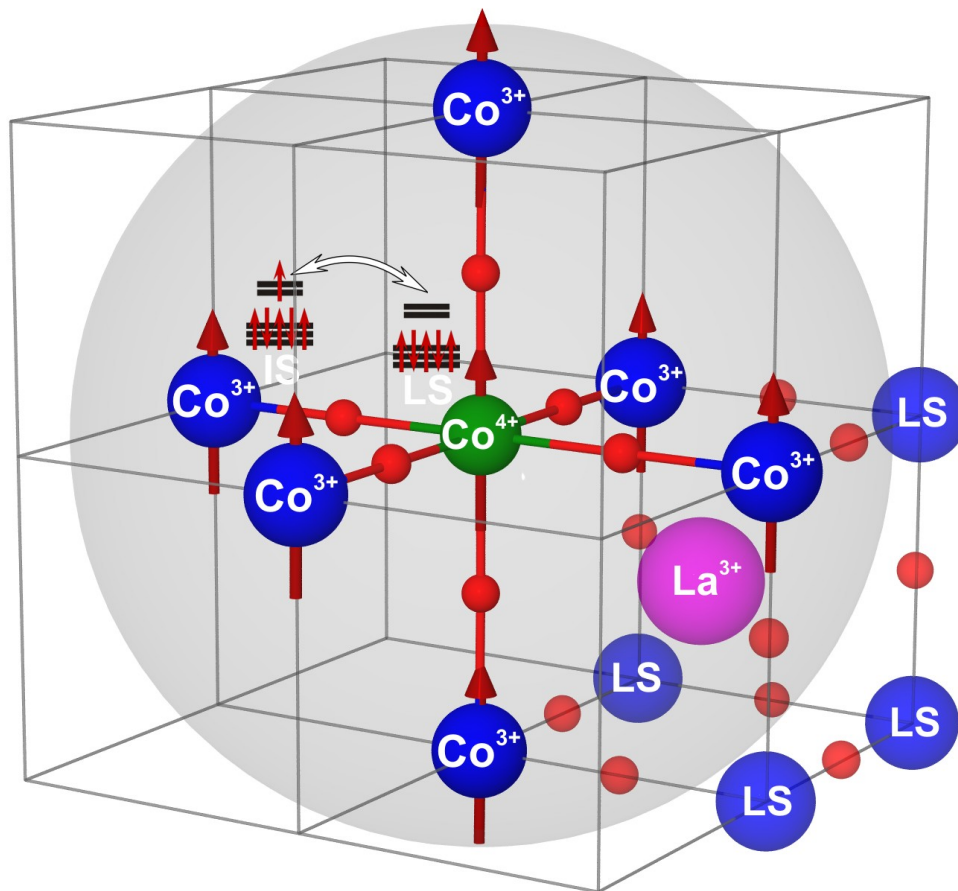
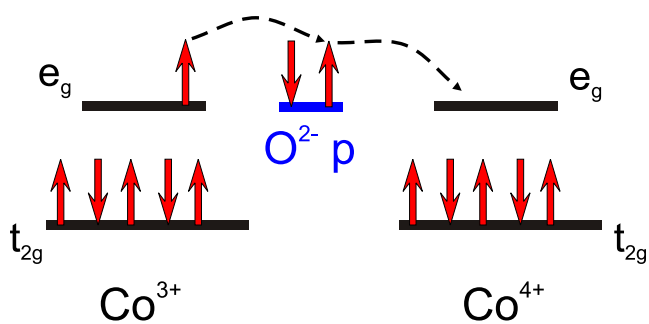FIGURE 4.17: Schematic representation of the polarons in lightly hole-doped LaCoO$_3$.

FIGURE 4.18: Double exchange between Co^{3+} and Co^{4+} ions through oxygen p-orbitals.

A tempting scenario would be that the spin-state polarons in doped LaCoO$_3$ are the building blocks of all low-T magnetic phases present in the phase diagram (see Fig.4.4). At very low doping levels, there are only spin polarons embedded in a nonmagnetic matrix. Increasing the doping level would lead to the agglomeration of the polarons, yielding magnetic clusters of a bigger size, but still localized and behaving as a spin glass. At a certain doping level of $x \sim 0.18$ the metal-insulator transition would take place when the magnetic clusters' size becomes so big that they overlap and the holes can percolate through the whole sample volume. Hence the sample becomes a ferromagnetic metal.

Summary

In this work two representatives of strongly correlated electronic systems have been studied by means of high-field electron spin resonance, complemented by nuclear magnetic resonance, thermodynamic and transport measurements. Our investigation has revealed a significant exchange coupling between Gd- and Fe-layers in the first system, the superconducting $GdO_{1-x}F_xFeAs$ material. Moreover the Gd^{3+} ESR through this coupling has established the coexistence of superconductivity with short-range quasi-static magnetic correlations which suppresses with increasing the doping level and T_c, but still survive at the doping level close to optimal. Such coexistence and possible interplay of usually competing phases suggests a nontrivial nature of the superconductivity, possibly due to a complex electronic structure. In the second material, hole doped perovskite $LaCoO_3$ it has been established that there is a formation of magnetically polarized clusters (polarons) in a nonmagnetic matrix at very low hole doping levels. These magnetic polarons appear to be building blocks for magnetic phases occurring at higher doping levels. To conclude, both examples prove that magnetic and electronic inhomogeneities and coexistence of different phases together with strong electronic interactions play an important role in the physics of these materials.

Bibliography

[1] E. Dagotto, *Nanoscale Phase Separation and Colossal Magnetoresistance* (Springer, 2002).

[2] E. Dagotto, Rev. Mod. Phys. **66**, 763 (1994).

[3] P. A. Lee, N. Nagaosa, and X.-G. Wen, Rev. Mod. Phys. **78**, 17 (2006).

[4] J. S. Miller and M. Drillon, eds., *Magnetism: Molecules to Materials* (Wiley-VCH, 2001).

[5] U. Schollwöck, J. Richter, D. J. Farnell, and R. F. Bishop, *Quantum Magnetism: Lecture Notes In Physics, Volume 645* (Springer-Verlag, 2004).

[6] C. Kittel, *Introduction to Solid State Physics* (WILEY, 2005).

[7] S. Blundell, *Magnetism in Condensed Matter* (Oxford University Press, Oxford, 2001).

[8] J. A. Weil and J. R. Bolton, *Electron Paramagnetic Resonance: Elementary Theory and Practical Applications, 2nd ed.* (Wiley, New York, 2007).

[9] S. A. Altshuler and B. M. Kozyrev, *Electron Paramagnetic Resonance in Compounds of Transition Elements, 2nd ed.* (Wiley, New York, 1974).

[10] A. Abragam and B. Bleaney, *Electron Paramagnetic Resonance of Transition Ions* (1970).

[11] J. Charles P. Poole, *Electron Spin Resonance: A Comprehensive Treatise on Experimental Techniques, 2nd ed.* (Dover, New York, 1996).

[12] L. D. Landau and L. M. Lifshitz, *Quantum Mechanics: Non-Relativistic Theory, Third Edition: Volume 3* (Butterworth-Heinemann, London, 1981).

[13] L. Pauling and E. B. W. Jr., *Introduction to Quantum Mechanics with Applications to Chemistry* (McGraw-Hill, New York and London, 1935).

[14] R. Shankar, *Principles of Quantum Mechanics, 2nd ed.* (Springer, 1994).

[15] J. Schwinger, *Particles, Sources and Fields, Vol. III* (Perseus Books, Reading, MA, U.S.A., 1998).

[16] A. Das and S. Perez, Phys. Lett. B **581**, 182 (2004).

[17] T. Kinoshita and M. Nio, Phys. Rev. D **73**, 013003 (2006).

[18] D. R. Hartree, Mathematical Proceedings of the Cambridge Philosophical Society **24**, 89 (1928).

[19] V. Fock, Zeitschrift für Physik A Hadrons and Nuclei **61**, 126 (1930).

[20] J. C. Slater, Phys. Rev. **34**, 1293 (1929).

[21] F. Hund, Zeitschrift für Physik A Hadrons and Nuclei **33**, 345 (1925).

[22] F. Hund, Zeitschrift für Physik A Hadrons and Nuclei **33**, 855 (1925).

[23] F. Hund, *Linienspektren und periodisches System der Elemente* (Springer, Berlin, 1927).

[24] W. Pauli, Zeitschrift für Physik A Hadrons and Nuclei **31**, 765 (1925).

[25] L. H. Thomas, Nature (London) **117**, 514 (1926).

[26] H. N. Russell and F. A. Saunders, Astrophysical Journal **61**, 38 (1925).

[27] P. Zeeman, Astrophysical Journal **5**, 332 (1897).

[28] D. J. Newman and W. Urban, Advances in Physics **24**, 6 (1975).

[29] H. A. Kramers, Proc. Acad. Sci. Amsterdam **33**, 959 (1930).

[30] K. W. H. Stevens, Proceedings of the Physical Society. Section A **65**, 209 (1952).

[31] B. Bleaney and K. W. H. Stevens, Reports on Progress in Physics **16**, 108 (1953).

[32] W. Heisenberg, Z. Phys. **38**, 411 (1926).

[33] W. Heisenberg, Z. Phys. **49**, 619 (1928).

[34] P. W. Anderson, Phys. Rev. **79**, 350 (1950).

[35] J. B. Goodenough, Phys. Rev. **100**, 564 (1955).

[36] J. B. Goodenough, Journal of Physics and Chemistry of Solids **6**, 287 (1958).

[37] J. Kanamori, Journal of Physics and Chemistry of Solids **10**, 87 (1959).

[38] C. Zener, Phys. Rev. **82**, 403 (1951).

[39] W. Gerlach and O. Stern, Zeitschrift für Physik A Hadrons and Nuclei **9**, 353 (1922).

[40] B. Friedrich and D. Herschbach, Physics Today **56**, 53 (2003).

[41] A. Einstein and P. Ehrenfest, Zs. f. Phys. **11**, 31 (1922).

[42] G. E. Uhlenbeck and S. Goudsmit, Die Naturwissenschaften **13**, 953 (1925).

[43] G. Breit and I. I. Rabi, Phys. Rev. **38**, 2082 (1931).

[44] I. I. Rabi, J. R. Zacharias, S. Millman, and P. Kusch, Phys. Rev. **53**, 318 (1938).

[45] E. Zavoisky, J. Phys. U.S.S.R. **9**, 211, 245 (1945).

[46] R. A. Beth, Phys. Rev. **48**, 471 (1935).

[47] R. A. Beth, Phys. Rev. **50**, 115 (1936).

[48] W. Heisenberg, Zeitschrift für Physik A Hadrons and Nuclei **43**, 172 (1927).

[49] *Bruker EMX Users Manual* (1998).

[50] C. Golze, Ph.D. thesis, Dresden university of technology (2007).

[51] U. Schaufuss, Ph.D. thesis, Dresden university of technology (2009).

[52] C. Golze, A. Alfonsov, R. Klingeler, B. Büchner, V. Kataev, C. Mennerich, H.-H. Klauss, M. Goiran, J.-M. Broto, H. Rakoto, et al., Phys. Rev. B **73**, 224403 (2006).

[53] Y. Kamihara, T. Watanabe, M. Hirano, and H. Hosono, J. Am. Chem. Soc. **130**, 32963297 (2008).

[54] X. H. Chen, T. Wu, G. Wu, R. H. Liu, H. Chen, and D. F. Fang, Nature (London) **453**, 761 (2008).

[55] A. J. Drew, C. Niedermayer, P. J. Baker, F. L. Pratt, S. J. Blundell, T. Lancaster, R. H. Liu, G. Wu, X. H. Chen, I. Watanabe, et al., Nat. Mater. **8**, 310 (2009).

[56] C. Hess, A. Kondrat, A. Narduzzo, J. E. Hamann-Borrero, R. Klingeler, J. Werner, G. Behr, and B. Büchner, EPL (Europhysics Letters) **87**, 17005 (2009).

[57] H. Luetkens, H.-H. Klauss, M. Kraken, F. J. Litterst, T. Dellmann, R. Klingeler, C. Hess, R. Khasanov, A. Amato, C. Baines, et al., Nat. Mater. **8**, 305 (2009).

[58] J. Zhao, Q. Huang, C. de la Cruz, S. Li, J. W. Lynn, Y. Chen, M. A. Green, G. F. Chen, G. Li, Z. Li, et al., Nat. Mater. **7**, 953 (2008).

[59] S. Sanna, R. De Renzi, T. Shiroka, G. Lamura, G. Prando, P. Carretta, M. Putti, A. Martinelli, M. R. Cimberle, M. Tropeano, et al., Phys. Rev. B **82**, 060508(R) (2010).

[60] M.-H. Julien, H. Mayaffre, M. Horvatic, C. Berthier, X. D. Zhang, W. Wu, G. F. Chen, N. L. Wang, and J. L. Luo, EPL (Europhysics Letters) **87**, 37001 (5pp) (2009).

[61] Y. Laplace, J. Bobroff, F. Rullier-Albenque, D. Colson, and A. Forget, Phys. Rev. B **80**, 140501 (2009).

[62] R. R. Urbano, E. L. Green, W. G. Moulton, A. P. Reyes, P. L. Kuhns, E. M. Bittar, C. Adriano, T. M. Garitezi, L. Bufaial, and P. G. Pagliuso, Phys. Rev. Lett. **105**, 107001 (2010).

[63] T. Nomura, S. W. Kim, Y. Kamihara, M. Hirano, P. V. Sushko, K. Kato, M. Takata, A. L. Shluger, and H. Hosono, Supercond. Sci. Technol. **21**, 125028 (2008).

[64] H. Maeter, H. Luetkens, Y. G. Pashkevich, A. Kwadrin, R. Khasanov, A. Amato, A. A. Gusev, K. V. Lamonova, D. A. Chervinskii, R. Klingeler, et al., Phys. Rev. B **80**, 094524 (2009).

[65] C. Bernhard, A. J. Drew, L. Schulz, V. K. Malik, M. Roessle, C. Niedermayer, T. Wolf, G. D. Varma, G. Mu, H. H. Wen, et al., New Journal of Physics **11**, 055050 (2009).

[66] Y. Nakai, K. Ishida, Y. Kamihara, M. Hirano, and H. Hosono, J. Phys. Soc. Jpn. **77**, 073701 (2008).

[67] G. Prando, P. Carretta, A. Rigamonti, S. Sanna, A. Palenzona, M. Putti, and M. Tropeano, Phys. Rev. B **81**, 100508 (2010).

[68] A. Kondrat, J. E. Hamann-Borrero, N. Leps, M. Kosmala, O. Schumann, A. Köhler, J. Werner, G. Behr, M. Braden, R. Klingeler, et al., Eur. Phys. J. B **70**, 461 (2009).

[69] N. D. Zhigadlo, S. Katrych, Z. Bukowski, S. Weyeneth, R. Puzniak, and J. Karpinski, Journal of Physics: Condensed Matter **20**, 342202 (2008).

[70] H.-H. Klauss, H. Luetkens, R. Klingeler, C. Hess, F. J. Litterst, M. Kraken, M. M. Korshunov, I. Eremin, S.-L. Drechsler, R. Khasanov, et al., Phys. Rev. Lett. **101**, 077005 (2008).

[71] S. E. Barnes, Adv. Phys. **30**, 801 (1981).

[72] E. Dengler, J. Deisenhofer, H.-A. Krug von Nidda, S. Khim, J. S. Kim, K. H. Kim, F. Casper, C. Felser, and A. Loidl, Phys. Rev. B **81**, 024406 (2010).

[73] J. Korringa, Physica **16**, 601 (1950).

[74] R. Klingeler, N. Leps, I. Hellmann, A. Popa, U. Stockert, C. Hess, V. Kataev, H. Grafe, F. Hammerath, G. Lang, et al., Phys. Rev. B **81**, 024506 (2010).

[75] N. D. Zhigadlo, S. Katrych, S. Weyeneth, R. Puzniak, P. J. W. Moll, Z. Bukowski, J. Karpinski, H. Keller, and B. Batlogg, Phys. Rev. B **82**, 064517 (2010).

[76] M. Rotter, M. Pangerl, M. Tegel, and D. Johrendt, Angew. Chem. **47**, 7949 (2008).

[77] A. Koitzsch, D. S. Inosov, D. V. Evtushinsky, V. B. Zabolotnyy, A. A. Kordyuk, A. Kondrat, C. Hess, M. Knupfer, B. Büchner, G. L. Sun, et al., Phys. Rev. Lett. **102**, 167001 (2009).

[78] A. Kondrat, G. Behr, B. Büchner, and C. Hess, Phys. Rev. B **83**, 092507 (2011).

[79] G. F. Goya, R. C. Mercader, L. B. Stere, R. D. Sánchez, M. T. Causa, and M. Tovar, J. Phys.: Condens. Matter **8**, 4529 (1996).

[80] C. de la Cruz, Q. Huang, J. W. Lynn, J. Li, W. Ratcliff II, J. L. Zarestky, H. A. Mook, G. F. Chen, J. L. Luo, N. L. Wang, et al., Nature **453**, 899 (2008).

[81] A. Fainstein, A. Butera, and M. Tovar, Phys. Rev. B **50**, 16708 (1994).

[82] S. B. Oseroff, D. Rao, F. Wright, D. C. Vier, S. Schultz, J. D. Thompson, Z. Fisk, S.-W. Cheong, M. F. Hundley, and M. Tovar, Phys. Rev. B **41**, 1934 (1990).

[83] M. A. McGuire, A. D. Christianson, A. S. Sefat, B. C. Sales, M. D. Lumsden, R. Jin, E. A. Payzant, D. Mandrus, Y. Luan, V. Keppens, et al., Phys. Rev. B **78**, 094517 (2008).

[84] Y. Kohama, Y. Kamihara, M. Hirano, H. Kawaji, T. Atake, and H. Hosono, Phys. Rev. B **78**, 020512 (2008).

[85] S. Shamoto, M. Ishikado, S. Wakimoto, K. Kodama, R. Kajimoto, M. Arai, T. Fukuda, H. Nakamura, M. Machida, and H. Eisaki, Physica C: Superconductivity **470**, S284 (2009).

[86] S. Wakimoto, K. Kodama, M. Ishikado, M. Matsuda, R. Kajimoto, M. Arai, K. Kakurai, F. Esaka, A. Iyo, H. Kito, et al., Journal of the Physical Society of Japan **79**, 074715 (2010).

[87] J. P. Carlo, Y. J. Uemura, T. Goko, G. J. MacDougall, J. A. Rodriguez, W. Yu, G. M. Luke, P. Dai, N. Shannon, S. Miyasaka, et al., Phys. Rev. Lett. **102**, 087001 (2009).

[88] A. Alfonsov, F. Murányi, V. Kataev, G. Lang, N. Leps, L. Wang, R. Klingeler, A. Kondrat, C. Hess, S. Wurmehl, et al., Phys. Rev. B **83**, 094526 (2011).

[89] J. H. Davies, *The Physics of Low-dimensional Semiconductors: An Introduction* (Cambridge University Press, 1997).

[90] D. Gatteschi, R. Sessoli, and J. Villain, Oxford University Press, Oxford (2006).

[91] M. Senaris-Rodriguez and J. Goodenough, J. Solid State Chem. **118**, 323 (1995).

[92] V. G. Bhide, D. S. Rajoria, C. N. R. Rao, G. R. Rao, and V. G. Jadhao, Phys. Rev. B **12**, 2832 (1975).

[93] J. Wu and C. Leighton, Phys. Rev. B **67**, 174408 (2003).

[94] D. Louca and J. L. Sarrao, Phys. Rev. Lett. **91**, 155501 (2003).

[95] D. Phelan, D. Louca, K. Kamazawa, S.-H. Lee, S. N. Ancona, S. Rosenkranz, Y. Motome, M. F. Hundley, J. F. Mitchell, and Y. Moritomo, Phys. Rev. Lett. **97**, 235501 (2006).

[96] M. Imada, A. Fujimori, and Y. Tokura, Rev. Mod. Phys. **70**, 1039 (1998).

[97] S. Yamaguchi, Y. Okimoto, and Y. Tokura, Phys. Rev. B **55**, R8666 (1997).

[98] S. Yamaguchi, Y. Okimoto, H. Taniguchi, and Y. Tokura, Phys. Rev. B **53**, R2926 (1996).

[99] S. Stoll and A. Schweiger, J. Magn. Reson. **178(1)**, 42 (2006).

[100] *easyspin.org* (2006).

[101] P. M. Raccah and J. B. Goodenough, Phys. Rev. **155**, 932 (1967).

[102] K. Asai, O. Yokokura, N. Nishimori, H. Chou, J. M. Tranquada, G. Shirane, S. Higuchi, Y. Okajima, and K. Kohn, Phys. Rev. B **50**, 3025 (1994).

[103] M. Itoh, I. Natori, S. Kubota, and K. Motoya, Journal of the Physical Society of Japan **63**, 1486 (1994).

[104] M. A. Senaris-Rodriguez and J. B. Goodenough, Journal of Solid State Chemistry **116**, 224 (1995).

[105] S. Noguchi, S. Kawamata, K. Okuda, H. Nojiri, and M. Motokawa, Phys. Rev. B **66**, 094404 (2002).

[106] M. W. Haverkort, Z. Hu, J. C. Cezar, T. Burnus, H. Hartmann, M. Reuther, C. Zobel, T. Lorenz, A. Tanaka, N. B. Brookes, et al., Phys. Rev. Lett. **97**, 176405 (2006).

[107] A. Podlesnyak, S. Streule, J. Mesot, M. Medarde, E. Pomjakushina, K. Conder, A. Tanaka, M. W. Haverkort, and D. I. Khomskii, Phys. Rev. Lett. **97**, 247208 (2006).

[108] M. Itoh and I. Natori, J. Phys. Soc. Jpn. **64**, 970 (1995).

[109] Y. Kobayashi, N. Fujiwara, S. Murata, K. Asai, and K. Yasuoka, Phys. Rev. B **62**, 410 (2000).

[110] M. J. R. Hoch, P. L. Kuhns, W. G. Moulton, A. P. Reyes, J. Wu, and C. Leighton, Phys. Rev. B **69**, 014425 (2004).

[111] A. Podlesnyak, M. Russina, Furrer, A. Alfonsov, Vavilova, V. Kataev, B. Büchner, T. Strässle, E. Pomjakushina, K. Conder, et al., Phys. Rev. Lett. **101**, 247603 (2008).

Acknowledgment

In the first place I would like to show my gratitude to Prof. Dr. Bernd Büchner for giving me the opportunity to perform my research work in the well equipped laboratory in the Leibniz Institute for Solid State and Materials Research (IFW) and for constant interest in the progress of my work.

I owe my deepest gratitude to my advisor Dr. Vladislav Kataev, a group leader of the ESR laboratory. This thesis would not have been possible without his fruitful discussions, brilliant advices, encouragement and willingness to help no matter how busy he is.

Special thanks to Dr. Ferenc Murányi and Dr. Guillaume Lang for sharing their great experience in the field of magnetic resonance and solid state physics which helped me to avoid many problems during my work.

I would like to thank Prof. Dr. Rüdiger Klingeler for the fruitful discussions concerning the thermodynamic properties of materials and for being referee of my PhD thesis.

I am grateful to Dr. Evgenia Vavilova for help in understanding the NMR data that she measured. I am very thankful to Dr. Christian Hess for the measurements and discussions concerning transport properties of materials. I would like to acknowledge Dr. Sabine Wurmehl for the Fe-pnictide sample preparation. I am thankful to Dr. Silke Hampel for the help in X-ray diffraction measurements.

I would like to acknowledge Dr. Andrei Podlesniak, who provided our group with the hole doped $LaCoO_3$ sample and performed INS measurements.

I am very thankful to Falk Herold who was building not only precisely but also very fast important parts and details for the devices in the laboratory.

Publication List

1. A. Podlesnyak, M. Russina, A. Furrer, **A. Alfonsov**, E. Vavilova, V. Kataev, B.Büchner, T. Strässle, E. Pomjakushina, K. Conder and D. I. Khomskii Spin-State Polarons in Lightly-Hole-Doped $LaCoO_3$. *Phys Rev Lett* **101**, 247603, 2008.

2. A. Sachse, G. Noël, S. Dechert, S. Demeshko, A. Honecker, **A. Alfonsov**, V. Kataev and F. Meyer. Bulky Pyrazolate-Based Compartmental Ligand Scaffolds: Encapsulation of an Edge-Sharing Cu_6O_2 Bitetrahedral Core. *Eur J Inorg Chem* **34**, 5390 - 5396, 2008.

3. V. Kataev, U. Schaufuss, F. Murányi, **A. Alfonsov**, M. Doerr, M. Rotter and B. Büchner. Magnetic anisotropy of the spin-antiferromagnet $GdNi_2B_2C$ probed by high-frequency ESR. *J Phys: Conf Ser* **150**, 042086, 2009.

4. **A. Alfonsov**, E. Vavilova, V. Kataev, B. Büchner, A. Podlesnyak, M. Russina, A. Furrer, T. Strässle, E. Pomjakushina, K. Conder and D. I. Khomskii. Origin of a spin-state polaron in lightly hole doped $LaCoO_3$. *J Phys: Conf Ser* **150**, 042003, 2009.

5. Y. Krupskaya, A. Parameswaran, **A. Alfonsov**, R. Klingeler, V. Kataev, N. Beyer, J. Lach, M. Gressenbuch, B. Kersting, B. Büchner. High-Field ESR and Magnetization Study of a Novel Macrocyclic Chelate Trinuclear Ni(II) Complex. *J Low Temp Phys* **159**, 84-87, 2010.

6. Y. Krupskaya, **A. Alfonsov**, A. Parameswaran, V. Kataev, R. Klingeler, G. Steinfeld, N. Beyer, M. Gressenbuch, B. Kersting, B Büchner. Interplay of Magnetic Exchange Interactions and Ni-S-Ni Bond Angles in Polynuclear Nickel(II) Complexes. *ChemPhysChem* **11**, 1961-1970, 2010.

7. **A. Alfonsov**, F. Murányi, V. Kataev, N. Leps, R. Klingeler, A. Kondrat, C. Hess, J. Werner, G. Behr and B. Büchner. High field ESR spectroscopy on $GdO_{1-x}F_xFeAs$. *J Low Temp Phys* **159**, 172-175, 2010.

8. V. Kataev, **A. Alfonsov**, E. Vavilova, A. Podlesnyak, D. I. Khomskii, and B. Büchner. Formation of magnetic polarons in lightly Ca doped $LaCoO_3$. *J Phys: Conf Ser* **200**, 012080, 2010.

9. **A. Alfonsov**, F. Murányi, V. Kataev, G. Lang, N. Leps, L. Wang, R. Klingeler, A. Kondrat, C. Hess, S. Wurmehl, A. Köhler, G. Behr, S. Hampel, M. Deutschmann, S. Katrych, N. D. Zhigadlo, Z. Bukowski, J. Karpinski and B. Büchner. High-field electron spin resonance spectroscopy study of GdFeAsO$_{1-x}$F$_x$ superconductors. *Phys Rev B* **83**, 094526, 2011.

Diese Arbeit wurde unter Betreuung von Prof. Dr. B. Büchner am Institut für Festkörperforschung (IFF) des Instituts für Festkörper- und Werkstoffforschung Dresden e.V. (IFW Dresden) angefertigt.

Versicherung

Hiermit versichere ich, dass ich die vorliegende Arbeit ohne zulässige Hilfe Dritter und ohne Benutzung anderer als der angegebenen Hilfsmittel angefertigt habe; die aus fremden Quellen direkt oder indirekt übernommenen Gedanken sind als solche kenntlich gemacht. Die Arbeit wurde bisher weder im Inland noch im Ausland in gleicher oder ähnlicher Form einer anderen Prüfungsbehörde vorgelegt.

Ich erkenne hiermit die Promotionsordnung der TU Dresden an.

Curriculum Vitae

Name	Alexey Alfonsov
Date of birth	28. 09. 1984
Place of birth	Kazan, Russia
Nationality	Russian
Contact	a.alfonsov@ifw-dresden.de
2001 − 2007	Studied Physics in Kazan State University, Kazan, Russia
February 2005	Visited the Leibniz Institute for Solid State and Materials Research Dresden to perform a part of a bachelor work
June 2005	Bachelor in Physics. Topic: "EPR spectroscopy of the tetranuclear Ni(II) complex with a central μ_4 azide in strong magnetic fields ".
March 2006 **February − April 2007**	Visited the Leibniz Institute for Solid State and Materials Research Dresden to perform a part of a master work
June 2007	Master in Physics. Topic: "Investigation of the Fe magnetic states in low-dimensional polymer system PAC by means of electron spin resonance and static magnetometery".
Since **September 2007**	PhD student at the Leibniz Institute for Solid State and Materials Research Dresden